**A Comparison of Afghanistan, Yuma, AZ, and Manufactured Sands Melted on
EB-PVD Thermal Barrier Coatings**

THESIS

Nathaniel P. Opie, Captain, USAF

AFIT-ENY-T-14-S-18

**DEPARTMENT OF THE AIR FORCE
AIR UNIVERSITY**

AIR FORCE INSTITUTE OF TECHNOLOGY

Wright-Patterson Air Force Base, Ohio

AFIT-ENY-T-14-S-18

A COMPARISON OF AFGHANISTAN, YUMA, AZ, AND MANUFACTURED SANDS MELTED ON EB-PVD THERMAL BARRIER COATINGS

THESIS

Presented to the Faculty

Department of Aeronautics and Astronautics

Graduate School of Engineering and Management

Air Force Institute of Technology

Air University

Air Education and Training Command

In Partial Fulfillment of the Requirements for the

Degree of Master of Science in Materials Science

Nathaniel P. Opie, B.S.M.E

Captain, USAF

Septemeber 2014

AFIT-ENY-T-14-S-18

**A COMPARISON OF AFGHANISTAN, YUMA, AZ, AND MANUFACTURED
SANDS MELTED ON EB-PVD THERMAL BARRIER COATINGS**

Nathaniel P. Opie, BS

Captain, USAF

Approved:

_____/Signed/_____	19 June 2104
Timothy Radsick, Lt Col, USAF, PhD (Chairman)	Date
_____/Signed/_____	26 August 2014
James Rutledge, Maj, USAF, PhD (Member)	Date
_____/Signed/_____	26 August 2014
Andrew Phelps, PhD (Member)	Date

Abstract

Military operations such as Desert Shield/Storm and Enduring Freedom have tested the ability of military aircraft performance in dry, desert-like environments. Sand and dust from these areas is ingested into gas turbine engines causing damage to many engine components. In particular, after operation in these sandy/dusty environments blades and nozzles in the turbine section are often found to be coated with a molten glass-substance, created when ingested material is heated to melting temperatures. This molten glass attacks environmental barrier coatings and thermal barrier coatings on the surface of these parts.

In order to improve thermal barrier coating (TBC) research, in particular the response of TBC to sand attack, the present study investigated the behavior of natural sand behavior on thermal barrier coatings when heated to high temperatures such as those present in the turbine engine. Test results from natural sand were compared to those of manufactured sand, the material commonly used in current engine qualification testing. The manufactured sand should behave like natural sand melted on a thermal barrier coating to substantiate past, current, and future testing.

Specifically, in the present study natural sands from Yuma Arizona and Afghanistan were heated to melting temperatures side-by-side with manufactured sands that were specifically created for engine testing. Also, EB-PVD TBC buttons provided by two different companies were used – these two companies currently provide turbine

component coating services to the aerospace industry. A comparison of the sands

melting behavior and cooling interaction with the two different EB-PVD TBCs was made

in this study.

In this comparison it was found that of the three manufactured sands tested,

AFRL 02, behaved most like the natural sands from Afghanistan in sintering and melting

behavior, mass loss behavior, and surface energy reduction across a TBC surface. A

second manufactured sand, PTI A1, behaved most like the Yuma sand in sintering and

melting behavior, wetting and TBC top coat infiltration. The manufactured sand QGCS

was found to behave differently from the other natural or manufactured sand samples in

melting, sintering, and wetting. Both manufactured sands and natural sands were found

to produce similar results of TBC delamination cracking commonly found on TBC-

coated blades and nozzles in operational turbine engines.

Acknowledgements

I know she would not do it on her own. She has been the best wife/mother/friend I could ever have through this journey at AFIT.

Table of Contents

Page

List of Figures

List of Tables

Page

Acronyms

A1 – PTI A1 Ultra-Fine sand sample

A2 – PTI A2 Fine sand sample

Al – Aluminum

Afg Bl – Afghan Blade sand sample

AFM – Afghanistan mixed sand

AFRL – Air Force Research Lab

AOR – Area of Responsibility

ASTER – Advanced Spaceborne Thermal Emission and Reflection Radiometer

Bal Bl – Balad Blade sand sample

BC – Bond Coat

Button A – TBC Button made by Manufacturer A

Button B – TBC Button made by Manufacturer B

Ca – Calcium

CMAS – Calcium, Magnesium, Aluminum, Silicate

CTIO – Coating Technology Integration Office

Cr – Chromium

CTE – Coefficient of Thermal Expansion

DoD – Department of Defense

EBC – Environmental Barrier Coating

EB-PVD – Electron Beam Physical Vapor Deposition

EDS - Energy Dispersive X–ray Spectroscopic analysis

FOD - Foreign Object Debris

GB – Grain Boundary

Helm – Helmand Basin sand

HPT – High Pressure Turbine

K – Potassium

KBr – Potassium Bromide

Mfg-sand – Manufactured sand (Section 1.4 for definition)

Mg – Magnesium

Na – Sodium

Nat-sand – Natural sand (Section 1.4 for definition)

Ni – Nickel

O – Oxygen

OEM – Original Equipment Manufacture

Pd – Palladium

Pt – Platinum

PTI – Powder Technology Inc.

PVD - Physical Vapor Deposition

RAM – ARAMCO sand sample

SEM – Scanning Electron Microscope

Si – Silicon

Sim-CMAS – Simulated CMAS (Section 1.4 for definition)

SLR – Single Lens Reflex

SPM – Suspended Particle Matter

S – Sulfur

TBC – Thermal Barrier Coating

TC – Thermocouple

T_M – Melting temperature

TSP – Total Suspended Particulate Matter

UAE – United Arab Emirates

USCENTCOM – U.S. Central Command

VA – Volcanic Ash

YSZ – Yttria-Stabilized Zirconia

Yuma – Yuma Proving Ground sand

Zr – Zirconium

A Comparison of Afghanistan, Yuma, AZ, and Manufactured Sands Melted on

EB-PVD Thermal Barrier Coatings

I. Introduction

1.1 Background

Military operations such as Desert Shield/Storm and Enduring Freedom have tested the ability of military aircraft performance in dry desert-like environments. Sand and dust from these desert-like areas are ingested into the aircraft's gas turbine engines, causing damage to many of its components. In particular, the components of the engine's turbine section are coated with a molten glass when the sand is heated to melting temperatures at this section. This molten glass attacks environmental barrier coatings (EBC) and thermal barrier coatings (TBC) on the hot surfaces of these components.

Thermal barrier coatings are thermal insulating layers of ceramic bonded to the surface of turbine section blades, nozzles, and inner wall lining. In addition to TBCs, streams of cool inlet air flow through cooling passages in the interior of some components, carrying away heat absorbed from combustion. Lastly, this cool air exits the surface of the part exposed to the heat, and flowing across the parts surface to create a turbulent layer of film cooled air, thereby reduced the thermal heating of the parts within the turbine section. The combination of the cooling and thermal insulating techniques allow the gas turbine engine to reach higher performance and efficiency; without these methods, maximum turbine inlet temperatures would need to be reduced. If one of these thermal control techniques is compromised, excessive wear and premature failure of

engine parts is likely, as component temperatures exceed the thermal limits of their structural materials.

Sand and dust from desert-like environments have been identified as an operational hazard, compromising the integrity of both TBCs and cooling passages. Fine dust can enter the internal cooling passages eventually blocking the cooling air stream. Sand and dust that enter the compressor section eventually transit through the combustor and into the turbine section. Gas temperatures of approximately 1900 ºC in the turbine section soften the sand by liquid phase sintering. As the sand softens it can potentially adhere to the TBC on blades, nozzles, or lining walls. Surface temperatures of these parts in the turbine section, though lower than that of the combustion gases, are approximately 1150 ºC – 1350 ºC. Once softened, sand particles adhere to these parts, and further melting takes place until particles liquefy into a molten glass. The molten glass liquid has the ability to infiltrate the microstructure of the TBC. As the parts cool during the shutdown of the engine, the molten material that has infiltrated into the TBC cools to form a glass, altering the coefficient of thermal expansion of the bulk material and creating a thermal expansion mismatch between the affected area and the unaffected area. This thermal expansion mismatch, combined with a change in temperature of 1200 ºC, initiates cracking and drives crack propagation, leading to delamination and failure of the TBC layer. Failure of the TBC leads to premature failure of engine components, and possibly catastrophic failure of the engine.

The cooled glass material on the TBC has been described as a thin smooth, pink-brown deposit or a rough light brown deposit [1]. These glass-like deposits have been

chemically analyzed and have been reported to contain mostly calcium oxide, magnesium oxide, aluminum oxide, and silicon oxide along with other trace elements [1] [2]. Because of its composition, this material has been termed Calcium Magnesium Aluminum Silicate—or, commonly, CMAS. A chemically analogous substance, comprising the same elemental composition as CMAS, has been the material used to study CMAS and TBC [3]. The type of CMAS commonly used in experimentation is a mixture of elemental oxide powders. The compositional make-up of the experimental CMAS is similar to the composition reported from harvested CMAS samples collected from engine parts. The aim of the simulated CMAS testing has been to create a better understanding of sand attack on TBC coatings.

Other studies of sand ingestion attack on the gas turbine engine have been conducted by the US Army, US Navy, and US Air Force. The guidance for sand particle ingestion testing is designed to ensure engines bought by the agencies can maintain a satisfactory level of performance when operated in sand environments [4]. This guidance is called out in the Department of Defense Joint Service Specification Guide Engines, Aircraft, Turbine (JSSG), [4], and uses a manufactured sand having specific composition and particle size requirements set by the respective military service. The US Army uses a sand called PTI A1. The US Navy use a sand called QGCS (which stands for quartz, gypsum, calcite, and salt). The composition and size distribution of these sands will be found in later sections of the present document. During testing the sand is introduced into the engines under the guidelines of specific test procedures [4]. The level of

resulting engine damage is assessed to determine if the engine meets the set of service standards.

The engines currently in operational service in Southwest Asia have passed the above requirements/tolerances for sand ingestion; these same engines, however are being placed into maintenance earlier than expected due to accelerated degradation due to sand ingestion. Such a discrepancy between qualification testing and operational reality indicates that further research is needed in this area. Therefore the present study hopes to add to the field of knowledge of sand interaction with TBCs, through methodical study of the effects of natural sand and manufactured sand on TBC.

1.2 Problem Statement

The engines used for military aircraft undergo sand ingestion testing before being allowed into service, however, engines are commonly taken out of service earlier than expected due to sand ingestion damage. There are several reasons why the qualification testing and operational engine wear are resulting in different outcomes. One cause could be that testing procedures do not accurately represent sand ingestion as it happens in real world operations. Another possible cause is that the type of sand used during testing may not accurately represent the behavior of actual sand ingested in real world operations. Likely, testing improvements in both areas are warranted

Natural sands are a very complex material. Natural sands can differ greatly from region to region with respect to the composition of minerals, the particle sizes and size distributions, and the softening and melting points during heating. The manufactured

sand used in qualification testing can likewise vary in composition by a wide margin from natural sand seen in operational use. Thus, results of testing using manufactured sand can be expected to differ from the results of operational service. Therefore analysis of melting behavior between natural sands and the manufactured sands used in engine testing is in order to characterize similarities and differences.

Testing conducted for CMAS and TBC interaction uses only a simulated CMAS composition – i.e. matching the composition of the glass residue remaining on sand-attacked turbine blades. Since the simulated CMAS is not consistent with natural sand composition, the results of testing with CMAS do not provide information about the process of natural sand melting and interacting with a TBC. Therefore testing with natural sands and more representative manufactured sands is necessary to build an understanding of the melting and infiltration behavior of CMAS-forming sands.

The United States military relies on robust, sustainable gas turbine engines in a large number of their military vehicles. Sand ingestion degrades the service life of the engine parts, thereby decreasing the maintenance inspection intervals and the overall life of the engine. A decrease in engine life necessarily means an increase in costs of engine overhaul and replacement. These problems produce an unexpected cost burden to the U.S. Government. This present study aims to improve existing engine test requirements, better matching them to real-world conditions of sand ingestion. The desired final result is a high performance gas turbine engine with more predictable behavior in sand environments, and more cost effective to the government.

1.3 Research Focus

The focus of the present research is to compare and contrast melting behavior of natural and manufactured sand on electron beam physical vapor deposition (EB-PVD) TBCs.   The natural sands used in the present study are harvested from two sandy regions where extensive military operations take place; Yuma (Arizona) and Afghanistan. The composition of these two sands differ, as will be discussed later in this document. Several sands manufactured for engine testing are used in the present study.

The present study aims to address several questions:

1. How do various sands behave (i.e amount of glass phase formed and changes in color, shape, volume, and mass) as they are heated and transformed from loose particulates to molten glass?

2. How do the wetting characteristics of various sands differ on two representative TBCs as function of thermal energy?

3. To what extent do the various sands infiltrate the TBC with increasing temperature?

4. How do the results of the present study compare to observations from fielded hardware which has been subjected to CMAS attack?

1.4 Description of Terminology

One goal of the present study is to use representative materials and exposure conditions that closely mimic those seen in real-world operational service by military airplanes and helicopters. To distinguish between the various types of sand and CMAS glass discussed throughout the present study, the terms defined in Table 1 will be used.

Table 1: Sand terms presented throughout the present study.

Name	Description	Abbreviation
Natural Sand	Sands harvested from various geological locations. Compositionally different from region to region.	Nat-sand
Manufactured Sand	Specific types of minerals are combined and blended together. Composition and/or size distribution are based on customer requirements.	Mfg-sand
Natural CMAS	Thin brown glass deposits formed on turbine engine parts after being exposed to sandy environments. Composition consists of Ca, Mg, Al, and Si oxides and trace amounts of Fe and Ni oxides.	CMAS
Simulated CMAS	Created by combining oxide powders of the four principle elements found in turbine engine deposits (Ca, Mg, Al, and Si). Mixture is melted and then crushed to create a homogenous glass powder with a melting point of 1240 °C.	Sim-CMAS

II. Literature Review

2.1 Introduction

This chapter provides a review of relevant literature on the topics of turbine engines, sand composition and microstructure, TBCs, and their interaction. The chapter first discusses the turbine engine and the function of its various sections, specifically focusing on the turbine section and cooling schemes needed to maintain material integrity. The chapter then discusses regional compositional differences in natural sand in Afghanistan and in the Middle East region. This discussion is followed by a discussion of the sintering and melting mechanisms which lead to glass formation on TBC coated components in the gas turbine engine. Next, the composition, synthesis, and select failure mechanisms of the TBC system are described. Lastly, current studies of CMAS and TBC interaction are discussed.

2.2 Gas Turbine Engine

Throughout the history of military conflict the effects of the environment have played a major role in the ultimate success of failure of operations. Failure to understand the effect of the external environment has led to gas turbine engine failure. One present environmental issue challenging the US military is operation in sandy, dusty environments. Sand jams weapons, destroys bearings in vehicles, clogs air filters, and infiltrates into lubrication systems. Particularly worrisome is its effect on operational reliability and sustainment of gas turbine engines.

The gas turbine engine concept was first patented in 1922 to Guliume of France while the first operational engine was developed in 1937 by Sir Frank Whittle [5]. In 1941, a Gloyster airplane conducted the first flight with a turbine jet engine. The engine is made of five main sections: inlet, compressor, combustor, turbine and nozzle Figure 1.
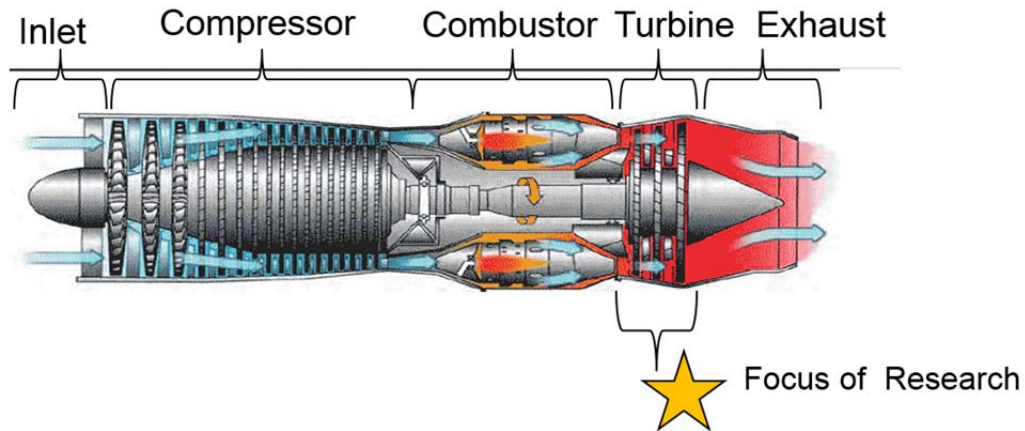
Figure 1: Cross section of gas turbine engine.

2.2.1 Inlet Section

The inlet is designed to import and guide intake air into the compressor with minimal total pressure loss [6]. Inlet design influences the drag forces on the aircraft and diffuses the air intake. Some different design configurations for the inlet include angled inlets, multiple inlets, and direct or indirect stream inlets. The design of the inlet depends on each vehicle's operational requirements determined by the range of speed and acceleration, the cargo capacity, operating environment and mission type. If required by operating environment, filters and particle separators, can be located in the inlet to reduce the amount of debris entering the engine [7].

9

2.2.2 Compressor Section

The compressor acts to pressurize the intake air using various stages of rotor and stator blades. Rotor blades attached to a rotating central shaft add energy to the fluid, while stator blades are stationary and attached to the case of engine. The goal of a compressor is to compress the most air possible with a minimal number of stages to maintain high efficiency throughout the operating range [6]. The higher the pressure in the compressor, the higher the turbine section temperature, thereby increasing the net work of the engine [6]. After the air is compressed it flows to the combustor section.

2.2.3 Combustor Section

In the combustion section the compressed intake air is precisely mixed with vaporized fuel and ignited to release the potential energy from the air/fuel mixture. The combustion section must efficiently operate at a wide range of external conditions – high and low elevations, high and low outside air temperatures, e.g. The thermal energy from combustion is ideally evenly distributed across the exit of the combustor section to prevent thermal stresses due to hot spots at the turbine inlet. Combustion gas temperatures have been reported to reach as high as 1900 ºC which is well above the melting temperature of the superalloy materials used in the combustion section [8]. To mitigate possible material damage, additional compressed air is used for dilution and cooling the combustion gasses.

2.2.4 Turbine Section

In the turbine section the energized combustion gases from the combustion chamber are received; the high-temperature, high-pressure fluid is accelerating through the stators and rotors sometimes referred to nozzles and blades, respectively. As is the case with the compressor, turbines can be configured either axially or centrifugally; axial turbines are typically used for aircraft. A portion of the energy from the combustion gasses is extracted in the turbine section and converted into shaft horsepower, which then drives compressor fan blades, gearboxes, turboprop shafts, turbo fans and any power output shafts that are present. Increased turbine inlet temperature has proven to reduce fuel consumption by increasing turbine efficiency [7]. Ideally, an engine designer would aim to increase the temperatures beyond the temperatures in current use, but designers are limited by the ability of turbine section materials to withstand thermal degradation. The first stage of nozzles and blades receive the harshest temperatures, with the most advanced engines allowing surface temperatures to reach as high as 1370°C [7]. As energy is extracted by the turbine each successive stage experiences a less severe thermal environment.

Historically, turbine engine designers have sought to improve performance and efficiency by increasing temperatures within the turbine section. These temperature increases have been achieved though improvements in materials and cooling. A nickel (Ni) based polycrystalline material was initially used because of its ability to retain properties at high temperatures. Further improvements were realized through better control over the microstructure of Ni. Achievement of columnar grain growth in Ni-

based superalloy materials enabled increased turbine engine temperatures. Further gains were achieved through the development of single-crystal materials.

To further increase combustion temperatures without exceeding the material property limitations of the Ni-based single crystal alloy, elaborate internal cooling passages and exterior coating techniques are used. The interior cooling allows cool air to extract heat from the bulk material. As the cooling air exits the component it creates a thin surface film protecting the component from the high combustion gas temperatures.

Also, metallic coatings called environmental barrier coatings (EBC) are commonly deposited on the surface of turbine blades and nozzles to protect against oxidation and salt corrosion. TBC systems provide a ceramic thermal insulation layer to the exterior surface of engine components. These coatings will be discussed in greater detail in section 2.6.

2.2.5 Exhaust Section

The last section of the turbine engine is exhaust, also referred to as the exhaust nozzle. The exhaust nozzle guides the high-temperature combustion gasses (cooled somewhat by the extraction of energy in the turbine), allowing them to pass through a designed geometry to create a high velocity, directional jet [9]. The nozzle is configured to provide the optimum expansion ratio and is often convergent. However, depending on the mission profile, a variable convergent/divergent nozzle could be necessary for maximum efficiency. Convergent/divergent nozzles are especially necessary if the nozzle is equipped with an afterburner which introduces additional fuel to reheat the

propelling fluid and thereby creating additional thrust [9]. Nozzles may also provide

thrust reversal and absorb the noise created as the hot propelling fluid enters the cooler

atmospheric environment [6, 9].

2.3 Sand

Some military operations have recently focused on environments where sand is

able to be ingested into gas turbine engines. These areas of operation include training

areas such as those in Arizona and California; allied air bases in Qatar, Saudi Arabia, and

Israel; and even Forward Operating Bases (FOB) in Iraq and Afghanistan. These desert

areas differ from non-desert areas because of the lack of moisture resulting from high

temperatures, lack of rain fall, geographical proximity to mountains, and/or long

distances from ocean wind currents. These factors produce regions that have extremely

dry ground surfaces and extremely dry wind currents. Wind currents transport small

particles of sand, silt, and clay which act as a source of erosion for local rock formation,

plants or any other solid material in its path. Wind currents also displace the sand, silt,

clay and eroded material from region to region. Therefore, while sand compositions in

various desert regions can be somewhat similar, regional geological differences can result

in significant differences in mineral content, particle size and presence of trace elements.

Saudi Arabian sands from a wide range of Saudi locations have been analyzed

and compared by Smialek et al. [1]. Some typical sand compositions can be found in

Table 2, representing samples from areas of operation by US Army groups such as: 3rd

Armored Cavalry Regiment, 24th infantry Division, 82nd Airborne Division and 101st

Airborne Division [1]. A map of the regions of operation can be seen in Figure 2.   From Table 2, quartz (SiO_2) and carbonate (CO_2) are the dominant minerals in Saudi Arabian dune sand, but in river bed sand calcite ($CaCO_3$) and dolomite ($CaMg(CO_3)_2$) are the most abundant minerals [1].

Table 2: Chemical Analyses of Selected Saudi Arabian Sands from Smaileck et al. [1].

	Dune Sand	20 µm Fines	River Bed Sand
SiO_2	90.8	52.4	12.3
CaO	1.5	17.4	25.9
Al_2O_3	2.5	14.3	5.2
Fe_2O_3	0.8	8.8	0.9
MgO	0.5	4.4	15.6
NiO	1.0	0.5	0.2
TiO_2	0.2	0.9	0.2
Na_2O	0.2	‡	0.2
K_2O	0.5	‡	0.1
CO_2	5.6	NA	39.4
SO_2	1.3	NA	8.5

NA—not analyzed
* Emission spectroscopy, normalized to 100% oxide.
† From BFLRF No. 294.⁴
‡ Not found.

The Origins of Sand Analyzed by Smialek et al.

101 st
82 nd.
IRAN
IRAQ
3 rd ACR
GULF
24 th
KUWAIT
SAUDI ARABIA
King Fahd Airport
Dhahran
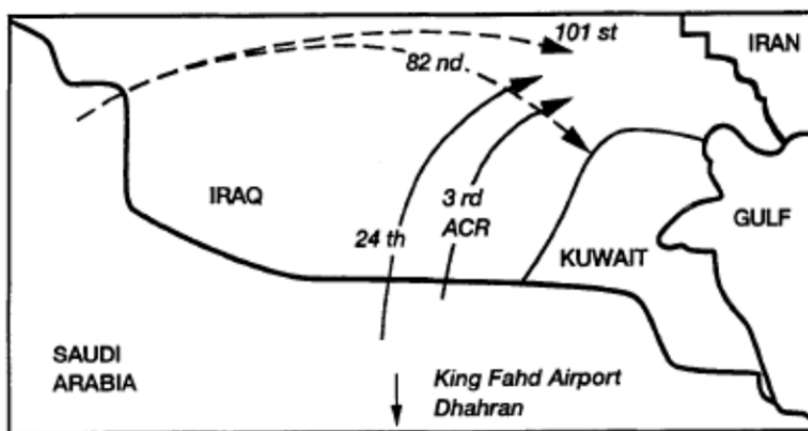
Figure 2: Operating locations of 3rd Armored Cavalry Regiment, 24th Infantry Division, 82nd Airborne Division, and 101st Airborne Division [1].

In a study by de Wet et al. [2] five sites were sampled near Saudi Arabia. The results of the sand compositions are in Table 3. This analysis shows that quartz is a very common mineral found in sands. Other minerals present contain the elements Calcium (Ca), Magnesium (Mg), Aluminum (Al), Sodium (Na), Potassium (K), and Sulfur (S).

Another soil characterization study by Kelley et al. [10] reported on soil characterization of Iraq and Afghanistan samples. In Iraq partially cemented gypsum ($CaSO_4 \cdot 2H_2O$) was present under the windblown surface layer. The twelve Afghanistan sampling sites found calcium carbonate was the most dominant mineral, with significant gypsum amount found only near the Helmand Province. In both Iraq and Afghanistan research found that silt and clay sized particles were more abundant than soil-sized particles. A scale of relative sedimentary sizes can be found in Figure 3 [11].

Table 3: X-ray diffraction analyses of sand samples sites near Saudi Arabia [2].

Mineral	Sinaiyah	Bahrain	Dubai	Abu Dhabi	Doha
Quartz $\alpha-SiO_2$	vs	vs	s	vs	w
Calcite $CaCO_3$	w	w/m	vs	s	w
Aragonite $CaCO_3$	-	m	-	-	-
Dolomite $CaMg(CO_3)_2$	w	w/m	w	w	m
Gypsum $CaSO_4.2H_2O$	-	-	-	-	vs
Albite $NaAlSi_3O_8$	m	w	w	m/s	-
Microcline $KAlSi_3O_8$	m	w	w	w	-
Diopside $CaMg(SiO_3)_2$	-	w/m	-	-	-

Amount present indicated by; vs = very strong, s = strong,
m = medium, w = weak, vw = very weak
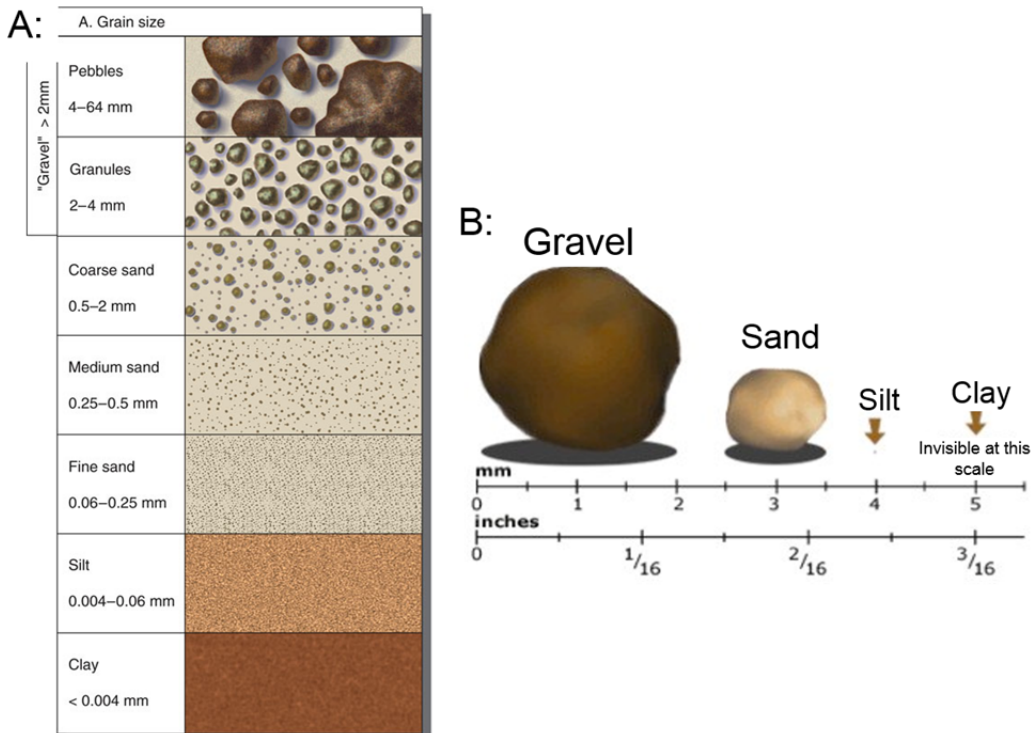
Figure 3: Relative scale of sedimentary grain sizes found in soil. Image A shows the categories of soils and their corresponding sizes. Image B shows individual grains relative to each other [11, 12].

16

Advanced Spaceborne Thermal Emission and Reflection Radiometer (ASTER) studies were conducted on the Kabul Basin in order to measure relative mineralogy. The imaging scanned the relative abundance of ten different minerals which can be viewed in Figure 4 and Figure 5. The dominant minerals found were of quartz, carbonate, feldspar, ferric iron, and smectite clays [13]. Gypsum was not found through the ASTER mapping because unlike the Helmand basin the Kabul basin is an open basin. Whether a basin is closed or open depends on its drainage characteristics which can affect the type of minerals present in the soil.
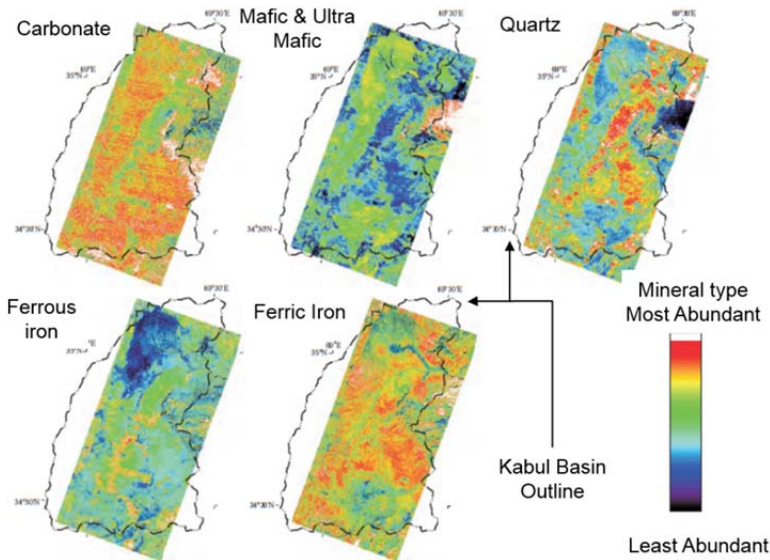
Figure 4: Relative abundance of carbonate, mafic and ultra mafic, quartz, ferrous iron, and ferric iron minerals present in Kabul Basin, Afghanistan from ASTER imaging [13].
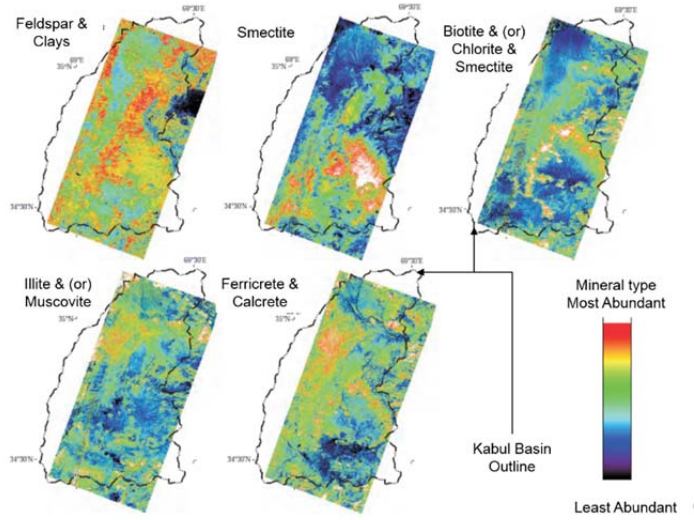
Figure 5: Relative abundance of feldspar & clays, smectite, biotite and (or) chlorite and smectite, Illite and (or) muscovite, and ferricrete and calcrete minerals present in Kabul Basin, Afghanistan from ASTER imaging [13].

Lastly, Englebrecht et al. **[14]** conducted a study of air-suspended particulate matter (SPM) chemistry, size, and concentration within Middle Eastern areas under the US Central Command (USCENTCOM) Area of Responsibility (AOR). These airborne particles comprise of the majority of material ingested into military aircraft engines. The study used suspended particulate filters, surface samples, and bulk samples at 15 different geographic sites.

The filter testing used a total suspended particle matter (TSP) filter that captured particles larger than 10 μm, a PM_{10} filter that collected particles larger than 10 μm in diameter, and finally a $PM_{2.5}$ filter which collects samples larger than 2.5 μm in diameter. Relevant findings with respect to the particulate sizes found during the study are listed below:

- The country with the highest average concentration of TSP was Iraq with Kuwait in second. The lowest average concentration of TSP was Djibouti **[14]**.

- The ratio of $PM_{2.5}$ particles to PM_{10} particles reveals that most of Iraq, Kuwait, UAE, and Bagram, Afghanistan airborne particles are similar to each other and similar to deserts in the southwestern U.S **[14]**.

- Khowst, Afghanistan reportedly has the largest amount of fine airborne particulates, more than any other sampling site **[14]**.

- The total contribution from clay-sized particles was minimal enough to be considered insignificant for further study [14]**.**

- During the $PM_{2.5}$ trace metal analysis, lead was the most abundant species in Iraqi cities. Its presence is attributed to battery manufacturing, burn piles, and leaded gasoline used in the cities **[14]**.

A chart of the filtered particles found and the chemistry of those filtered samples can be seen in Figure 6. This chart provides a comparison as to which elements are present in smaller and larger particles. It was found that during dust blown events sulfate minerals have a much higher percentage of abundance in the $PM_{2.5}$ while CaO has a much higher abundance in the TSP filter. Therefore, the larger sized CaO is easier to filter and should only be a concern at low altitude; whereas the smaller sized sulfates remain a concern even at high altitudes and are difficult to filter. Additional analysis of

bulk sand samples separated and analyzed particles less than 38 μm. The results of chemical and mineralogical analyses are listed below:

- The Djibouti samples were dominated by igneous minerals due to the basaltic volcanic activity in the region [14].

- Afghanistan sample sites revealed quartz, feldspar, mica, calcite, and trace amounts of chlorites.

- In Qatar and UAE the majority of minerals found were calcite, quartz and feldspar with some chlorite and clay [14].

- Qatar samples revealed traces of volcanic material such as hornblende and ilmenite. [14]

- Baghdad, Taji, Balad, and Tikrit (Iraq) were mostly concentrated in quartz, calcite, feldspar with minor amounts of gypsum and other minerals. In Al Asad dolomite was the abundant mineral instead of calcite. In Tallil, an unexpected, yet notable amount of gypsum was found and is thought to be present due to windblown sand from a nearby gypsiferous desert [14].

- Kuwait contained larger amounts of quartz and lesser calcite than most other cities while more silts were found compared to Iraq sites.

The sands of the countries listed above were compared to the sands of other world deserts, as seen in Figure 7. One notable fact seen from this chart is the sand from countries previously mentioned is more abundant in CaO than the sand from the other

20

deserts around the world. Also, SiO_2 is more abundant in the sand from other deserts than the sands collected in this study.
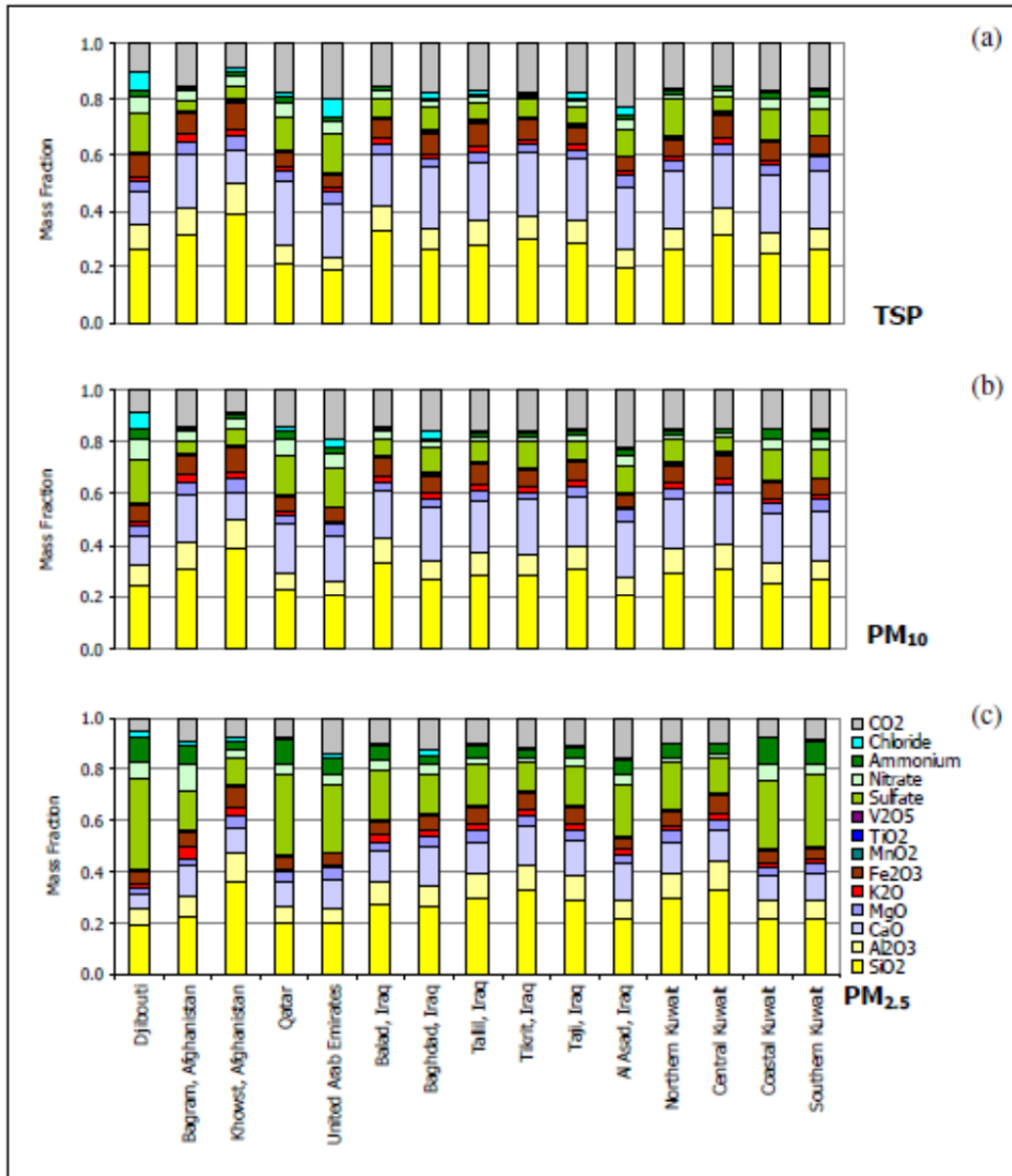
Figure 6: The major chemistry for (a) TSP, (b) PM$_{10}$, (c) PM$_{2.5}$ as mass fractions from Englebrecht, et al. [14].
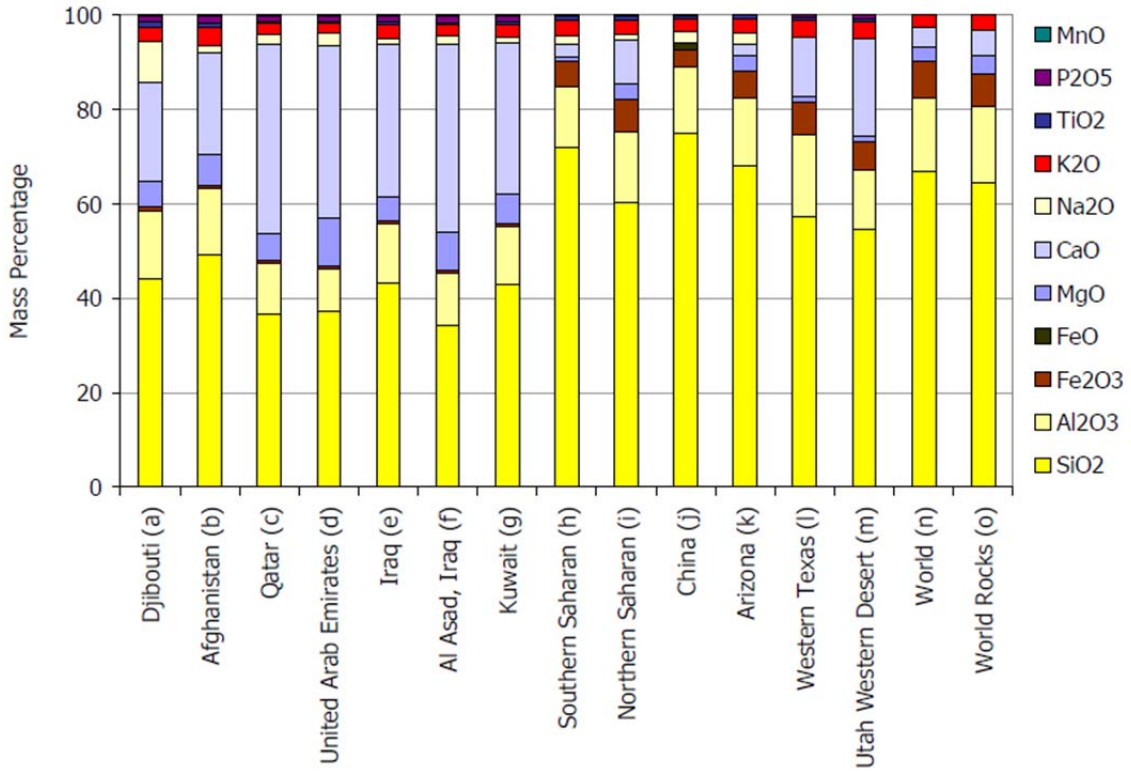
Figure 7: Chart compares mean TSP dust from the Middle Eastern countries with other world region composition studies [14].

2.4 Consolidation and Melting of Ingested Sand

2.4.1 Overview

When a turbine engine heats the mixture of granular minerals that make up sand, the mixture may consolidate due to sintering, or transition to a molten liquid if heated to its melting temperature (T_M). Sintering is the process by which particles consolidate and strengthen below their T_M. An understanding of sintering processes like solid state and

liquid phase sintering is crucial to understanding the behavior of sand at elevated temperatures; it also provides insight into how and why different mixtures of sand behave differently.

Sand is a mixture of various minerals, each having a discrete T_M. Although many sands may have similar compositions of major elements like Si or Ca, sands rarely exhibit the same melting behavior as a whole. How and why this difference occurs is directly applicable to the present research. In particular, the presence of "flux compounds" within sand can lead to dramatic reductions in the temperature at which molten sand forms, causing (for example) a quartz containing sand to form molten liquid at temperatures that are hundreds of degrees Celsius cooler than quartz T_M.

2.4.2 Sintering

Sintering is a thermally-activated process whereby a collection of particles consolidate and densify at temperatures below the melting point of the particles. The sintering process is dependent on temperature, time, pressure, atmosphere, and material properties. Material properties could be further broken into physical and chemical variables. Physical variables include shape, size, size distribution, and existence of agglomerations. Chemical variables include: composition, presence of impurities, stoichiometry, and homogeneity.

Sintering can be further divided into solid state and liquid phase. Solid state sintering occurs between solid particles when heated to approximately 50 - 90 % of their melting point. Liquid phase sintering, on the other hand, uses a liquid to facilitate the

sintering process of the materials. A more in-depth description of solid state sintering

and liquid phase sintering will be provided in the following sections.

2.4.2.1 Solid State Sintering

Solid state sintering is a thermally-activated process whereby a collection of solid

particles consolidate, densify, and form a single solid body at temperatures below the

melting point of the particles. Figure 8 illustrates the process of sintering of a body of

four individual particles. Initially the particles are in touching contact, but under

sintering conditions, material travels to these points of contact between neighboring

particles, forming grain boundaries (GB) and changing pore shape and size. The area

where two particles form a GB between each other is known as the sintering neck. The

transport mechanisms that lead to the formation of a sintering neck can be seen in Figure

9. Necks form as a result of a combination of 6 transport mechanisms:

1. Surface diffusion: atoms on the surface of particles travel along the surface
   toward the sintering neck, deposit, and thus increase the size of the neck.

2. Surface-Lattice diffusion: atoms from the surface can travel through the bulk
   lattice and deposit at the growing sintering neck.

3. Vapor Transport: atoms on surface can vaporize and preferentially condense
   in the neck region.

4. Grain Boundary Diffusion: atoms at the GB can travel along the GB to the
   growing sinter neck.

5. Grain Boundary-Lattice Diffusion: atoms at the GB can travel through the bulk lattice and deposit at the neck.

6. Bulk Flow (Plastic Flow): Material from the bulk of the particle can diffuse to the surface at the sintering neck.

It should be noted that mechanisms 1-3 above effectively reorient surface material from one surface region to another, but do not remove material from between the particle centers and deposit it on the surface. Consequently, mechanisms 1-3 result in microstructural changes but not shrinkage/densification. In mechanisms 4-6 above, material from the "interior" of the particles, between the two particle centers is removed to the surface. As such, the particle centers approach one another and densification/shrinkage occurs.

As sintering progresses in three dimensions, the interparticle spaces can become closed off, thus creating pores. Continued sintering and the diffusion of the pore atmosphere out of the body can reduce the size of or eliminate pores. Some pores are stable, however, and are not eliminated via sintering and coarsening mechanisms
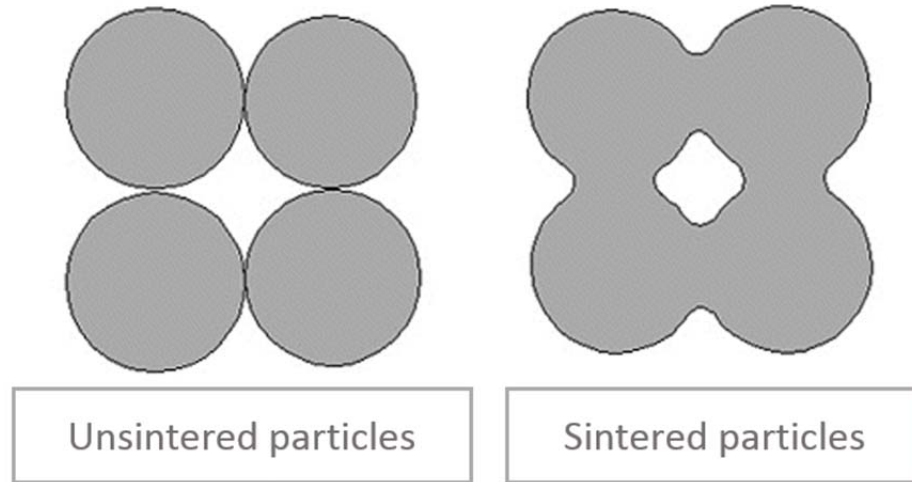
Figure 8: Basic evolution of sintering between particles
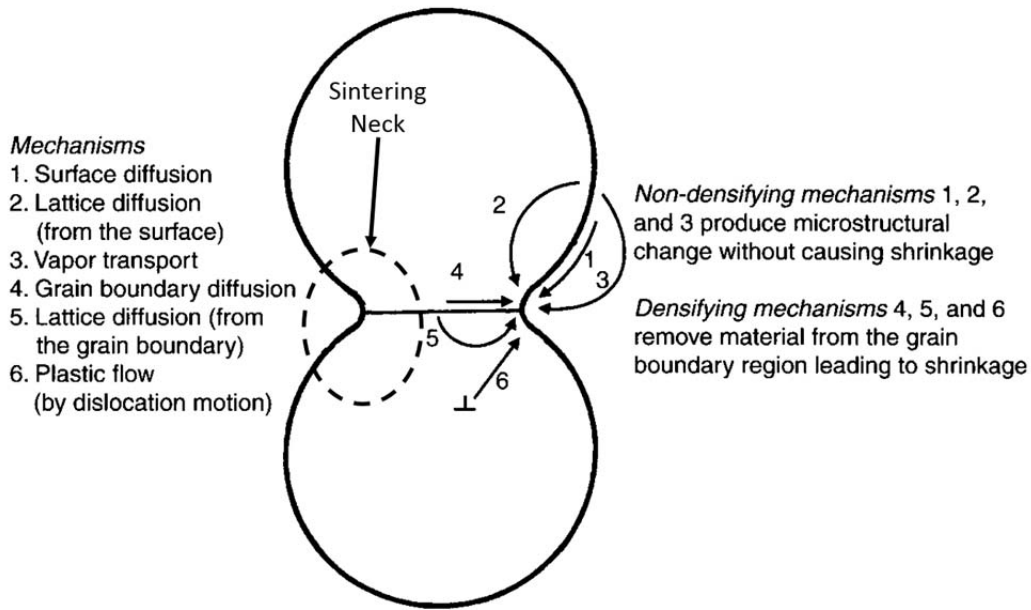
Figure 9: Mechanisms of necking between two particles during sintering [15].

In a sintered body, transport mechanisms similar to those described above can result in a net increase in grain size. This process of grain coarsening is often referred to

as Ostwald's Ripening. Ostwald's Ripening is the consumption of smaller grains by larger grains within a matrix of soluble particles [16]. The consumption of smaller grains is driven by the decrease in the interfacial free energy. The grain growth rate, U, is the energy it takes to jump an atom from one side of the grain boundary to the other. It can be described as

$$U = U_0 \exp\left(-\frac{E_U}{RT}\right) \tag{1}$$

where E_U is the activation energy, R is gas constant, and T is temperature [16]. The grain boundary velocity (V) can be described as

$$V = M \cdot F \tag{2}$$

where M is grain boundary mobility and F is the driving force for grain boundary migration [17]. Ostwald's Ripening can be observed in Figure 10.
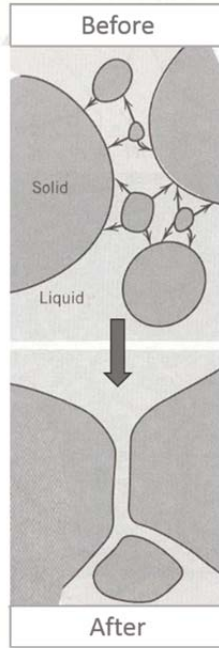
Figure 10: Example of Ostwald's Ripening [17].

The densification and coarsening are a result of surface free-energy reduction within the system. Surface free energy is the free energy, G, per unit area of surface interactions. Surface tension, γ, between the interfacial surfaces of the material can be related to the free energy and internal energy, E, by

$$\gamma = \left(\frac{\partial E}{\partial A}\right)_{S,V,n_i} = \left(\frac{\partial G}{\partial A}\right)_{P,T,n_i} \tag{3}$$

where the entropy ,S, volume, V, pressure, P, and temperature, T, are independent variables [16]. In order to reduce total surface energy, the microstructure of particles will change, seeking to (1) preferentially reduce the amount of "high energy" surface in favor of additional "low energy" surface; and (2) reduce the overall surface to volume ratio.

In the case of sand at high temperatures, this energy reduction is accomplished by

elimination of high energy solid/air interfaces and replacing them with lower energy solid/solid interfaces. Sintering necks are created through this process, reducing the surface area but increasing grain boundary area. Additionally, coarsening serves to reduce the total grain boundary area, further reducing the free energy. The diffusion of vacancies (driven by pressure) serves to reduce the size of pores, or eliminate them altogether, further reducing system free energy.

2.4.2.2 Liquid Phase Sintering

Liquid phase sintering involves the presence of transient or persistent liquid that can wet the surface of, and eventually dissolve, the solid particles. The liquid aids in the processes of densification and coarsening of the solid particle within the body. Liquid phase sintering is shown in Figure 11. Initially, the particles at low temperatures are not surrounded by any liquid, but as temperature increases (position 1) a liquid forms, wetting solid particles, often at temperatures much below the T_M of the solids. Once enveloped in liquid, rearrangement and pore elimination can occur, further shrinking the body. At position 2 porosity has been largely eliminated and the majority of shrinkage has occurred. Additionally, the enveloped solid particles are being dissolved into the liquid and re-precipitating.

At position 3, the body is in a lower energy state than the initial compact. Additionally, this liquid phase sintering process progressed at a more rapid rate than solid state sintering due to accelerated material transport enabled by the liquid phase. In

general, in liquid phase sintering the ratio of liquid to solid determines the rate and extent of sintering.
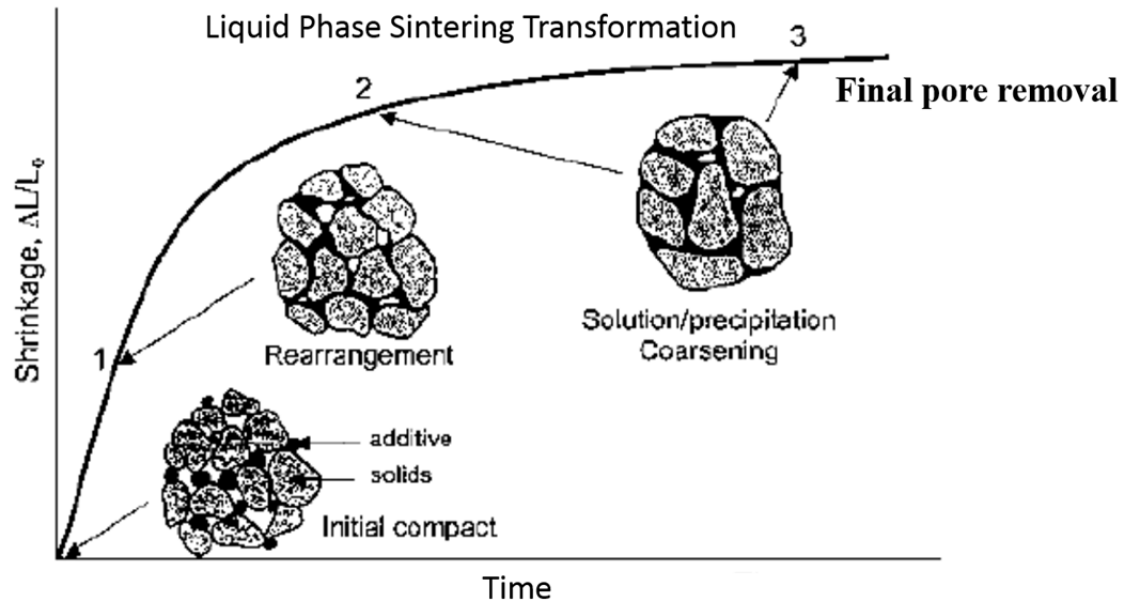
Figure 11: Liquid phase sintering process of shrinkage as a function of time [17].

If a large degree of melting occurs, a sufficient amount of liquid exists to fill all voids within the body, resulting in the densification of the body. Typically in the melting of sand the liquid bonding together the body is a viscous liquid silicate that often drives sintering in silicate systems. The factors influencing liquid formation are surface tension, viscosity, particle size, and composition [16]. Each variable influences the rate of densification within the body. Kingery et al. [16] state the primary variables critical to the rate of densification when processing silicate materials are the particle size and viscosity. For example the rate of sintering is increased by a factor of 10 when the particle size is changed from 10 μm to 1μm. Viscosity in soda-lime-silica glass changes

by a factor of 1000 over a 100 ºC change. The densification rate changes by a factor of

1000 also. The viscosity is a function of temperature and composition, therefore to

increase densification the temperature must be increased and/or the composition must be

changed to lower viscosity. Composition can be altered by the addition or subtraction of

a flux agent.

The above-described processes directly relates to the present study, in which

mixtures of particles of sand comprising various minerals are exposed to extreme high

temperatures. Most of the minerals that make up the bulk of sands have high T_M values,

over 1600 °C for quartz, for example. The presence of small amounts of fluxes –

compounds that are found in sand but not in resulting CMAS – however, can lower the

melting point behavior of sand to below 1200 °C.

2.4.3 Flux

Flux, in the context of this research, is an oxide compound that lowers the

softening and melting temperatures of other materials. Flux dissolves surface molecules

of neighboring oxides. The viscosity of a material is affected by the amount of flux

present within the material's composition. It essentially helps the material to flow.

Crystalline solids – such as the crystalline minerals contained in sand – tend to have

distinct melting points due to their ordered, repeated bonding. Unlike crystalline solids,

amorphous glasses does not have a distinct melting point because bonding characteristics

vary throughout the material. Pure quartz will melt to liquid at a range of 1550 –

 1705 ºC but with the introduction of a small amount of a flux like Na_2O, the melting

temperature will be reduced.   This shift occurs because the Na_2O chemically breaks the

Si and O bonds, disrupting the ordered crystal. An illustration can be seen in Figure 12.

This behavior is in agreement with the "mixed oxide effect" which states that the greater

the variety of oxide minerals mixed together, the lower the melting point of the mixture

[16]. Figure 13 shows viscosity of different types of glass compositions. As the non-

silica compositions increase in percentage, the viscosity of the glass is reduced and

melting occurs at reduced temperatures. Some of the common flux categories are

potassium (K), sodium (Na), lead (Pb), and lithium (Li). Potassium oxides are commonly

found in volcanic ash. Lead oxides are known to be toxic, but their usefulness in

providing clarity to glass has led to their use in the preparation of optical lenses.   Fluxes

are also of great importance in the production of commodity ceramics (dishes, toilets,

spark plugs, e.g.) and are key to the performance of the surface glaze that is applied in the

final processing steps. Many fluxes exist and in general, any new oxide introduced into a

material mixture has the potential to act as fluxing agent in glass-forming applications.
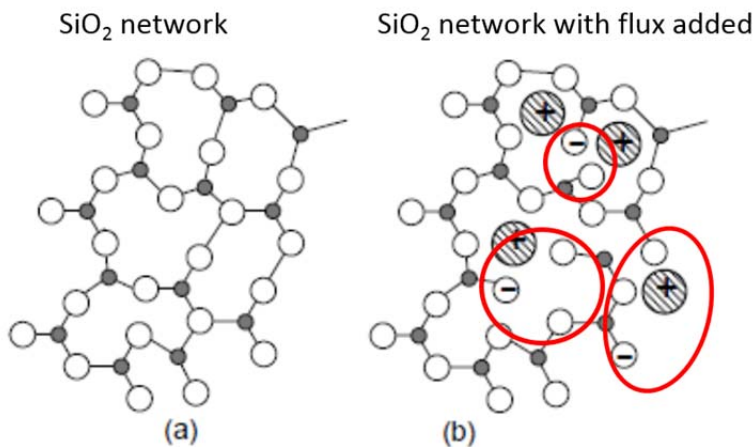
Figure 12: (a) Illustrates a quartz network without the addition of flux.
           (b) Illustrates the bonds broken (inside the red circles) due to the addition of a flux agent in the same quartz network [18].

Type of Glass	Composition (% by wt)						
	SiO_2	Na_2O	K_2O	CaO	MgO	B_2O_3	Al_2O_3
Silica glass	99.5+						
96% silica	96.3	<0.2	<0.2			2.9	0.4
Borosilicate	80.5	3.8	0.5			12.9	2.2
Soda-lime	72	17		9	4		1
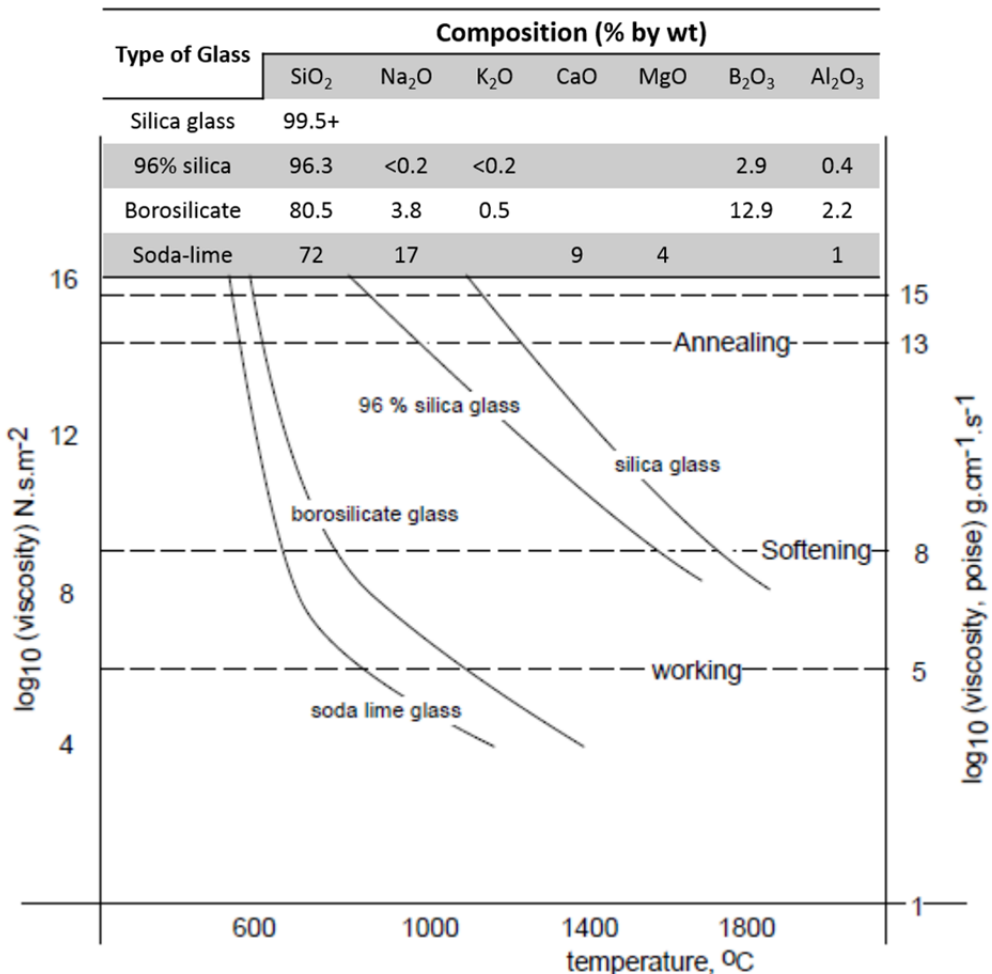
Figure 13: A comparison of different glass compositions and their viscosity with respect to temperature. [18].

2.5 Logistic Consequences of Ingested Sand

Sand creates significant sustainment and logistical problems for aircraft. When operating within sand environments, many parts of the vehicle are negatively affected,

33

the degree of which depends on the environmental conditions. Windy days can cause "sandblasting" to occur on outer surface coatings, tail numbers, and decals. Radomes and windshields can become pitted and no longer transparent. Any moving components such as bearings, fittings, actuation joints and their lubricating greases can collect the sand, eventually leading to premature wear and failure

The sand can also be ingested into an aircraft's turbine engine. Here the sand can have differing adverse effects in the various sections of the engine. Sand entering an engine's inlet could collect in gear boxes simply by slipping through unfiltered vents, cracks or covers. As sand is only partially filtered by particle separators as it enters the engine, sand that makes it through the filter may enter cooling channels [1] or travel to the compressor. The compressor's rotors and stators experience erosion as individual sand grains grind away on obstructing surfaces.

Fine particles of sand or ash can collect in the combustor section, which can in turn clog fuel injection ports and alter the air/fuel mixtures. Sand experiences extreme temperatures as it enters the combustor, and continues into the turbine section. Once heated to extreme temperatures, sand can then transform into a molten fluid and contact the leading edge of the turbine's nozzle and blades. This happens especially in the first stage where temperatures are the hottest. Once in contact with the surfaces of leading edges, stagnation edges or outer liner edges, the molten fluid wets parts and coatings, negatively affecting the material and the flow of combustion gasses across the blades. Sand attack ultimately results in a decrease of engine life and an increase of maintenance hours for the military or commercial operators. Dealing with the consequences of sand

attack also impacts aircraft availability and mission planning, raising great concern in the military community.

As stated before, sand ingestion has effects on many sections of the engine. However, the main focus of the present study will be its effect on the turbine section. The temperatures in the combustor and turbine sections, in conjunction with the presence of fluxes in ingested sand, can cause sand to become molten glass. The sand's particular combination of dominant and trace minerals – including the presence or absence of fluxes – affects its melting point. Therefore, a regional understanding of sand compositions can be very useful to those who design, operate, schedule, and maintain turbine engine vehicles. This information can be taken into consideration for overall operation of the vehicles in terms of their usage hours, maintenance inspections, and engine life expectancy. Most high temperature, high efficiency turbine engines use techniques like cooling channels and TBCs to withstand extreme temperatures. Contact with molten fluid from sand will decrease the efficacy of the cooling techniques and the life expectancy of the engine.

2.6 Thermal Barrier Coatings (TBCs)

The TBC is a multilayer system that provides a thermal insulating barrier of protection to blades, nozzles, and/or the inner wall lining of the engine. The multiple layers of the TBC consist of a superalloy substrate with a metallic bond coat (BC) deposited on top. A thermally-grown oxide (TGO) layer of alumina scale forms on top of the BC and acts as a binding agent for a final layer of a ceramic top coat [19] [20]. The

multiple layers can be seen in Figure 14. Each layer has a specific function as well as a set of compatibility requirements.
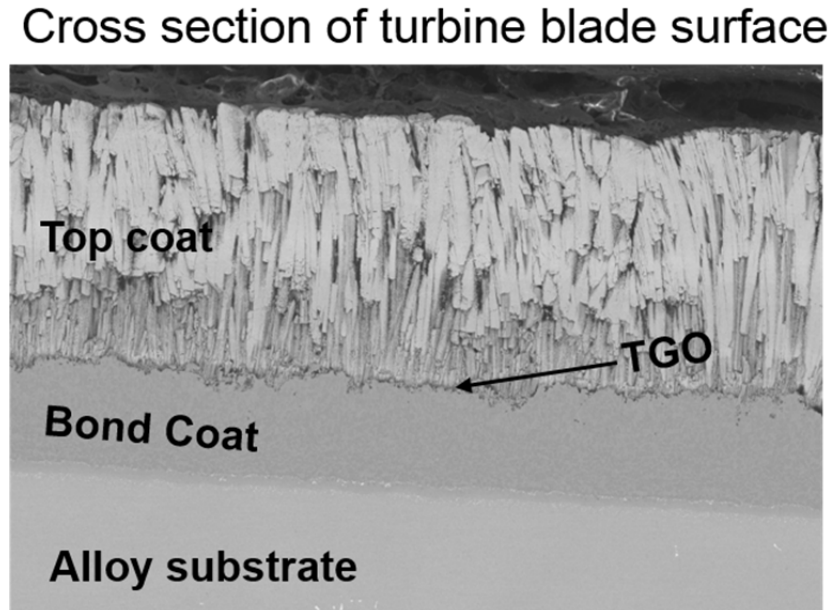
Figure 14: Cross-section of an EB-PVD TBC.

2.6.1 Alloy Substrate

The superalloy base layer must be a material that has can have the strength to maintain a load at temperatures from 850 ℃ to 1250 ℃ for the complete life cycle of the engine. Therefore the substrate alloy must have satisfactory characteristics in rupture strength, creep, and fatigue strength at these temperatures [7]. Nickel-based superalloys meet these requirements through the microstructural mechanism of precipitate-hardening, with gamma-prime phase precipitates in a gamma matrix. Cobalt-based superalloys are strengthened by solid solution strengthening and through carbide formation [19]. While

high-temperature strength, creep, fatigue are of vital importance they are not the only properties to consider for the substrate at these high temperatures.

Hot corrosion, oxidation, and erosion wear are other considerations in the design of the substrate. The addition of Al and chromium (Cr) increase the substrates resistance to hot corrosion and oxidation by creating a protective oxide scale on the surface of the substrate. Above a certain level of additional alloying, however, Al or Cr will serve to degrade other material properties such as fatigue or creep resistance. Therefore corrosion, oxidation and wear are commonly approached through the use of EBC or TBC coatings. The superalloy's coefficient of thermal expansion (CTE) is taken into consideration in selecting and designing these coatings, in order that the CTEs of the coating and the substrate are similar. The matching CTEs will reduce the amount of thermal strain between the substrate and coatings during operation.

2.6.2 Bond Coat

The BC is a thin metallic coating that creates a protective oxide scale layer on its surface when subjected to high temperatures [19]. The layer of oxide scale forms by oxidizing, Al, atoms from the BC onto the surface, thereby protecting the substrate from oxygen and corroding salt. Bose [19], reports that in order for the BC to provide continued protection it must meet requirements such as:

- The oxide scale must grow at a slow rate.

- The oxide scale must adhere well to the BC.

- There must be a high concentration of scale-former present in the BC composition.

- The oxide scale must have a uniform thickness.

- No expected or sporadic phase changes should occur within the BC.

- Diffusion of BC and substrate elements should occur slowly at use temperatures.

- CTE should be similar to substrate.

- Must be able to withstand creep, fatigue, impact loading of the surface.

The BC can be applied as a diffusion coating or an overlay coating. The metallic elements for the coatings are vaporized and transported, depending on processing type, to the substrate. Diffusion coating elements are dependent on the composition of the substrate. This is because the diffusion of the substrate elements interact with the BC elements producing a metallic layer of the combined elements. As an example, an aluminum coating on a Ni-based superalloy substrate can produce a nickel aluminide coating. This occurs due to the discontinuity in thermodynamic equilibrium between BC and the substrate's composition. Platinum aluminide diffusion coatings deposited using Chemical Vapor Deposition (CVD) retain the greatest resistance to high temperature oxidation and corrosion compared to pure Al, Cr, and S elements. It doubles the resistance of type 1 hot corrosion, and quadruples oxidation resistance compared to pure aluminum [19].

In order to gain additional corrosion, oxidation, and CTE-matching properties additional elements may be needed. The dissolution of other elements in β-NiAl can be

very difficult to achieve, therefore, overlay coatings are commonly used to add the additional elements desired for the design.   Overlay coatings consist of MCrAlX composition. M normally consists of Ni, Co, and Fe elements and X normally consists of oxygen-reactive elements like Zr, Hf, Si, and Y [19]. Avoiding the phase transformation from $\beta + \gamma$ to $\alpha + \gamma'$ is a major consideration in composition selection. The wrong composition can cause the BC to significantly decrease in volume if the coating transforms to $\alpha + \gamma'$ phase as it cools to 850 ºC. Overlay coatings are normally applied by various processes such as: spray, arc, and physical vapor deposition (PVD).   These processes produce specifically unique microstructures that affect grain size, porosity, phase distribution, and texture of the coating.

2.6.3 Thermally Grown Oxide Layer

The third layer is the oxide scale layer that has been previously mentioned in the BC section.   Within the context of the TBC system it is commonly referred to as the thermally grown oxide (TGO) layer and it also gains a new function because of its interaction with the top coat. An extremely effective TGO layer forms pure α-Al_2O_3. Pure alpha alumina, bonds strongly to the top coat while continuing to slow the diffusion of oxygen into the substrate. The TGO layer oxidizes during thermal cycling as oxygen diffuses through the oxygen-rich ceramic top coat [21]. Oxidation may occur as early as the preheat stage of ceramic deposition, but the most common rate of growth occurs when subjected to its normal operation temperatures. The most reliable TGO will oxidize at a very slow rate, growing defect-free, uniformly across the BC [21].

As the Al atoms are depleted from the BC other metallic oxides, known as spinel's (Ni,Co)Al$_2$O$_4$, begin to form [19, 20]. The binding strength of the spinel is less than α alumina thereby increasing the likelihood of spallation. Imperfections, voids, or cracks in the TGO also act as crack propagation sites that increase the likelihood of spallation [20]. Experimental and field research suggests that TBC spallation often occurs when the TGO thickness is between 6-7 μm [19].

2.6.4 TBC Top Coat

The ceramic top coat is a thermal insulator to turbine section parts due to its low thermal conductivity. The combination of cooling passages, which remove heat, and low thermal conductivity result in temperature gradients from the ceramic top coat to the substrate surface that have values of 50-150°C [7]. Yttria-stabilized zirconia (YSZ) is the preferred insulating ceramic because of its low thermal conductivity of 2.3 W/m·K at 1000°C [21]. The low thermal conductivity properties are attributed to a high concentration of oxygen vacancies which increase the distance heat conducting phonons travel between atoms [20, 21]. This also suppresses, or normalizes, high temperature spikes that may occur in the coatings environment.

YSZ is especially strain tolerant in the TBC system because its CTE is similar to that of the substrate, to the BC, and to the TGO. Similar thermal expansion coefficients are necessary to prevent delamination from forming within the top coat or nearby interfaces upon cooling [19, 21]. YSZ is stabilized with seven percent weight yttria (Y), referred to as 7YSZ, in order to retain the desired CTE over a wide range of temperatures.

A phase diagram of ZrO_2 stabilized with Y over a various temperatures can be seen in

Figure 15.   At a lower percentage of Y a phase transformation occurs upon cooling. This

transformation from tetragonal to monoclinic phase increases the volume of YSZ by 3 -

 5% [19]. At higher concentrations, YSZ is dominated by the cubic phase, especially at

higher temperatures. The cubic phase has been found to have reduced strength and

durability than the tetragonal phase [19]. The tetragonal phase is the most durable and

has the highest strength while retaining a level of strain tolerance required by the TBC

system.
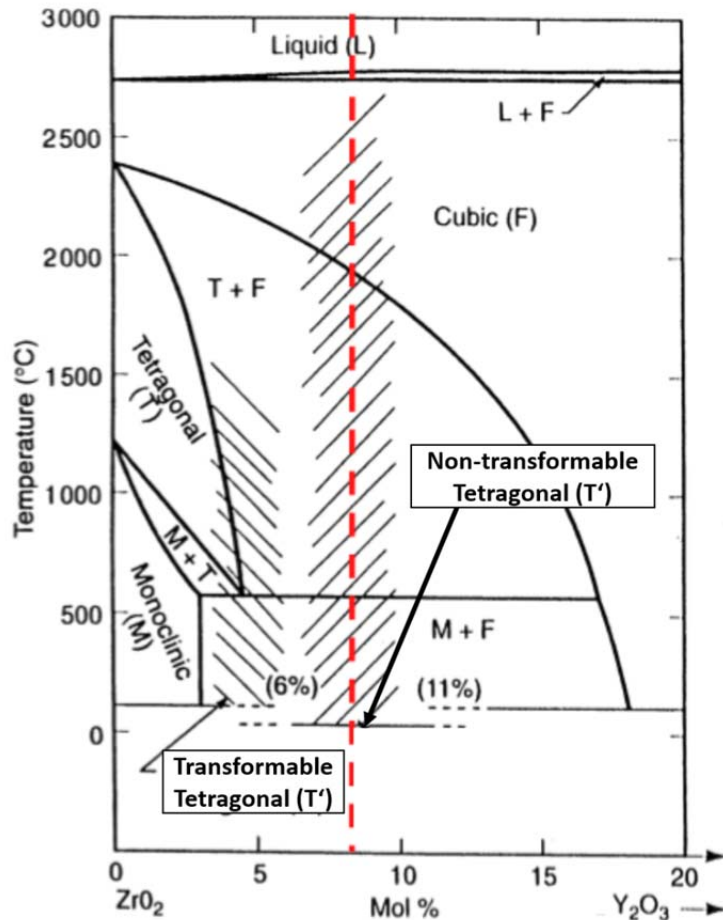
Figure 15: Phase diagram of ZrO_2 –Y_2O_3. Red line indicates where 7 % wt YSZ composition lies [22].

2.7 TBC Processing Techniques

Several processing techniques exist to deposit the ceramic top coats. Many of the processes are interchangeable with those used for metallic BCs, except higher melting temperatures are needed for the ceramics. Typical deposition techniques include air plasma spray (APS), low-pressure plasma spray (LPPS), solution precursor plasma spray (SPPS), electron beam physical vapor deposition (EBPVD), flame spray, high-velocity oxygen fuel (HVOF), electric arc spray, and various others. The APS and EB-PVD are the two most common commercially used processes. The difference in microstructure resulting from these tow deposition methods can be seen in Figure 16.
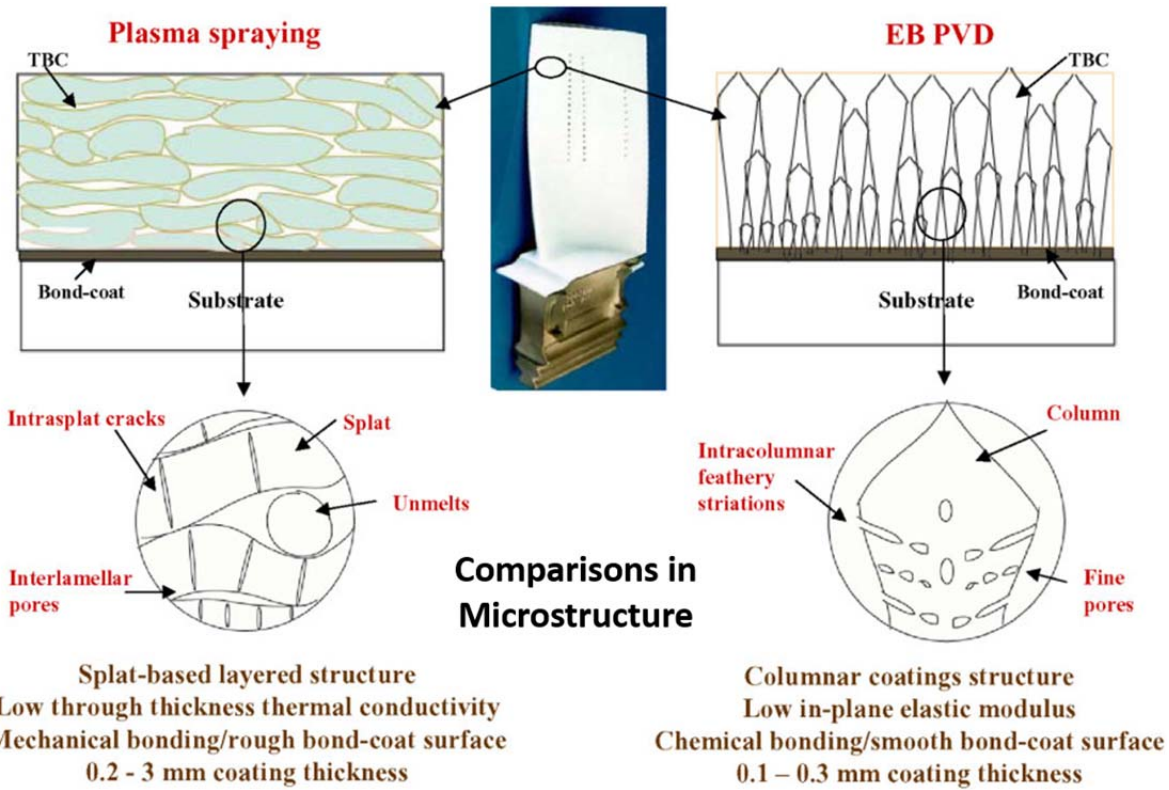
Figure 16: A comparison of APS coating microstructure (left) and EB-PVD coating microstructure (right) [23].

2.7.1 Air Plasma Sprayed Deposition

APS uses a plasma gun to melt a ceramic powder and transport it to the substrate. The melted powder upon deposition on the surface of the substrate, compresses axially and expands radially, a process referred to as "splatting" as seen in Figure 16 [19, 21]. The structure within the individual flattened ceramic "splats" is crystalline with columnar grains that are the height of the splat. The deposition of multiple random pancake-like splats onto the target creates a microstructure of mechanically-interlocked 7YSZ layers.

This type of microstructure contains many voids resulting in a 10 – 25 vol % porosity of the layer [19, 21]. The added porosity and splat grain boundaries result in

lower thermal conductivity and improved strain tolerance. Cracks often form in APS due to causes such as: (i) high residual stresses development upon contact with a much cooler substrate during application, (ii) splat grain boundaries, and (iii) undulation of the TGO layer [20]. The orientation of cracks within the coating can relieve stresses during thermal cycling, and also improve strain tolerance and durability. For example, cracks parallel to deposition surface decrease thermal conductivity while through cracks, perpendicular to deposition surface, relieve stresses during thermal cycling.

The bonding strength of the APS is weaker than that of EB-PVD, due to the nature of the mechanical interlocking of the splats. This makes the coating less resistant to impacts from foreign object debris (FOD). As a result, APS deposition methods are more commonly limited to use on stationary parts. The most notable advantages of APS are ease of application onto complex part geometries and lower cost compared to EB-PVD [19] [21].

2.7.2 EB-PVD Deposition

EB-PVD is another preferred commercial application process. In EB-PVD, an electron gun (commonly called an E-gun) is used to vaporize ingots of ceramic in a vacuum chamber. The ceramic vapor then condenses on to the part [19, 24]. Due to complex part geometries within a part like a turbine blade, it is required that the part be rotated, tilted, or manipulated to achieve a uniform layer of the ceramic. As the vapor attaches to the target it grows into columnar structures as seen in Figure 16. The voids between the individual columns are a primary cause of its low thermal conductivity.

44

Weak inter-columnar bonds aid the EB-PVD's strain tolerance during thermal expansion and contraction. While this mechanism differs from that of APS, both APS & EB-PVD behave similarly when strained thermally. EP-PVD is more durable than APS because the columnar grains are independent of each other, whereas the APS has an inherent network of parallel and perpendicular cracks due to interlocking splat boundaries. During erosion testing, it has been found that an EB-PVD is 10 times more resistant than APS at direct FOD impact, and twice as resistant under glancing impacts, while at smaller angles, EB-PVD was twice as resistant. Therefore EB-PVD is typically used on parts, like blades, that are dynamic within the turbine engine.

2.8 Degradation of TBCs

2.8.1 Degradation without FOD Influence

TBCs can degrade due to causes other than FOD.   Stresses from thermally-induced loading is one commonly seen mechanism. During use, components in a typical aircraft gas turbine engine may experience temperatures that range from -30 ºC to 1650 ºC. TBCs are therefore degraded by thermal exposure of high temperatures. Also, they experience thermal cycling which is caused by large changes in temperature. Commonly-seen degradation mechanisms include: spinel formation, TGO growth, residual stress release, imperfections, and interface undulations or waviness. Many of these work in cooperation with each other to further degrade the TBC.   The formation of spinel increases the brittleness in the BC/TGO interface once aluminum has been depleted and other oxides begin to form. TGO growth occurs during every hot cycle when the BC oxidizes. As the TGO grows in a constrained volume, compressive stresses

increase between the BC/TGO/top coat interfaces [19, 20]. As the parts cool, residual stresses within the BC/TGO/top coat interfaces cause imperfections, undulation crests and troughs, and separation [19, 20, 21]. To try and relieve residual stresses within the layers, cracks begin to nucleate throughout the interfaces. Further thermal cycles and thermal expansion mismatch causes cracks or imperfections to propagate and coalesce until large-scale buckling or edge delamination occurs. The TBC will finally fail by spallation as the critical stress intensity factor is reached.

2.8.2 Degradation of TBCs with Environmental Influence

When foreign species like sand, volcanic ash, or other FOD are introduced into an engine they can deteriorate the TBC. The resulting damage will lead to premature failure of the TBC by spallation or delamination, but the functions for failure are slightly different. Damage is dependent on size, velocity, hardness, density, inertia, and intensity of energy and angle of attack. Large FOD, ~1000 μm, can create a point impact that compresses the material removing voids, increasing density and decreasing thickness. As the physical properties of the TBC change so does its insulative properties. The densification and decreased thickness causes the area to become a hot spot where sintering of the TBC will eventually occur. Upon sintering and the rise in temperature, the rate of BC oxidation will grow along with the TGO layer creating defects and undulations which will lead to spallation in that area.

Erosion of particles 100μm or less can cause similar effects if concentrated on a single area or if impacting directly at 90 ° angle to the surface. In the instance an APS

coating is attacked, additional cracks are introduced further weakening the interlocking strength of the splats causing premature spallation. For an EB-PVD coating only the individual columns affected maybe severed because the column is weakly bonded therefore not affect by neighboring damage. An APS coating is affected more by erosion that EB-PVD, due to their weakly bonded splat boundaries and their networks of cracks, resulting in an unpredictable cascading separation of the coating [19]. For an EB-PVD coating, the tips of the columns may be fractured but much larger amounts of energy are needed to shear the columns beneath the surface of the tips. Once tips are damaged the area can potentially sinter causing neighboring columns to fuse which then increases the area of spallation. Therefore while mechanisms of spallation are different, end results of erosion are similar in both coatings.

Smaller foreign debris like dust, sand, and ash effects TBCs in ways other than erosion when entering high temperature turbine engine environments. Once ingested debris absorbs enough thermal energy to transition from solid to molten liquid glass at approximately 1150 °C. Molten sand/ash contacts the TBC and infiltrates the ceramic microstructure by diffusion and wetting between the grains of the TBC. Upon cooling the affected area experiences thermal expansion mismatch which causes TBC to delaminate and spall. Also, as the molten glass – normally containing Si, Ca, Al, and sometimes Mg in composition – wets the YSZ TBC a chemical attack occurs [25].   This chemical attack depletes Y from the coating and redeposit ZrO in the monoclinic phase. The attack of the molten glass was found in helicopter turbine engines operating during the Persian Gulf War in 1990's [1] . An example of a CMAS coated blade can be seen in

Figure 17. This molten glass attack is referred to as CMAS (calcium-magnesium-alumina-silicate) attack on TBCs.
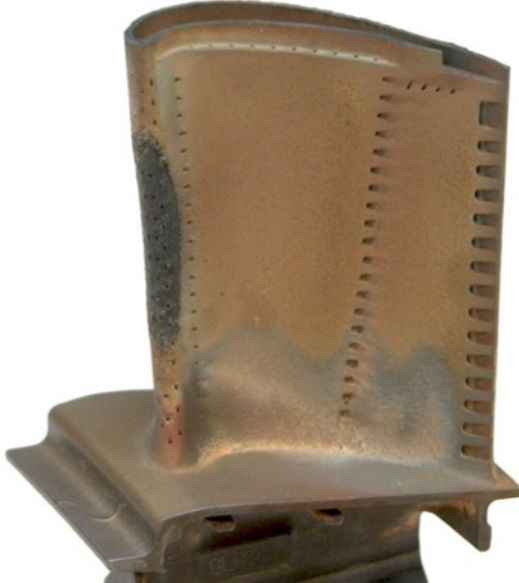
Figure 17: Turbine engine blade coated with CMAS

2.9 CMAS interaction with TBCs

The term CMAS refers to the molten glass that forms from the heating of sand in a turbine engines. CMAS has been collected from cooled turbine section parts and analyzed for composition. The composition of the CMAS was determined to be mostly calcium-magnesium-alumina-silicate. The average composition of the CMAS was found to be 33% CaO, 9% MgO, 13%AlO and 45% SiO [3]. Since its discovery, extensive research has been conducted to understand its effects and failure modes on TBC coatings. The field of research consists of studies on CMAS interaction on field service parts and also lab experimentation of Sim-CMAS on TBC coatings. Most of the studies do not use

actual sand but instead use a similar composition of oxides as described in section 1

where homogeneity and repeatability can be achieved throughout each test.

Research has found that the chemical attack of CMAS on TBC coatings affect

multiple layers of the coating [1, 2, 3, 6, 20, 21, 23, 25, 26, 27]. In the top coat, the Ca

and Si in the molten glass leads to preferential dissolution of Y from YSZ [3, 28]. As

discussed earlier, YSZ in TBCs is normally 7% wt. yttria for phase stability but when in

contact with CMAS Zr is dissolved and then precipitates as segregated globular particles

[25, 26]. This process reduces the phase-stabilization of Zr, enabling a transformation to

monoclinic structure upon cooling thereby degrading the strain tolerance of TBC [3, 28,

27]. As the molten glass penetrates close to the TGO layer the CMAS also dissolves Al

from the TGO layer [3]. As alumina is depleted from the TGO layer, metal oxide

formation is accelerated and species such as $(Ni,Co)Al_2O_4$ and NiO create a weak, brittle

TGO layer. Wellman et al. [27], showed that the CMAS-infiltrated areas in EB-PVD

coatings are more susceptible to spallation when subjected to erosion than an unaffected

TBC coating.

The physical effects of CMAS infiltration have also been studied by previous

researchers. CMAS has proven to physically infiltrate TBC coatings rapidly upon

contact with the top coat filling any cracks, pores, or voids [3]. Mercer et al. [29]

characterized delamination of TBCs caused by "cold shock" as the turbine engine cooled

during shutdown. The cold shock which occurs when the TBC is exposed to a large, rapid

decrease in temperature causing a temperature gradient normal to the surface of the top

coat. In effect, the sudden decrease in temperature creates cracks, normal and/or parallel

to the surface of the top coat. Crack properties are influenced by the heat transfer coefficient of the TBC system and the thermal conductivity and thermal diffusivity of the top coat material [29]. As the CMAS infiltrates EB-BVD structure, it increases the volume of the infiltrating area. Upon cooling the thermal expansion mismatch in the affected area create to bending stresses in the columns at the edge of the infiltrated area [30]. The bending stresses can cause crack initiation within a column which can coalesce through multiple columns. The coalescence of the columns creates delamination cracks [30]. Additionally it's been reported that CMAS infiltration decreases the durability of EB-PVD to erosion [27]. Wu et al. [28] found that in APS coatings the porosity was reduced to 5% when infiltrated with CMAS. He also discovered the thermal diffusivity of APS increased by 70% and micro hardness increased by 25% [28]. Kramer et al. [31] discovered that upon cooling tensile stresses arise at the surface of the CMAS infiltrated areas in an APS coating. These stresses produced channel cracks that extend through the layer of CMAS penetration. Ultimately CMAS attack has proven to delaminate or spall the TBC at a much higher rate than the expected life cycle.

2.10 TBC resistance to CMAS

Further research has and is being conducted on TBC coating to improve their durability, thermal conductivity, and resistance to CMAS infiltration. Rai et al. [32] studied the effects of CMAS infiltration on EB-PVD buttons coated with a layer of impermeable, sacrificial, and non-wetting coatings such as: SiO_2, Palladium (Pd), and others, as well as surface layer densification techniques such as electron beam (EB)

glazing.   The results revealed the impermeable, sacrificial, and non-wetting coatings did not stop CMAS infiltration while a dense EB glazed Pd top coat did. He concluded that CMAS infiltration is more dependent on density and structure of top coat than the chemical make-up.

Other improvements by compositional change of the ceramic top coat have been proposed. Aygun et al. [33] studied the addition of 20 mol. % Al_2O_3, and 5 mol. % TiO solid solution into the YSZ ceramic coating using SPPS deposition. He found that additional Al drives the CMAS composition to an easy-to-crystallize material while the additional Ti promotes the nucleation of material to crystalize, or glass. Ca and Si from the CMAS were completely arrested in the upper portion of the top coat in the form of $CaAl_2Si_2O_8$ (anorthite). As the need for higher efficiency in turbine engines rises and the use in desert like conditions continues new methods of CMAS resistance and arrest will likely be the subject of continual study.

III. Methodology

3.1 Introduction

This section discusses the materials and methods used in the present study. Sand samples, substrates, and other materials used in experimentation are described. The procedures for preparing samples, heating samples, and polishing samples are thoroughly discussed. The petrography process and purpose are explained. Methods and equipment used for optical and scanning electron microscopy (EDS) and for data analysis are also described in this section.

The overall experimentation was broken into three phases; each phase had a specific purpose and served as a platform to advance to the next phase. The goal of Phase 1 was to heat the sand samples at various temperatures in order to observe the transformation process and grow in familiarity with heating procedures. Seven (7) different sands were studied in this phase: AFM, Yu, AFRL 02, A1, A2, RAM, and VA. The purpose of Phase 2 was to validate measurements, procedures, and techniques on 25 mm x 25 mm x 3 mm samples of electro-formed nickel substrate. Eight (8) different sands were studied in this phase: VA, AFM, A1, A2, AFRL 02, Yuma, QGCS, A2, and RAM.

Phase 3 was the main focus of experimentation in the present study, building on the methods and process validation accomplished in Phase 1 and 2. In Phase 3, the consolidation and melting behavior of eight (8) different sands on two different TBCs was investigated. Sands used were: Helm, Yuma, Afg Bl, Bal Bl, AFM, AFRL 02, A1, and VA. TBCs used were supplied by two manufacturers under proprietary agreements,

and will be described as TBC A and TBC B for the purpose of maintaining an open

public distribution on the present document. More detailed explanation of Phases 1-3,

processing methods, and materials used are given in sections that follow.

3.2 Sand Samples, Composition, and Size Distribution

The composition and size distribution of sands used for experimentation are

described in the tables below. Natural sands vary in composition and particle size from

site to site and can even vary noticeably within a single region. Therefore Table 4 is an

attempt to centralize data from studies [1, 2, 10, 14, 34] mentioned in previous sections.

Composition of the natural sands (e.g. chemical makeup, particle size distribution,

mineral content) was not measured as part of the present study: rather, the sand

characteristics determined by the researcher and organizations cited above were used.

The natural sands used are referred to as Afghanistan Mixed (AFM), Helmand Basin

(Helm), and Yuma Proving Ground (Yuma). Volcanic Ash (VA) was also a sample that

was used during experimentation, but its results and analysis will not be discussed or

reported in the present document.

Two additional sand samples were collected from T700 first stage high pressure

turbine (HPT) blades provided to the Coating Technology Integration Office (CTIO), Air

Force Research Lab (AFRL), Wright-Patterson AFB, Ohio. The sand samples were

collected by scraping the sand particles from the root of the HPT blades. One set of

engine blades were from a rotary aircraft that spent the majority of its operational service

time in Afghanistan; this sample is referred to as Afghan Blade, (Afg Bl). The second set

of engine blades were taken from an aircraft that spent the majority of its operational service in Balad, Iraq; this sample is referred to as Balad Blade (Bal Bl). It is recognized that these sample have undergone cyclic heating within the engine, but it is noteworthy that the samples were taken from a relatively cold section of the blade.

Five manufactured sands were used throughout the various phases of this research. The composition and size distribution of each type of manufactured sand is shown in Table 5 and Table 6. AFRL 02 was developed by the CTIO office for use in a study on sand in the Middle Eastern desert regions and North American desert region [34]. From this study, a set of requirements were formed for mineral composition and size distribution of AFRL 02. The sand was manufactured by Powder Technology Inc. (PTI). Another manufactured sand used in the present research is QGCS, a sand that is specified by the *DoD Joint Service Specification Guide, Engines, Aircraft, Turbine* [4] for engine sand ingestion testing. The name QGCS refers to the mineral composition – Quartz, Gypsum, Calcite, and Salt. Lastly, three (3) sand samples developed by the US Army were used for the present research; these sands were developed to meet a specific distribution of particle sizes, and were not developed to match or mimic any particular composition of natural sand. These US Army-developed sands are called PTI A1 ultra-fine (A1), PTI A2 fine (A2), and PTI ARAMCO (RAM). The slight compositional variations between these three sands can be found in Table 6.

Table 4: Composition and particle size distribution of Mixed Afghanistan sand, Helmand Basin sand, and Yuma Proving Grounds sand [1, 2, 10, 14, 34].

Minerals	Mixed Afghanistan Sands	Helmand Basin
Minerals	Relative abundance	Relative abundance
Quartz (SiO_2)	Primary	Primary
Calcite ($CaCO_3$)	Primary	Primary
Plagioclase ($NaAlSi_3O_8$ – $CaAl_2Si_2O_8$)	Secondary	Secondary
Halite (NaCl)	Primary (wp)	Primary (wp)
K-Feldspar (($K,Na)AlSi_3O_8$)	Secondary	Secondary
Muscovite ($KAl_2(AlSi_3O_{10})(OH)_2$)	Trace	Trace
Dolomite ($CaMg(CO_3)_2$)	Secondary (wp)	Secondary (wp)
Gypsum ($CaSO_4 \cdot 2H_2O$)	Trace	Primary
Size Distribution		
Sands	Secondary	Secondary
Silts	Primary	Primary
Clay	secondary	Secondary
wp = when present		

Yuma Proving Ground, Arizona	
Minerals	Relative Abundance
Quartz	Primary
Calcite	Primary
Plagioclase	Secondary
K-Feldspar	Secondary
Muscovite	Trace
Kaolinite	Trace
Size Distribution	
Sands	secondary
Silts	Primary
Clay	Secondary

55

Table 5: Composition and size distribution of AFRL 02 and QGCS.

AFRL 02		QGCS	
Minerals	% by Wt	Minerals	% by Wt
Dolomite (CaMg(CO$_3$)$_2$)	13.33	Quartz (SiO$_2$)	60
Gypsum (CaSO$_4$·2H$_2$O)	28.75	Gypsum (CaSO$_4$·2H$_2$O)	26
Aplite (NaAlSi$_3$O$_8$)	16.36	Calcite (CaCO$_3$)	12
Silica (SiO$_2$)	36.56	Salt (NaCl)	2
Salt (NaCl)	5.00		
		Particle size distribution	
Particle size distribution		100% <=	1000 μm
90% <=	40.5 μm	90% <=	500 μm
50% <=	8.5 μm	70-75% <=	250 μm
10% <=	2.5 μm	50%-55% <=	120 μm
		25-30% <=	75 μm

Table 6: Composition and particle size distribution of PTI sands.

PTI	A1 Ultra Fine	A2 Fine	ARAMCO
Composition	% by Wt	% by Wt	% by Wt
SiO_2	68-76	SAME AS:	SIMILAR TO:
Al_2O_3	10-15		
Fe_2O_3	2-5	PTI A1 Ultra Fine	PTI A1 Ultra Fine
Na_2O	2-4		
CaO	2-5		EXCEPT
TiO_2	0.5-1		
K_2O	2-5		
NaCl	0		Added 10%
Particle size distribution			
<100%	20.5 μm	120 μm	SAME AS:
< 64-56%	5 μm	10 μm	PTI A1 Ultra Fine
<44-36%	4 μm	4 μm	

3.3 Substrates

The substrates used for Phase 1 experiments were LECO[®] graphite-ashing crucibles, 12.5 mm in diameter by 16 mm in height. A photo of these small crucibles can be seen in Figure 18. Crucibles were used in the as-received condition. The substrates used for Phase 2 experiments were 25 mm x 25 mm x 3 mm Electro-Formed Nickel alloy squares, shown in Figure 19.

In Phase 3, two types of TBC-coated substrate "buttons" were used, each provided by a turbine engine Original Equipment Manufacturers (OEM) (see Figure 20). The TBC button A was coated by EB-PVD with an YSZ top coat and a Pt aluminide BC on a gas turbine engine superalloy substrate. TBC button B was coated by EB-PVD with an YSZ top coat and aluminide BC on a gas turbine engine superalloy substrate. The top

coat of was deposited at a slight off-angle during the deposition process, a result not

intended by the manufacturer during application of turbine blade TBC coatings.

Figure 18: Graphite Crucible with LECO® graphite crucibles containing sand.
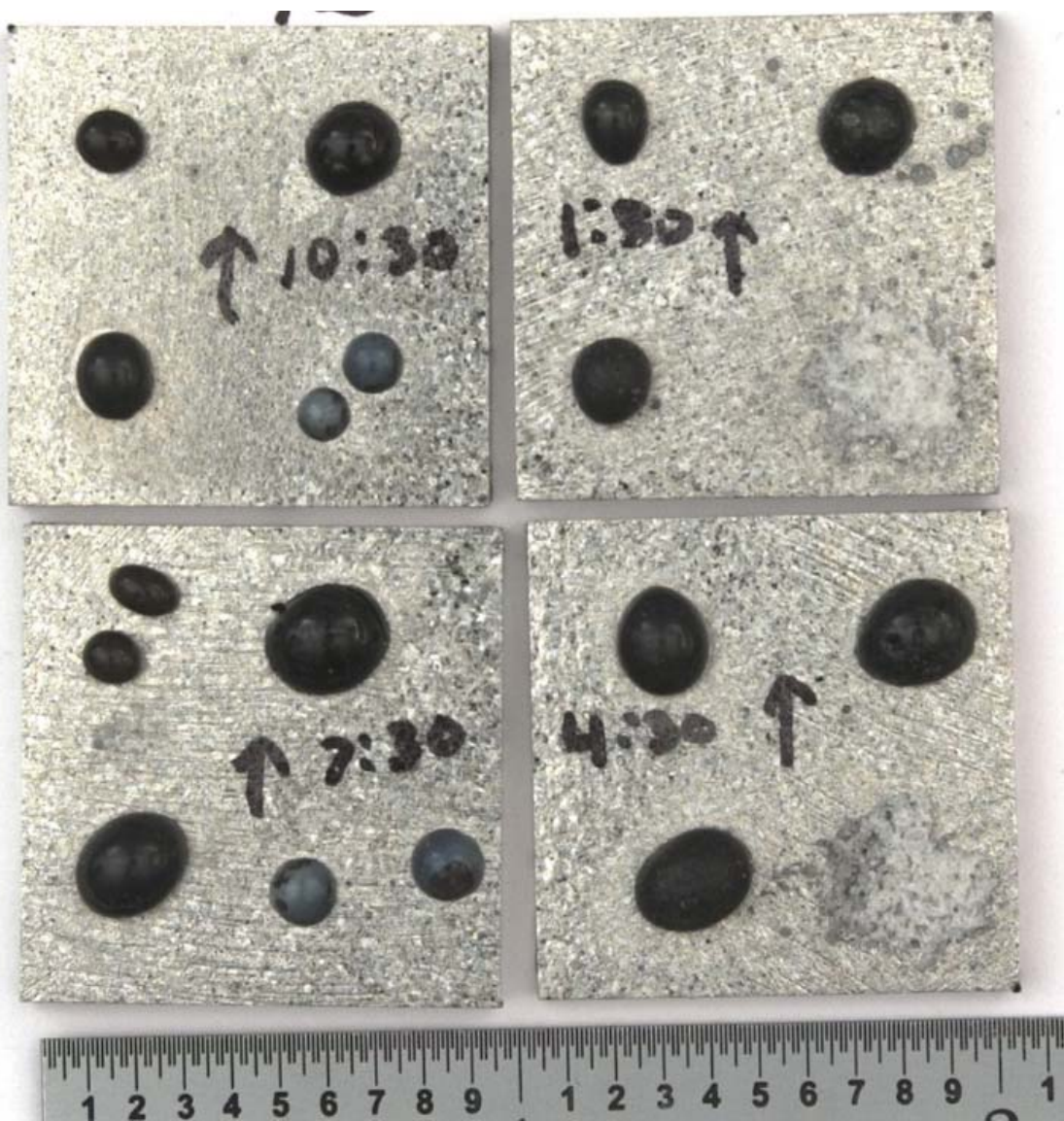
Figure 19: Electro-Plated Nickel superalloy square substrates.
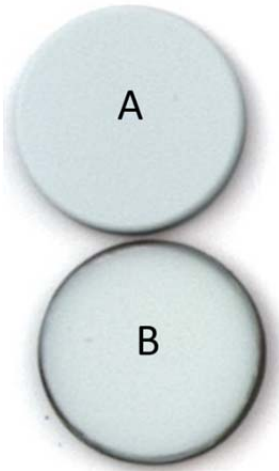
Figure 20: EB-PVD TBC substrates from company A and B.

3.4 Sample Preparation

Phase 1 sample preparation began with scribing the names of sand samples into the LECO® crucibles. Each LECO® crucible used was weighed and recorded before and after being filled with sand. Approximately 0.5 grams of sand was loaded into each LECO® crucible. Once loaded, individual LECO® crucibles were placed into a larger graphite holding pan, also seen in Figure 18. The position of each LECO® crucible was recorded before placing the large holding pan into the furnace.

Phase 2 and Phase 3 sample preparation began with pressing the sand samples into 25 mm radius disks. This was done by using a Carver Inc. hydraulic press and a Potassium Bromide (KBr) Powder press. The sand disks were compressed using pressures from 35 MPa to 70 MPa. The sand disks were made with 0.6 grams of sand per disk, resulting in a nominal disk thickness of 1.5 mm. To fit more compacted sand disks

on each substrate wafer, compacted disks were sliced into three or four smaller pieces using a razor blade. These compacted sand chips were then placed on the individual square substrates or the TBC buttons. Disk samples were not consistent in size or shape due to the variation caused during the slicing of the disks.

3.5 Heating Procedures and Materials

3.5.1 Static Furnace

The prepared samples were heated by a graphite laboratory furnace (Thermal Technology LLC). The furnace has a temperature capability of 2500 ºC within a reducing environment for static or batch heating only. The internal area available for heating specimens is four inches in diameter by six inches in height. The furnace is equipped with a water-jacketed outer shell for continuous cooling. The reducing environment is nitrogen gas supplied to the internal heating core. The furnace has a one-inch diameter viewing window. The nitrogen gas keeps the internal graphite parts from oxidizing at high temperatures. The gas also serves to de-fog the viewing window. The viewing window allows for pyrometric temperature measurement of the inner graphite walls of the furnace.

The graphite furnace is also equipped with an internal thermocouple (TC), positioned approximately three inches below the large graphite holding pan. Due to the positioning of the TC, the temperature measurement varies within a range of 200 °C, ± 10 °C from pyrometer measurements. An illustration of the furnace is provided in Figure 21.
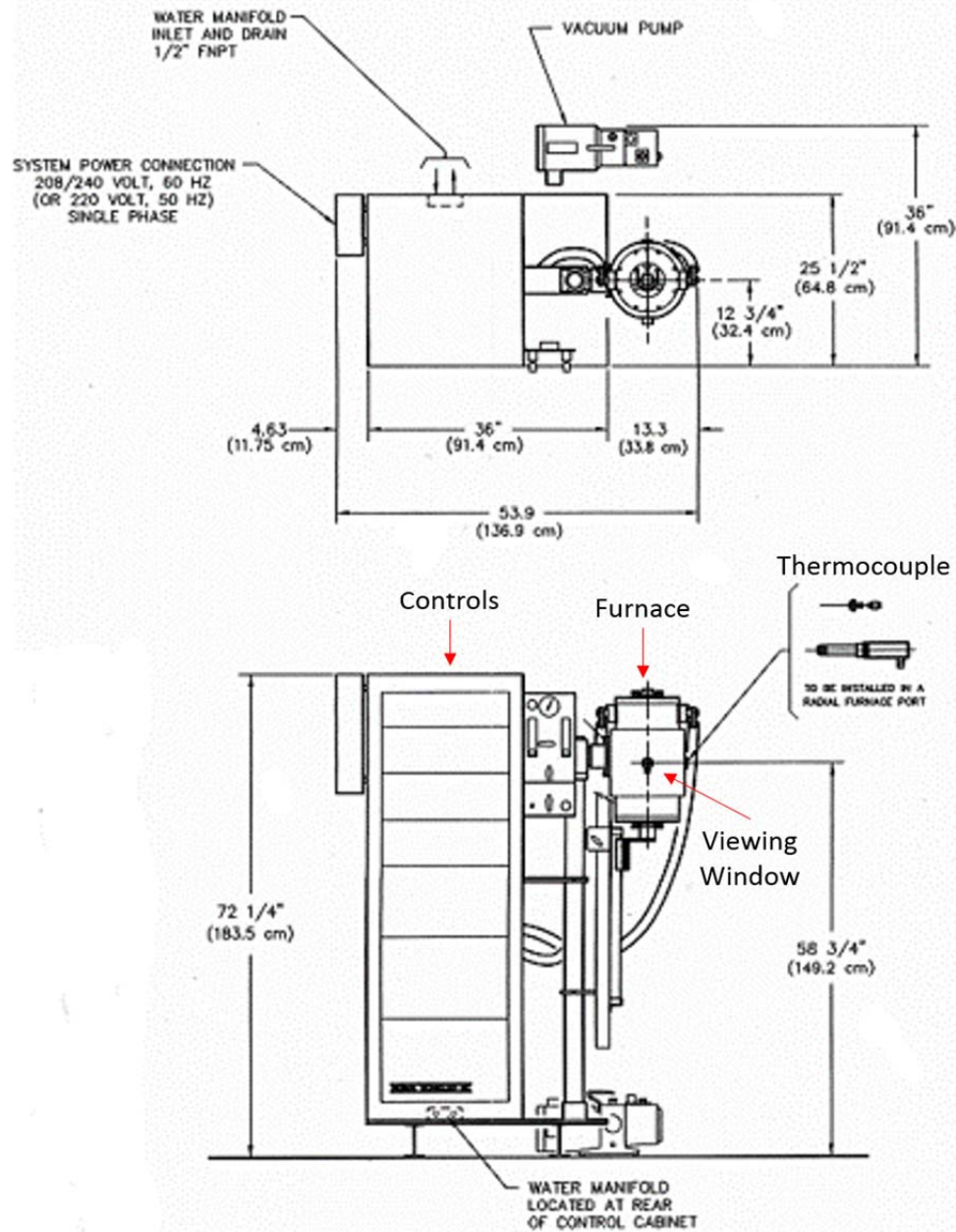
Figure 21: Static Furnace Illustration

3.5.2 Pyrometer

Temperature measurements were taken through the viewing window using a disappearing filament Micro Optical Pyrometer (Pyrometer Instrument Company, Bergenfield, NJ). In a disappearing filament, a current is passed through a tungsten wire filament, increasing its temperature and causing a specific thermal emission profile. The temperature of the filament is controlled by the manual adjustment of a calibrated potentiometer. As the temperature of the heated filament approaches that of the heated specimen, both the filament and the specimen will have a similar thermal emission profile, causing the filament to "disappear" into the background. The temperature of the filament is then read from the calibrated potentiometer.

The tungsten wire filament pyrometer has a temperature range capability of 700 °C to 3200 °C. The use of two red filters truncates the distribution of the thermal emission, allowing for improved accuracy. Using these filters, the filament seemingly "disappears and/or reappears" within a much smaller temperature range, thereby decreasing error when measuring temperature.

3.5.2 Procedure

The furnace heating procedures were consistent for Phases 1 to 3. The target temperatures were 1000 °C, 1100 °C, 1150 °C, 1200 °C, 1250 °C, 1300 °C and 1350 °C. Heating was conducted at a rate of approximately 10 ºC/minute. Once the target was reached, it was held within ±5 °C for a five-minute duration. The samples were then cooled at a rate of approximately 7 ºC/minute. The furnace heating process was

accomplished using manual adjustments of heating the current according to a protocol developed by CTIO for the furnace.

   After the samples – either LECO® crucibles, square nickel substrate, or TBC buttons – were prepared and placed into the large graphite holding pan, the pan was then loaded into the core of the furnace and secured for heating. When operating the furnace, the time, current, voltage, and TC temperature were recorded for repeatability within testing.

   Several steps were involved in the operation of the furnace. First, the furnace was turned on and current was increased from 0 A to 85 A. This allowed the internal parts to warm slowly to a TC reading of 65 °C, so as to avoid thermal shock of the graphite material. After 15 – 20 minutes, the current was increased to 130 A for an additional 15 – 20 minutes until a TC reading of 170 -185 °C was reached. After another 30-45 minutes, a third current increase was made to 200 A until a reading of 500-600 °C was reached. Finally, depending on the target temperature, the current was increased to an appropriate value between 225 A and 255 A, and the furnace was allowed to increase in temperature (approximately 40 – 60 minutes). When the furnace TC reading was within approximately 300 ºC of the target temperature, the pyrometer reading was used as the primary tool for temperature measurement.

   Once the pyrometer indicated the temperature of the inner walls of the furnaces were within 15-20 °C of the target temperature, the furnace was reduced to 10-12 A, depending on how fast or how slow the temperature was climbing according to the thermocouple. When the internal temperature was within 5 °C of the target temperature,

the heating current was reduced an additional 3-5 A. When the target temperature was reached, the current was reduced 2-4 A and fine-tuned as needed during the five minute holding time.

After the five minutes, the current was reduced to 0 A. The furnace then cooled to a TC temperature of 100 °C in approximately three hours. Care was taken to ensure that the furnace remained closed under a continuous flow of cooling water and purge gas until the graphite electrodes reached a temperature low enough to eliminate oxidation.

Once the furnace was opened, the large graphite holding pan was removed and placed on a table. In Phase 1, the crucibles cooled and were then reweighed. In Phase 3, some of the TBC buttons had to be covered with a shield due to excessive spallation during cooling.

3.6 Petrography: Processing and Technique

Petrography was conducted with Phase 1 samples only. Through grinding and polishing, the sintered glass-like pellets from the LECO® crucibles were processed into thin sections between 25-45 μm. First, the pellets were ground on a low-speed wet wheel into the midpoint of the sample. They were then hand polished on a 30 μm metal-bond diamond lapping plate, followed by a 15 μm metal-bond diamond lapping plate. Finally, the surface was polished using a 6 μm resin-bond diamond lapping plate. De-ionized water-rinsing and ultrasonic treatment was conducted between each polishing transition to ensure a clean surface with no contamination. After one side of the pellet had been

polished to a mirror surface, it was then glued to a 35 mm petrographic glass slide. The above polishing procedure was then repeated on the other side of the specimen.

The main difficulties encountered during the thin-sectioning process were "tumbling", and partially-destroyed cross sections. Tumbling occurs when minerals loosen and separate from the pellet while polishing. The loose minerals then serve as their own polishing media, thus leaving visible scratches on the surface. Destroyed cross sections occur when the two sides of the mirror-polished specimen are non-parallel, resulting in a specimen thickness that constantly increases across the surface. Non-parallel surfaces can give rise to a large section of the specimen being removed in polishing. As a result, only a portion of the sample would be analyzed, and some valuable distribution data is lost.

For specimens not damaged by these processing difficulties, the thin sections were viewed through a Meiji ML 9000 transmittance optical microscope (Meiji Techno Company LTD). Thin sections were first viewed in normal transmitted light conditions, and then photographed by a Canon T2 Single Lens Reflex (SLR) camera. Next, the polarization lens on the microscope was inserted into the light path, and the specimen was photographed. Crystalline material allows the transmission of polarized light, whereas a non-crystalline material (like glass) will not allow the transmission of polarized light.   Using published comparison charts, a visual estimation of the amount of minerals present can be made using this light-dark contrast. While this method can also be used for determining the specific type of minerals present, for the purpose of the

present research, only the amount of minerals as compared to the amount of glass present was determined.

Mineral content is quantified by selecting the most representative field of view within the sample and estimating the percentage that has remained crystalline. When evaluating the amount of minerals present and the amount of glass formed, it should be noted that this process can be somewhat subjective. However, there are comparison charts that guide the researcher to make an informed evaluation. Multiple comparison charts were used in the present research in order to reduce the amount of variability. It should also be noted that because of the size of the images, the reader may not be able to see all the minerals present. The use of high quality, bright, and focused field of view is necessary during characterization to ensure all the grains of sand that have not converted to glass are visible. Also, the sample viewing location plays a large role in the evaluation. It is important to ensure that the sample represents an accurate distribution of the present minerals of the thin section. Care was taken to avoid this potential source of error, and samples were examined at multiple locations.

3.7 Mounting & Polishing Procedure

Mounting and polishing were performed for the cross-section analysis of the Phase 3 TBC buttons, and with the help and guidance of the Structural Materials Evaluation (SME) team at AFRL, Wright Patterson AFB, Ohio.

Representative TBC buttons were epoxied in a quarter-inch of Buehler Epoxicure Resin and Hardener. Epoxicure cures in 14 hours at room temperature. After curing, the

samples were cut on a Struers Accutom 5 circular wet saw. The saw uses a water-based solution for wetting. The wheel speed was set to 3000 RPM and the feed rate was set to 0.013 m/s. Each button was cut into halves and then into quarters, bisecting each of the four sand samples. The four cross-sectioned samples from each button were placed into a Struers Pronto Press with Durofast epoxy resin. The Durofast epoxy resin is a thermosetting hot-mounting epoxy resin which contains mineral and glass fillers. The mounts were then placed in a Tegra-poly 31 polisher with a Tegra-Force 5 rotating head. The polishing sequence consisted of the following steps:

1. Polishing using a Struers MD Piano 220 wet wheel at 150 RPMs with 35 N of applied force for 30 minutes.

2. Polishing using a Struers MD Largo wheel with a Diapro Largo water based solution at 150 RPMs with 35 N of applied force for 5 minutes.

3. Polishing using a Struers MD DAC wheel with Diapro Dac water-based solution at 150 RPMs with 35 N of applied force for 5 minutes.

4. Polishing using a Stuers MD Chem wheel with an OPS colloidal silicia suspension solution at 10N for 60 seconds.

After the final polish, it was noticed that some of the samples had been affected by "pull out". This happens when the sand and TBC are removed from the cross section surface by the polishing wheels. This was determined to be caused by the pressurized mounting system weakening the initial Epoxicure layer and/or the aggressiveness of the diamond used in the polishing wheels.

The next set of TBC buttons used and prepared for cross-sectioning were initially epoxied and cut using the same process. However, for the final mount, the Epoxicure was used instead of the Pronto-Press 20. Instead of employing polishing steps 1 and 2 as stated above, a modified polishing procedure used Buehler silicon wet sand paper, progressing from 120, 320, 400, and 600 grit. Polishing steps 3 and 4 were used again, with no change. "Pull out" did not occur in these samples polished with this protocol.

3.8 Optical microscopy

The Phase 2 substrate squares and Phase 3 TBC buttons were first photographed with a Zeiss AxioCam HRc camera with a TAMRON 17-35mm 1:2.8-4 lens and a Nikon 105mm 1:2.8D lens. The software used for processing the photos was AxioVision Version 4.7.2.0 copyright 2006-2008 from Carl Ziess Imaging Solutions. Higher magnification imaging was conducted on the Phase 3 TBC buttons only. Each sample image was captured using a Zeiss Discovery V20 Extended Focus Stereo Optical Microscope with an AxioCam MRc-5 camera using the same AxioVision software.

Cross-sectioned samples were observed using an Axiovert 10 optical reflectance microscope with 25x, 50x, 100x, 200x, and 500x lens. Pictures were collected using an AxioCam MRc 5 camera and the AxioVision software. Both light field optical microscopy and dark field optical microscopy were used to observe any changes underneath the heated sand. Light field optical microscopy uses direct light normally illuminating the surface; dark field optical microscopy uses indirect lighting. The indirect lighting highlights surface features that direct light would overexpose. This

technique was a valuable predecessor to highlight areas of interest for further investigation using the Scanning Electron Microscope (SEM) and Energy Dispersive X–ray Spectroscopic (EDS).

3.9 SEM and EDS Process

SEM photomicroand EDS imaging was performed on samples in two orientations; first a few, not all, were imaged from the top view looking down on the TBC button upper surface and the other was on the cross-sectional view.   All specimens were coated with carbon to reduce the effect of charging on the surface of the TBC. Once in the SEM, the specimens oriented for top view imaging were examined for unique features, such as spherical structures and edge boundaries. An EDS analysis was then performed on these features, generating a list of elements found within the feature. The cross-section oriented specimens were scanned for wetting, infiltration, and cracks in the YSZ top coat caused by sand samples atop the top coat.   The SEM used to study these samples was a Quanta FEG 600F by FEI. The EDS used was a Genesis Spectrum Version 6.0.4, 31 Aug 09, by EDAX Inc. Assistance operating the SEM and EDS was provided by the Materials Characterization Facility (MCF) of AFRL, Wright Patterson AFB, Ohio. Subsequent samples were carbon-coated and examined using a JEOL Technics Ltd SEM (control user interface version 6.56, copyright 2002, 2004). The EDS used was an EDAX Inc, Genesis Spectrum version 6.38, dated 18 December 2012.

IV. Analysis and Results

4.1 Introduction

This chapter will discuss the results produced from the three phases of testing, comparing the natural sand behavior to the manufactured sand behavior. The first set of data presented will address the sintering and melting transformation of sand samples, as well as their mass loss during heating. Next, the wetting behavior of molten sand on TBC substrates at various temperatures is compared, focusing on the differences between natural and manufactured sand. Evidence of TBC infiltration by molten sand – and subsequent TBC microstructure change – is presented. Lastly, evidence of delamination cracking is presented and discussed, validating the current methodology with the reported effects of molten sand on in-service EB-PVD coated turbine engine blades.

4.2 Sintering and Melting Results

The evolution of the sand in Phase 1, Phase 2, and Phase 3 testing can be seen in Figure 22, Figure 23, and Figure 24. A noticeable characteristic presented by the evolution of the samples is consolidation via sintering. Sintering occurs initially when relatively low temperatures form structural bridges that connect the individual sand particles. As sintering progresses, as explained in Chapter 2, particle centers approach, leading to consolidation and shrinkage. The fact that this process occurs rapidly at processing times on the order of minutes indicates the presence of a liquid. In the 1000 ℃ samples in Figure 22, liquid phase sintering is indicated by the sample pulling itself into a quasi-spherical mass. Though 1000 °C is well below the melting temperature

of sand minerals such as quartz and feldspar as discussed in Chapter 2, the presence of multiple oxides and melting fluxes in the sand has led to liquid formation. At 1150 ºC, all the sand particles heated within the LECO® crucible have sintered together into a single mass that assumes the general shape of the interior of the LECO® crucible. What cannot necessarily be easily observed in the photos in Figure 22 is that the outer diameter of the samples was slightly smaller than the inner diameter of the LECO® crucible, and that this shrinkage effect increased with processing temperature. AFRL 02 and Yuma, processed at 1150 ºC, were approximately 1 mm smaller than the inner diameter of the LECO® crucible. PTI A1 sand processed at 1150 ºC was approximately 3 mm smaller than the inner diameter of a LECO® crucible. At 1200 ºC, the inner diameters of AFM and A1 were 4.5 mm smaller than the crucible, AFRL 02 was 4 mm smaller than the crucible, and Yuma was 1.5 mm smaller than the crucible. As the temperature is increased to 1350 ºC, the samples consistently sintered and off-gassed to a state of reduced surface energy, resulting in the formation of spherical pellets.

Also due to the onset of liquid phase sintering, the surface of the spherical pellets display a shiny surface at 1300 ºC and 1350 ºC. This manifestation of a smooth shiny surface, along with the knowledge that the material is mostly silica, indicates melting is taking place. The mineral particles have embedded within a glassy matrix, and any remaining solid sand particles have been consolidated [16]. Sand samples from Phase 2 and Phase 3 studies also presented a shiny surface when processed at high temperatures as shown in Figure 23 and Figure 24. Figure 22 indicates that this transition from a dull rough surface to a shiny surface occurred between 1200 ºC and 1300 ºC for all specimens

72

in the present study. Figure 24 shows evidence this transformation occurs by 1250 ℃. Other evidence of liquid phase sintering can be seen in the bridging visible in A1 heated to 1200 °C, (Figure 23), and the droplet-like appearance of consolidated Yuma and AFM (Figure 23), and also Helm, A1, and Yuma (Figure 24), all processed at 1200 °C.

When comparing Nat-sands to Mfg-sands in the Phase 1 crucible heating studies, AFRL 02 appears to initially form a large, relatively low-density mass at 1150 ℃. At this same temperature, the natural sands formed high-density masses that were smaller. However, after heating AFRL 02 to 1350 ℃, the melted pellet was smaller than others, but similar in size to AFM. Whereas A1 is the smallest sample at 1150 °C, it is most comparable to the largest sample Yuma at 1350 °C. The difference between A1 and AFRL 02 is that the A1 out-gassed and densified most between 1100-1150 °C, whereas AFRL 02 out-gassed and densified most between 1150-1350 °C. At 1200 ℃, AFM showed evidence of a higher degree of liquid formation when compared with the other three sands. This behavior can be explained by AFM's potentially greater content of fluxing agents and fine clays, absent from the Mfg-sands as described in Chapter 3.

In Phase 2 experiments, QGCS behaved visibly different from other sand samples. In the first heating test of Phase 2, QGCS was placed in a loose sand pile on the square nickel substrate. The other sand samples were compressed into a dense chip, but QGCS was too coarse. After heating it to 1300℃ as seen in Figure 23, it was evident that the thermal behavior of QGCS was quite different than the others samples; in fact, QGCS appears not to have melted like the others. For the rest of the Phase 2 testing, QGCS was mixed with water and placed on the nickel as a dough-like lump (see Figure 23,

unheated). While a small degree of sintering and consolidation may have occurred

between 1150-1350 ºC, extensive melting at 1350 °C did not occur as it did with the

other sands. All samples of QGCS that were mixed with water and deposited on the

substrate were found upon cooling to have a hard outer surface "crust" that formed while

heating. When the outer surface was fractured, the material was coarse and granular

inside. This behavior is likely attributed to two causes: QGCS contains no Mg or Al, and

is composed of quartz (SiO_2) and minerals that decompose from a solid into a gas,

bypassing the liquid phase. A lack of fluxes or liquid-forming precursors would predict

poor sintering behavior. Additionally, QGCS has a larger grain size – over 50 % of

QGCS grains are larger than 120 μm. AFRL 02, in comparison, has a grain size less than

40 μm. Larger grains have a higher thermal inertia, longer diffusion paths, and lower

surface-to-volume ratio, greatly slowing melting and consolidation. It would be expected

that increasing the QGCS hold time would reduce these size effects, but this was beyond

the scope of the present study. Overall, QGCS did not melt like the other sands, therefore

eliminating it from further consideration in this study. All other comparisons of surface,

finish, size reduction, and loss of volume between Nat-sand and Mfg-sand in Phase 2 are

similar to those previously stated in the Phase 1 comparison.

In Phase 3 testing of sand atop TBC substrates, the comparison of Nat-sands and

Mfg-sands was expanded with the addition of Helmand Province sand (Helm),

Afghanistan blade sand (Afg Bl), and Balad blade sand (Bal Bl). In this portion of the

present research, many of the same sintering and surface area reduction changes occurred

as in Phase 1 and Phase 2 results described above. In Phase 3 testing, molten sand

samples appeared to better wet the TBC substrate surface than it wet the nickel surface in Phase 2. In Phase 2 tests, molten sands established minimal surface contact with the substrate and instead formed droplet-like spherical pellets. On the TBC surface, however, these same molten sands spread out and flowed across the surface. The behavior occurred because of the affinity of the TBC toward the melted material. Surface wetting behavior was less evident between the TBC and the Yuma and A1 samples. This behavior may be due to the lack of Mg within the Yuma and A1 samples, but a more detailed analysis is needed for greater understanding.

One other notable difference was the presence of spherical features within the melt of these samples. This occurred at 1250 ºC and 1300 ºC in the Helm, Afg Bl, Bal Bl, and AFM samples. A magnified view of spherical structures can be viewed in Figure 25. To help identify these features, Smialeck et al. [1], has described the presence of gas bubbles while analyzing the ingested deposits on turbine blade airfoils; therefore the spherical structures in the present study may indeed be due to gas formation in the molten sand. Another possible cause would be the formation of spherical solid precipitates upon cooling.

Evidence of gas bubble formation in Helmand sand came from SEM and EDS analysis is shown in the photo (b) of Figure 25. When the surface of the bubble (Figure 26) was analyzed via EDS, the scan resulted in very low count rates, leading to the conclusion that the features were empty. The walls of these empty pockets were lined with Fe-rich particles as shown in Figure 26. Unlike the previous Helm sample, when the other spherical structures from Figure 25 (e.g. those in photo (a), Bal Bl 1250 ºC) were

75

analyzed with EDS, the count rate did not fall off and an elemental analysis was able to be conducted. The SEM photomicrographs of these samples can be viewed in Figure 27. An EDS line scan of Precipitate #1 can be viewed in Figure 28 and shows a variety of elements. Precipitate #2 is mainly composed of Fe and still contains the additional elements seen in Precipitate #1. Spherical features comprised of Fe were also found in many Nat-sand samples: an AFM sample at 1250 ºC, a Yuma sample at 1200 ºC, two Bal Bl samples at 1200 ºC and 1300 ºC, and a Helm sample at 1300 ºC. In contrast, no Fe-rich phases were found in Mfg-sand samples. These results indicate the need for further study of trace elements – including Fe – in Mfg-sand and Nat-sand in order to better replicate Nat-sand.

One last feature that is obvious when comparing the evolution of the sand samples is the change in shade of the sands as they are heated. Initially in the "Unheated" state the sands have a distinct brown or white color, but during heating these colors turn to gray and eventually to black. The color differences in the unheated state are different because of the amount of impurities and mineral composition. The change in shade during heating often occurs due to various reasons such as: natural metal oxides present within the composition, the substrate used, the use of a reducing or oxidizing environment. etc. This study did not control such parameters, therefore color changes that occurred as temperature increased and as substrates were changed are not considered in this study.

In summary, the three testing phases produced similar results with respect to the high temperature transformation of particulate sand into a consolidated mass, with the

exception of QGCS. The samples showed some differences in chemical, volume, and surface energy changes during those transformations. Yuma and A1 did not wet like from Afghanistan samples and AFRL 02 samples when heated on a TBC substrate. Many spherical features were formed within the Nat-sand samples heated on the TBC surface; though some of these spheres were identified as gas bubbles, the majority were determined to be Fe-rich phases. The spherical features were not present in the Mfg-sands. The formation of these bubbles and spherical features provided further evidence of melt on top of the TBC surface.

Figure 22: Evolution of Phase 1 testing with AFM, Yuma, AFRL 02 and PTI A1 sand starting from the original unheated state to a 1350 ºC state. 1000 ºC

and 1100 ºC are presented on a similar viewing scale whereas the 1150 ºC to 1350 ºC samples are presented in a similar viewing scale. (Note: Each individual image represents a separate test sample; all samples heated to 1000 ºC for example are different samples than those heated to other temperatures such 1100 ºC or 1300 ºC)
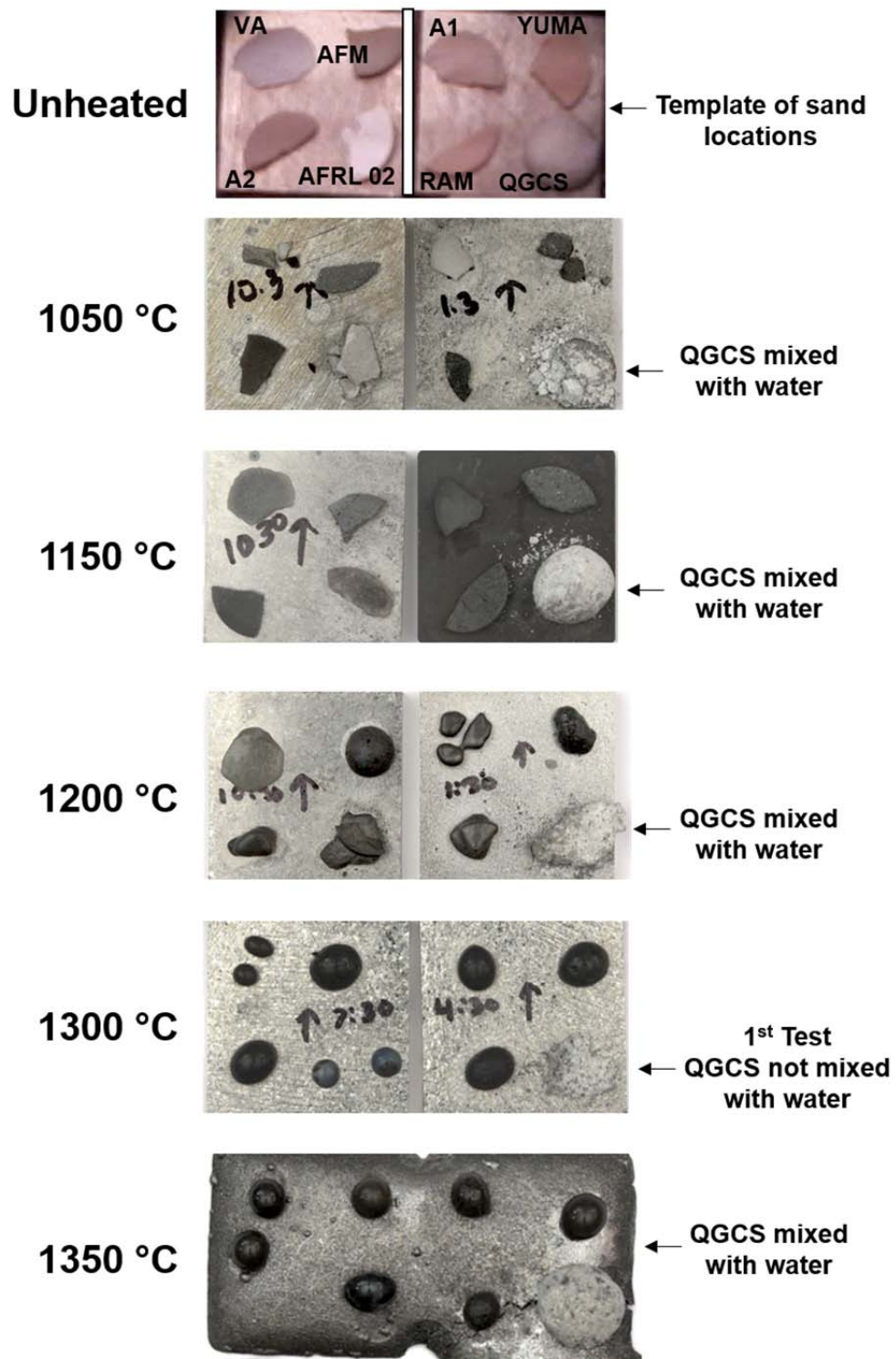
**Figure 23: Evolution of sand on electro-formed nickel squares.**
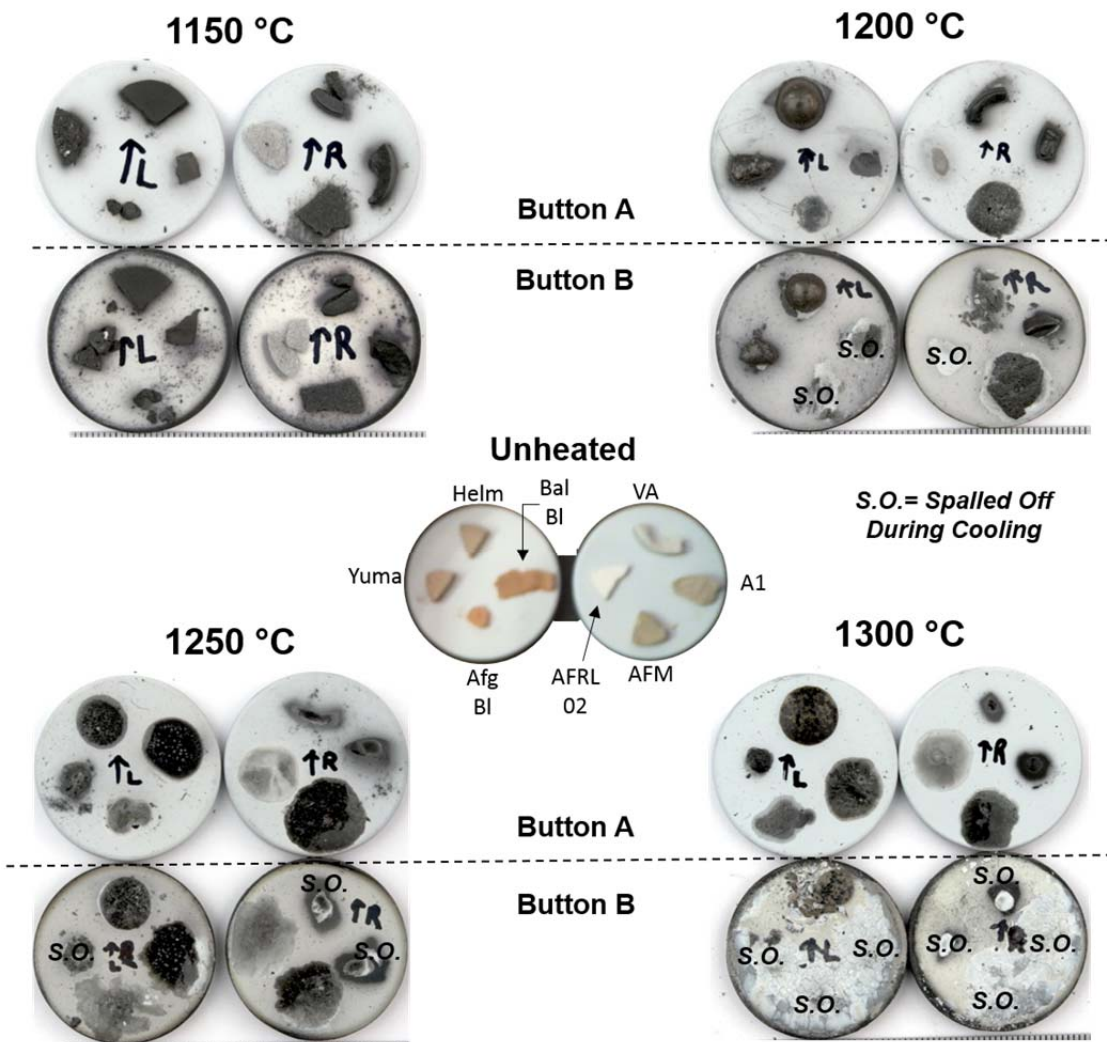
Figure 24: Evolution of sand on TBC buttons. Buttons above the dashed line are OEM buttons A and below the dashed line are OEM buttons B. Template of sands on the buttons is located in the middle of the figure. S.O. refers to places where the sand has been detached due to thermal expansion mismatch during cooling.

Bal Bl 1250 °C

Helm 1250 °C

Helm 1300 °C
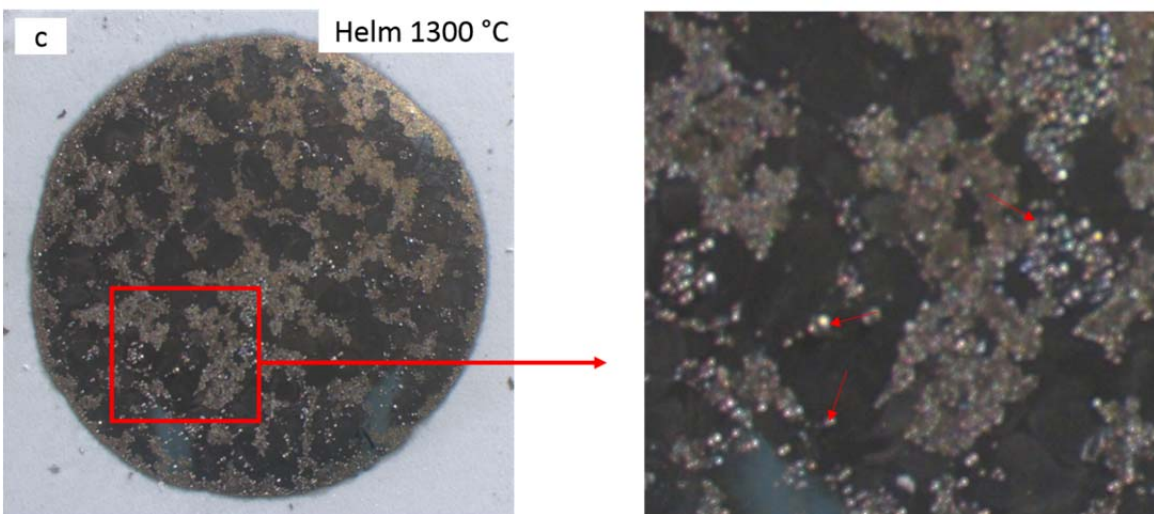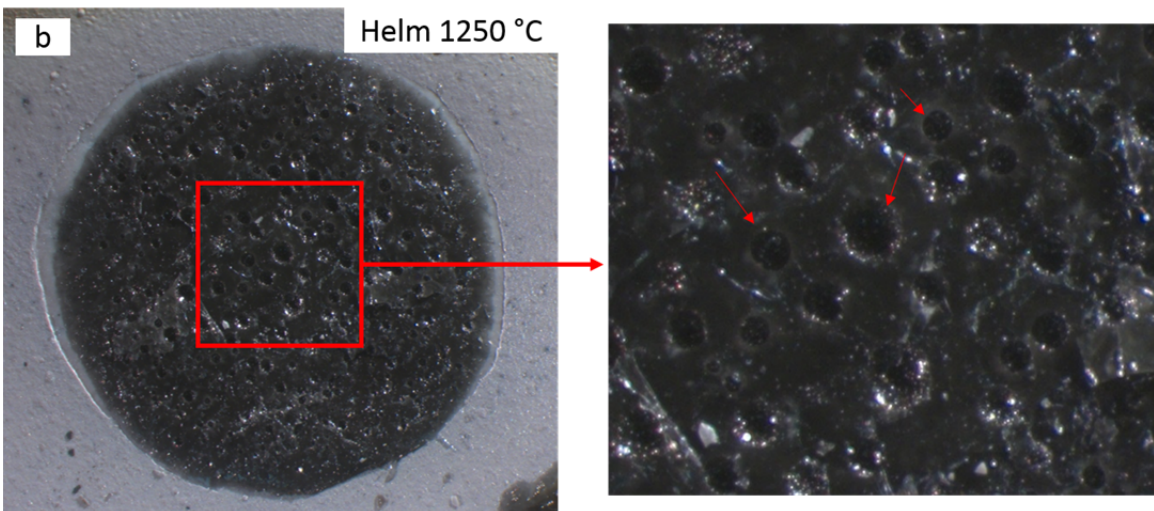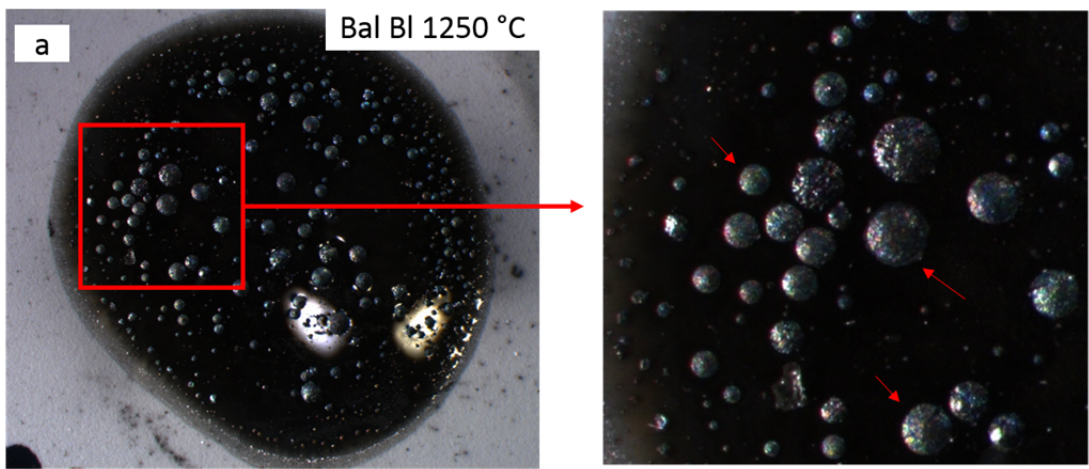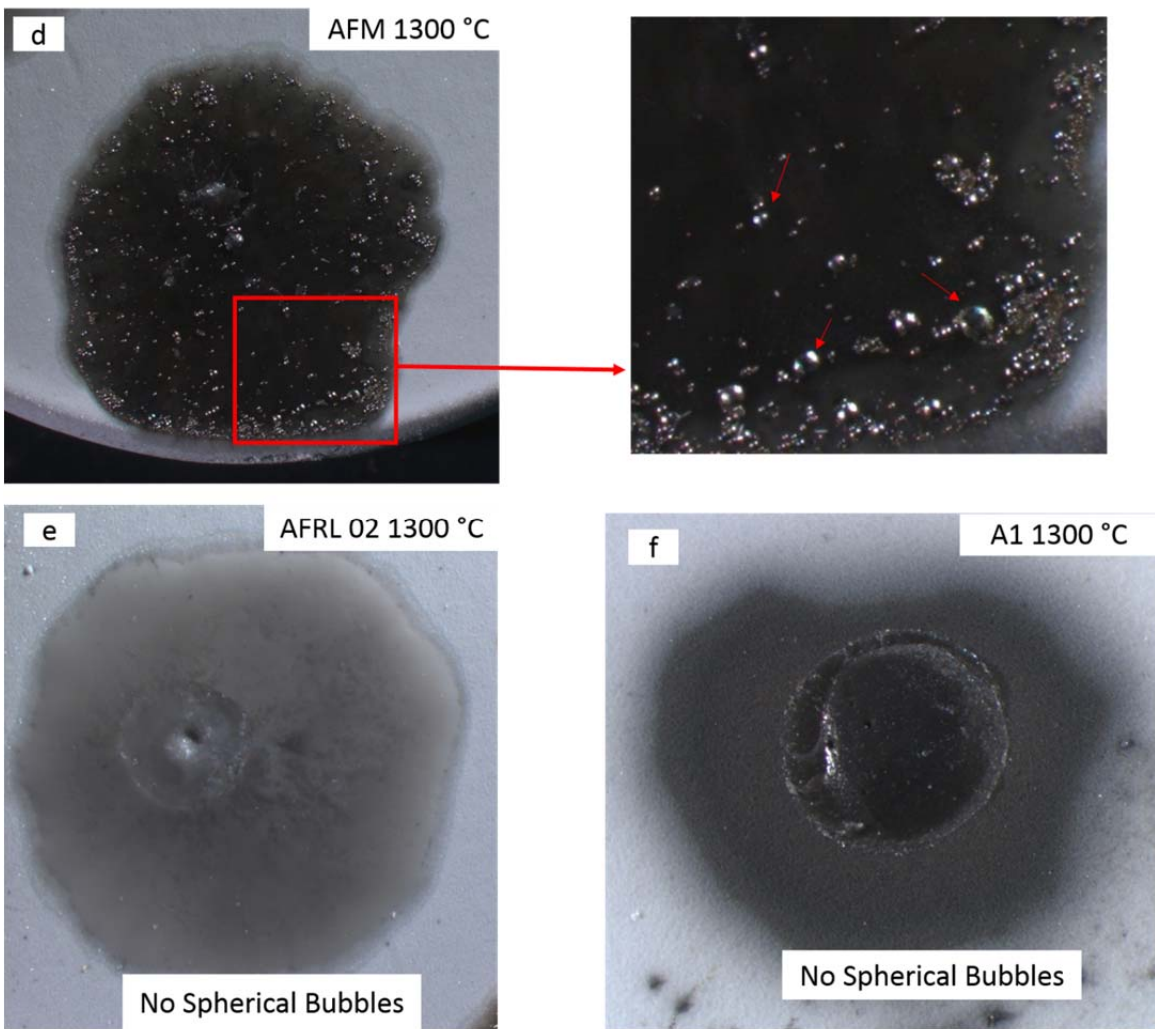
Figure 25: Optical microscopy of spherical features within Nat-sand and not within Mfg-sand samples. a) Bal Bl sample at 1250 ºC, b) Helm sample at 1250 ºC, c) Helm sample at 1300 ºC, d) AFM sample at 1300 ºC, e) AFRL 02 at 1300 ºC, f) A1 at 1300 ºC.
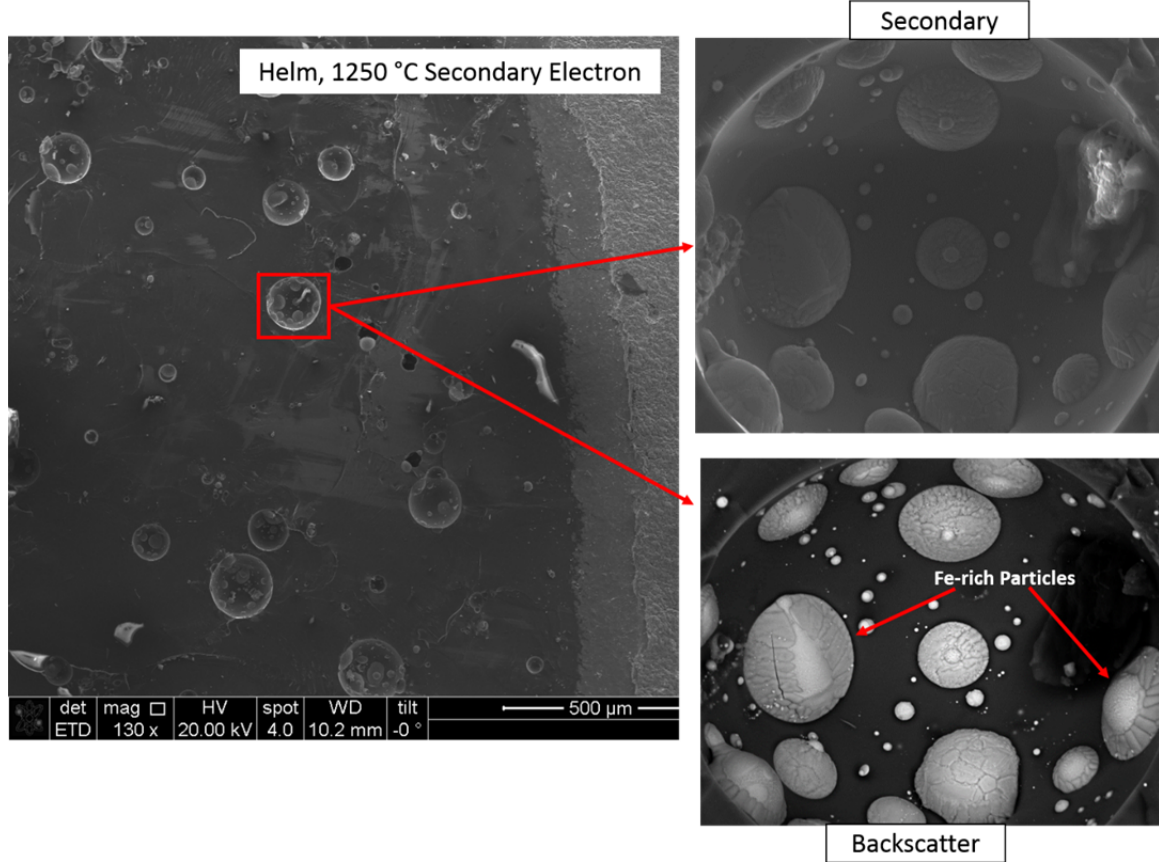
Figure 26: SEM photomicrographs of pockets in Helm sand at 1250 ºC. Pockets are lined with Fe-rich particles.
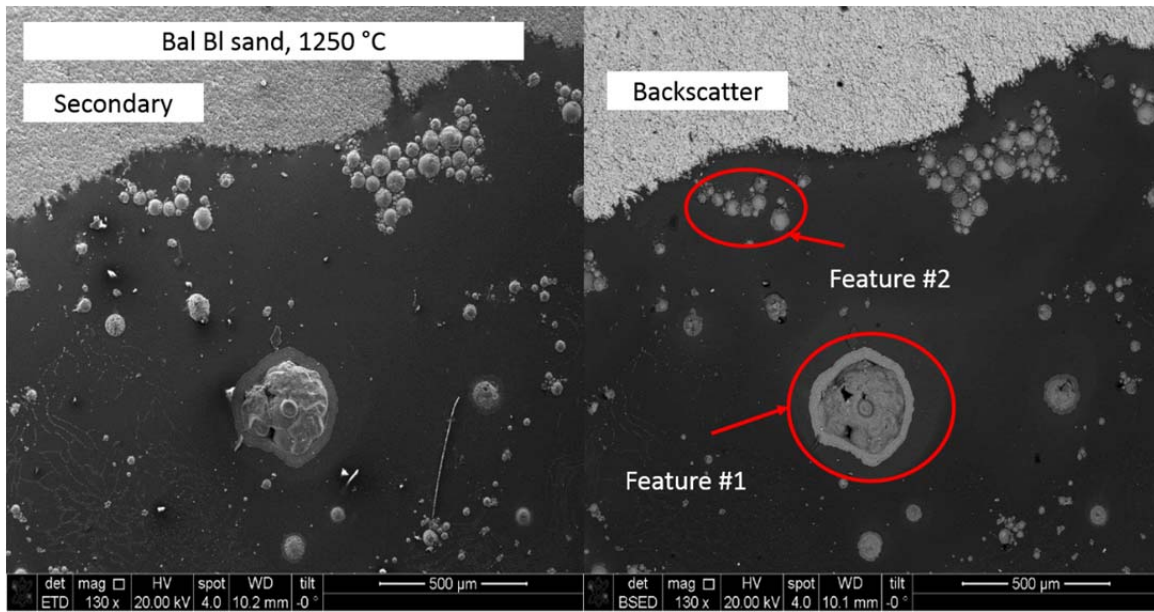
Figure 27: SEM photomicrograph of spherical features in Bal Bl sand sample heated to 1250 ºC shown in secondary and backscatter view. Feature #1 contains Cr, Fe, and S. Feature #2 is mostly made of Fe.
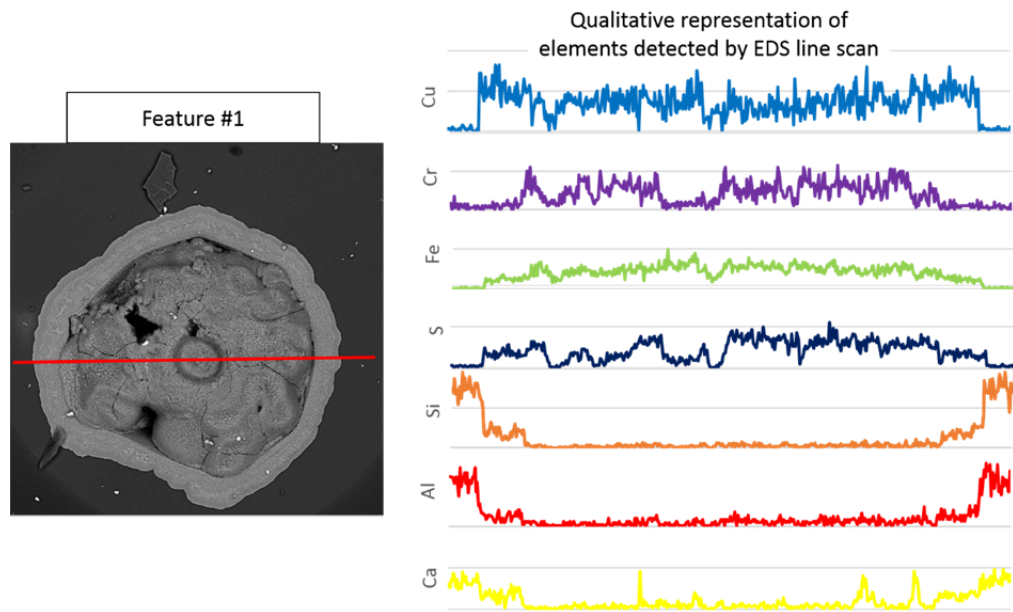
**Figure 28: SEM photomicrograph indicating EDS line scan location of Feature #1 from Bal Bl at 1250 ºC.**

4.3 Petrography Results

Petrography was used to characterize the proportion of glass and crystalline compounds present in heated sands. This data provides additional information regarding the extent of melting in the various sands. The results of the petrographic analysis of thin specimens are seen by the percentage values within each set of photos in Figure 29. The results in Figure 29 showed that the two Nat-sands studied – Yuma and AFM – differ in glass present by approximately 30 % when processed at 1200 °C, with Yuma forming glassier phase. Yuma also has the largest grain sizes present within the samples at this temperature, where AFM had relatively few large grains. The Mfg-sands showed noticeably smaller grains than the Nat-sands. The Mfg-sands processed at 1200 °C also differed by 30 %, with only 15 % of AFRL 02 transforming to glass. At 1300 ºC, the increased temperature led to a higher content of glass in all the samples. AFM contains the greatest amount of glass at 1300 ºC, whereas Yuma has the least amount of glass. AFRL 02 and A1 are both very close to one another in percentage of glass formed.

 Petrography also highlighted a difference in the mineral dispersion present in the samples heated to 1300 °C. The Yuma and A1 sands remain dispersed, with single small isolated mineral grains distributed throughout the glass matrix. In the AFM sample, unmelted mineral content manifested as a large cluster near the top of the sample. AFRL 02 also shows the presence of ribbons of unmelted crystalline material. This mineral concentration occurs near the sample's surface, just as in the AFM sample.

Petrography results show that the amount of glass within AFRL 02 at 1200 ℃ is less than the other sands, whereas at 1300 ℃, it has the second highest amount of glass. Therefore, the rate of crystalline-to-glass transformation in AFRL 02 from 1200 ℃ to 1300 ℃ was higher than any in other sand. This observation is also supported by the transition observed visually in Phase 1 testing in Figure 22. The second highest rate of crystalline-to-glass transformation was found in AFM. Even though Yuma had the most glass present at 1200 ℃, the rate of crystalline-to-glass transformation was the least of the samples at 1300 ℃.

In summary, these results reveal that even though the Phase 1 studies pointed toward the formation of dense glassy pellets fully melted, petrography reveals the continued presence of undigested minerals. The temperature needed to form glass, as well as the difference in glass formation among different sands at the same processing temperatures, highlights that "different sands melt differently", influenced by chemical and mineral composition, grain size, and amount of thermal energy.
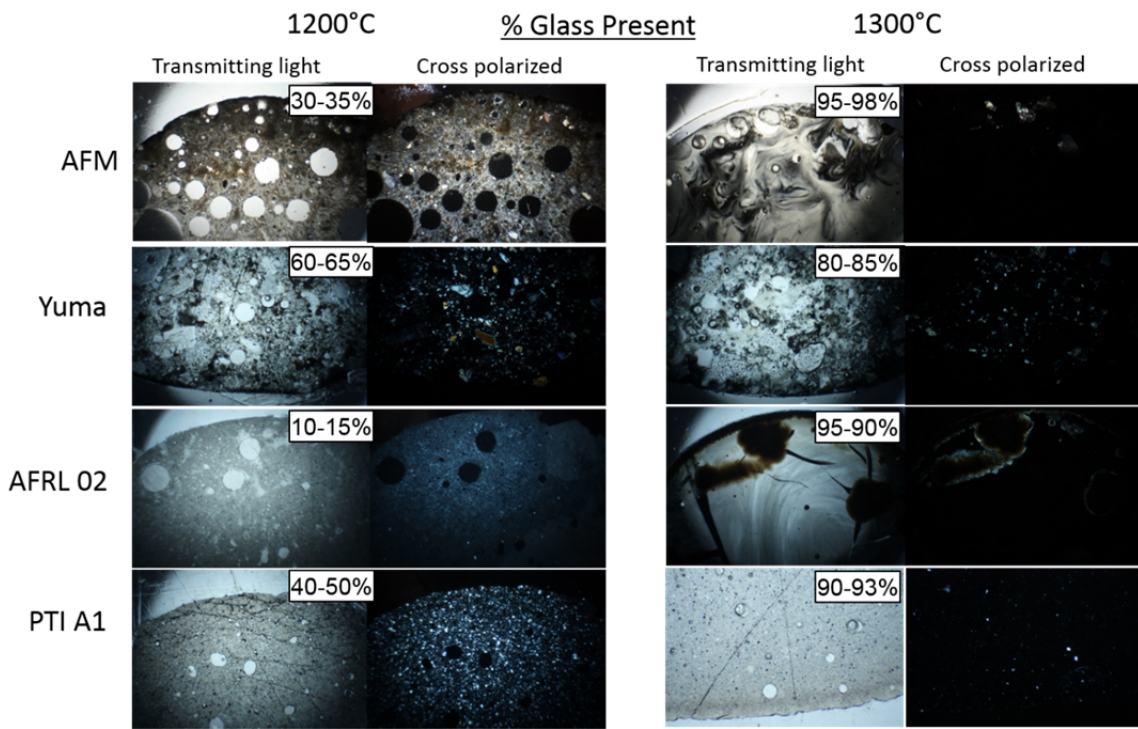
Figure 29: Petrography characterization of percentage of glass present in AFM, Yuma, AFRL 02, and PTI A1 samples heated to 1200 ºC and 1300 ºC.

4.4 Mass Loss Results

The difference in mass loss of the sand samples before and after heating determines the amount of material lost to out-gassing. The constituents of out-gassing include any compounds that evaporate within the given temperature range of these experiments, and may include: water (H_2O), sulfate (SO_2), carbonate (CO_2), sodium chloride (NaCl), hjydrogen sulfide (H_2S), and others. These compounds, present in the sand mixture, along with other oxides, can act as the fluxing agents within a sand. Therefore, by tracking the amount of mass loss through heating, information is revealed about the relative amount of flux compounds present in the sample. Simply stated, all

things being equal, a larger mass loss indicates a larger content of flux in the sand sample.

Mass loss due to decomposition of flux is present in Figure 30. The results show that AFRL 02 loses the most mass during the heating process, while PTI A1 and A2 lose the least mass. AFM samples undergo the most mass loss of the Nat-sand samples, but is still lower than AFRL 02. The mass loss experience by Yuma is about 3% greater than the amount A1 and 10 % less than the amount of AFM. AFRL 02 shows a mass loss that increases as processing temperature increases, without "flattening out" at the highest temperatures. On the other hand, sands such as PTI A1, AFM and Yuma have decomposed the majority of the gas compounds by 1200 °C because further temperature increases have little effect on mass.

The chemical compositions of the samples, presented in Chapter 3, can help explain the mass loss behavior. For example, AFRL 02 and ARAMCO have the most comparable rates of mass loss of all the sand samples. This can partially be attributed to the decomposition of salt (NaCl) present in their makeup. The reason why AFRL 02 has a higher amount of mass loss than ARAMCO is likely due to the additional loss of H_2O and SO_2 from gypsum and CO_2 from dolomite. The slight difference in Yuma and A1 samples suggests that the two have comparable amounts of decomposing minerals within their composition. While this data reflects a small sample size, it does serve to relatively compare mass loss between each sand sample, and alludes to the amount of flux within each sample.

In summary, AFRL 02 has the greatest amount of mass loss, and its most comparable natural sand is AFM. These results lead to a conclusion that AFM has a comparable amount of flux to what appears in AFRL 02. In contrast, the two sand samples, Yuma and A1, are the sand samples that have the least amount of material loss due to decomposition. The difference in AFRL 02 and AFM glassing and mass loss also proves that although more mass loss takes place it doesn't necessarily mean more glassing will occur. Although to further confirm this more petrographic analysis of the AFM should be conducted to confirm the one samples consistency. Again, Nat-sand compositions are very complex therefore the addition of other elements like Fe, K, oxides in the AFM may play a larger role the melting than process than the evaporative compounds.
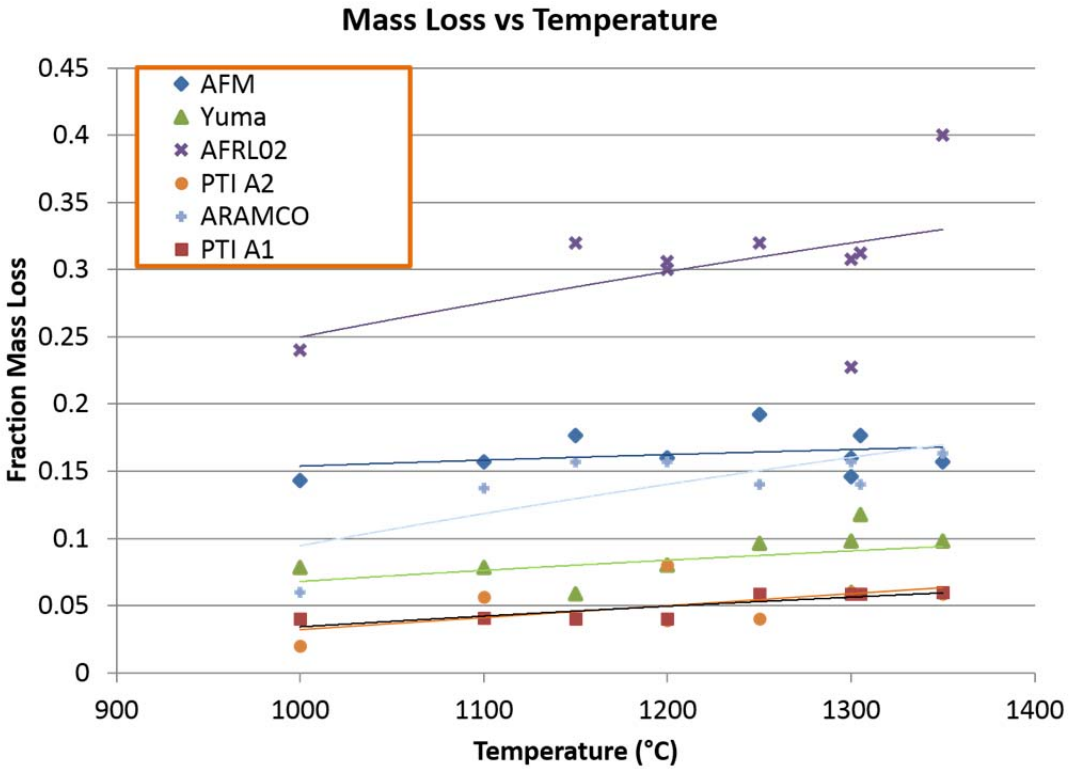
Figure 30: Mass loss analysis of Phase 1 tests.

4.5 Wetting Results

EB-PVD has a columnar microstructure, with distinct individual crystalline columns stacked in close physical proximity, but having weak connections between columns. Fluids that find it energetically favorable to be in contact with EB-PVD material will "wet" the EB-PVD columns and flow into the intercolumnar spaces, thereby infiltrating the top coat [23]. As sand melts, the liquid will infiltrate the top coat and wet the surface of the TBC. This wetting behavior is driven by the viscosity of the molten sand, which in turn is dependent on the flux present in the composition.

At 1150 °C, seen in Figure 31, the compressed chips did not appear to fully melt into a liquid and wet the surface. However, a residue of the material was left underneath the sand chip. The residue left behind, which will be referred to as residual shadows, is likely liquid produced during flux-assisted liquid phase sintering and melting. This is consistently evident in all the TBC samples.
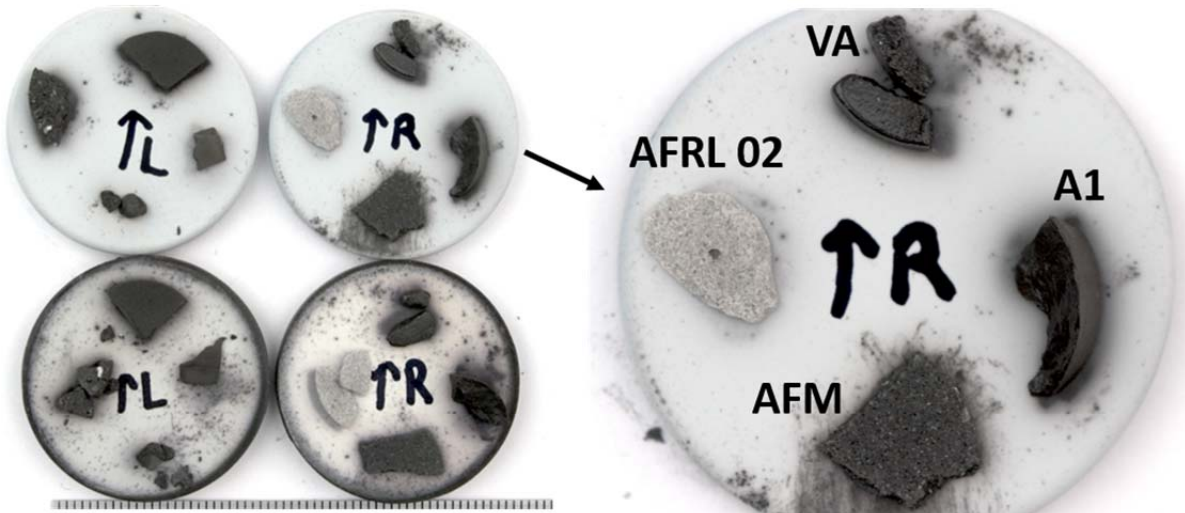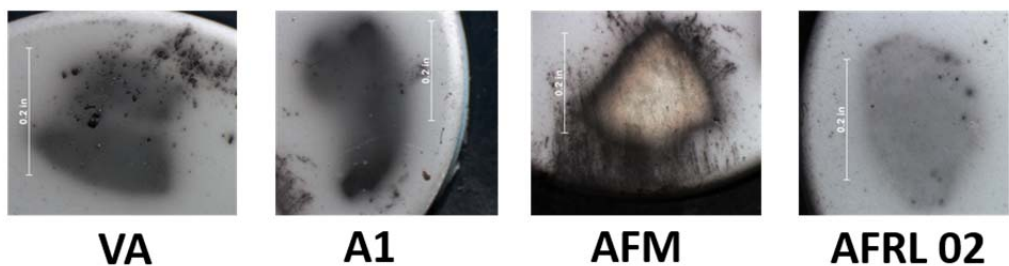
Figure 31: Wetting behavior of Phase 3 samples heated to 1150 ºC. Residual shadows are shown to remain after chips were removed.

At 1200 °C, the thermal energy causes the samples to shrink as liquid phase sintering and melting occurs, seen in Figure 32. As the compressed chips form spherical droplets to decrease free energy, they shrink their contact area, leaving behind residual shadows. Examples of these shadows are present in samples like Helm, A1, Yuma, and AFRL 02. In contrast, the AFM sample finds it more energetically favorable to expand its contact surface at 1200 °C, and somewhat spread out on the TBC surface, wetting it to a larger degree than other sands. It should be noted that the behavior of sand atop Button B TBC substrates cannot be accurately determined as a large number of molten sand samples spalled off during cooling.

At 1250 °C, the various sand samples appear to have melted to the extent that the resulting liquid fully wets the TBC substrate. Sand-to-TBC contact areas increased for Helm, AFM, AFRL 02, Bal Bl, and Afg Bl (on Button B) seen in Figure 33. Yuma, A1 and Afg Bl (on Button A) sample did not wet the surface in a similar way as the samples mentioned earlier. The samples retained a smaller sand-to-TBC surface area and formed rough, irregular, non-shiny surfaces. This difference in wetting behavior is due to low viscosity of the liquid, which means the sands did not contain as much flux.

One last noteworthy result was the difference in wetting behavior of the sand samples on the two buttons. A clear difference is seen in samples of Bal Bl, AFRL 02 and AFM sands. They formed a circular wetting front on Button A substrates, but a more convoluted wetting front on Button B. In samples heated to 1300 °C as shown Figure 34, molten sand atop Button A substrates behaved similar to the 1250 °C condition; sand

atop Button B substrates at the same temperatures, however, completely spalled off during cooling due to thermal expansion mismatch.

In summary, compounds within sand samples formed a small amount of liquid to wet the TBC substrate at the lowest processing temperature in the present study (1150 °C), even though the overall shape of the compressed sand chip only slightly changed. As temperature was increased to 1250 °C, a greater amount of liquid formed, leading to sand consolidation and wetting of the TBC surface. The Mfg-sand AFRL 02 consistently flowed and wet the TBC surface in ways similar to Helm, AFM, and Bal Bl. The sand samples that did not behave as these were Yuma, PTI A1, and Afg Bl. This is likely due to the lack of flux present in their sand composition, and therefore, a lower viscosity of the melted liquid.
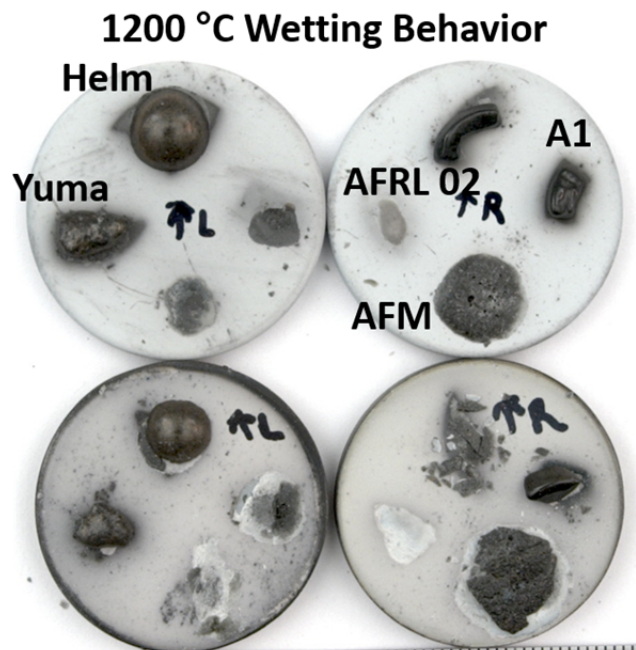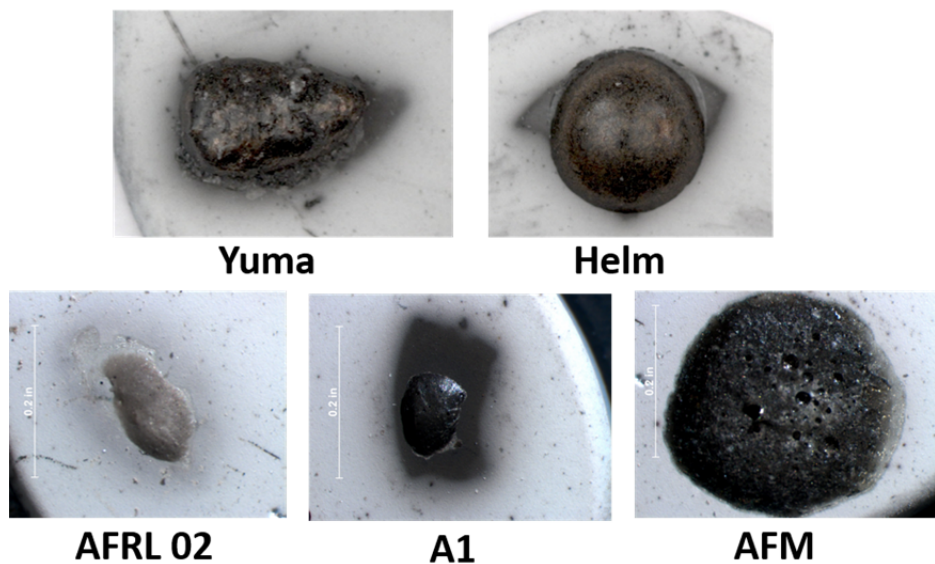
Figure 32: Wetting behavior of Phase 3 heated on TBCs at 1200 ºC.
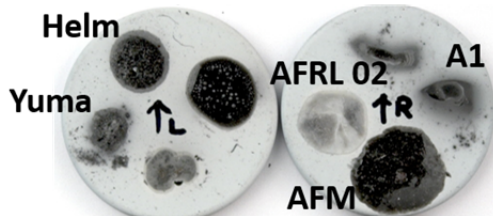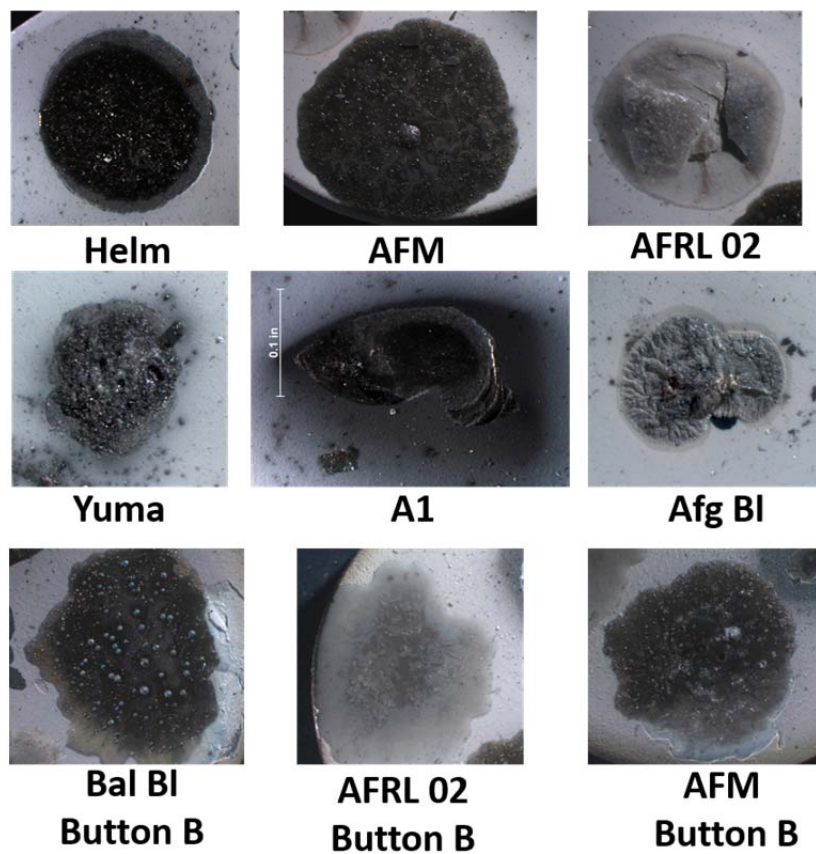
Figure 33: Wetting behavior of Phase 3 heated on TBCs at 1250 ºC.
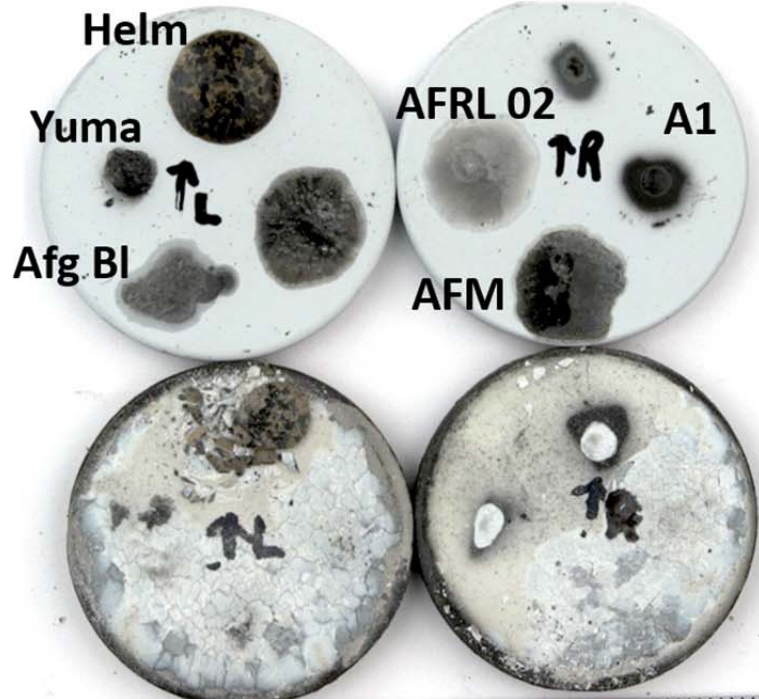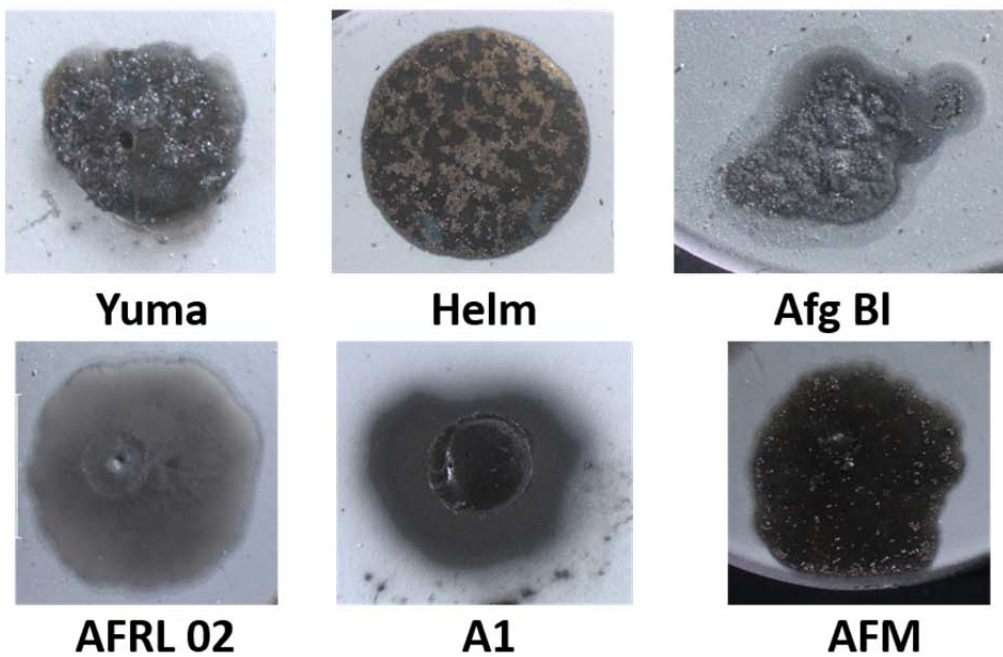
Figure 34: Wetting behavior of Phase 3 heated on TBCs at 1300 ºC.

4.6 Infiltration Results

Further information regarding the wetting of the TBC by molten sand was provided by investigating the edge of molten sand and the TBC beneath. By viewing the heated sand's perimeter atop the TBC, a comparison can be made between the TBC area directly underneath the sand and the TBC having no molten sand on top. A cross-sectional view of Yuma and AFRL 02 samples heated to 1200 °C can be viewed in Figure 35. Infiltration was clearly evident, observed through dark field reflectance microscopy as discussed in Chapter 3. In the Yuma sample, the infiltrated area is labeled "infiltrated" with a visually observable boundary indicated with a dashed line. The appearance of the infiltrated region was found to be gray with a bluish tint and with dim light black regions interspersed; little contrast was present in this region. The area labeled "non-infiltrated" showed no evidence of any liquid infiltration, and was found to be light blue with bright white specks interspersed with a high amount of brightness and contrast. In the AFRL02 cross section, there is a dashed line dividing the infiltrated area and the non-infiltrated area, also seen in Figure 35. Infiltrated and non-infiltrated regions of AFRL 02 specimen showed a similar difference in appearance as described above for Yuma.

Liquid infiltration into the TBC top coat was also examined in A1 and AFM samples. A1 cross-section, Figure 36, shows an area of infiltration, evidenced by the residual shadow mentioned in previous sections. The AFM sand photo depicts a sample section directly underneath the molten sand, instead of the wetting edge boundary. This section shows gray columns with no bright spots. AFM sand also has additional light

black lines near the surface of the top coat, and these lines that extend through half of the top coat. These light black lines are indicated by the arrows in Figure 36.

Infiltration of the TBC by liquid was validated by SEM imaging and elemental mapping of AFRL 02 heated to 1200 °C.   In Figure 37, the SEM photomicrograph shows the wetting edge of AFRL 02. The SEM photomicrograph clearly indicates the presence of liquid infiltration into the intercolumnar spaces in the region of TBC both underneath and next to the molten sand. Several locations are identified where glass is found between TBC columns. An infiltration boundary line has been placed at the position where the glass ceases to exist between the columns. To further validate this phenomenon, an elemental map was created, scanning for glassing elements such as Si, Ca, Mg, and Al to see if the materials containing these elements infiltrated the intercolumnar spaces. As shown in Figure 38, Si and Ca were very prominent between the YSZ columns. This further validates that the TBC has been infiltrated by the sand sample.
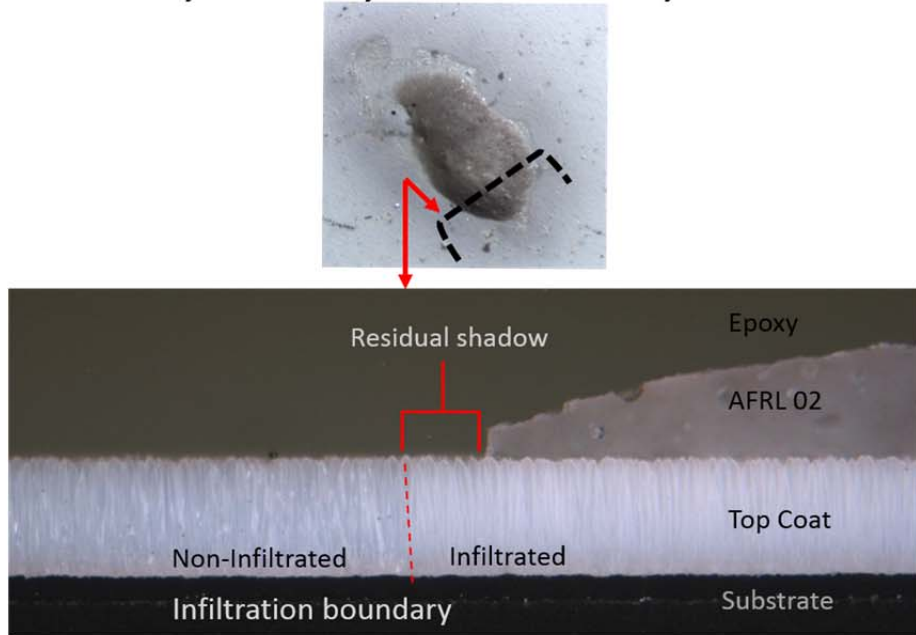
Figure 35: Optical Microscopy of Yuma and AFRL 02 samples heated to 1200 °C infiltrating TBC. Cross-section images taken optically in dark field view. Black dashed line in top view indicates location cross-sectional cut. Red dashed line in cross-section view indicate infiltration boundary.

A1, 1200 °C, Cross-section, Button A
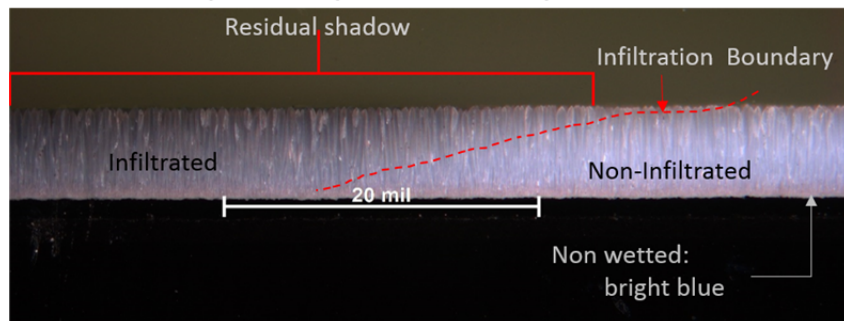
**AFM, 1200 °C, Cross-section Button A**
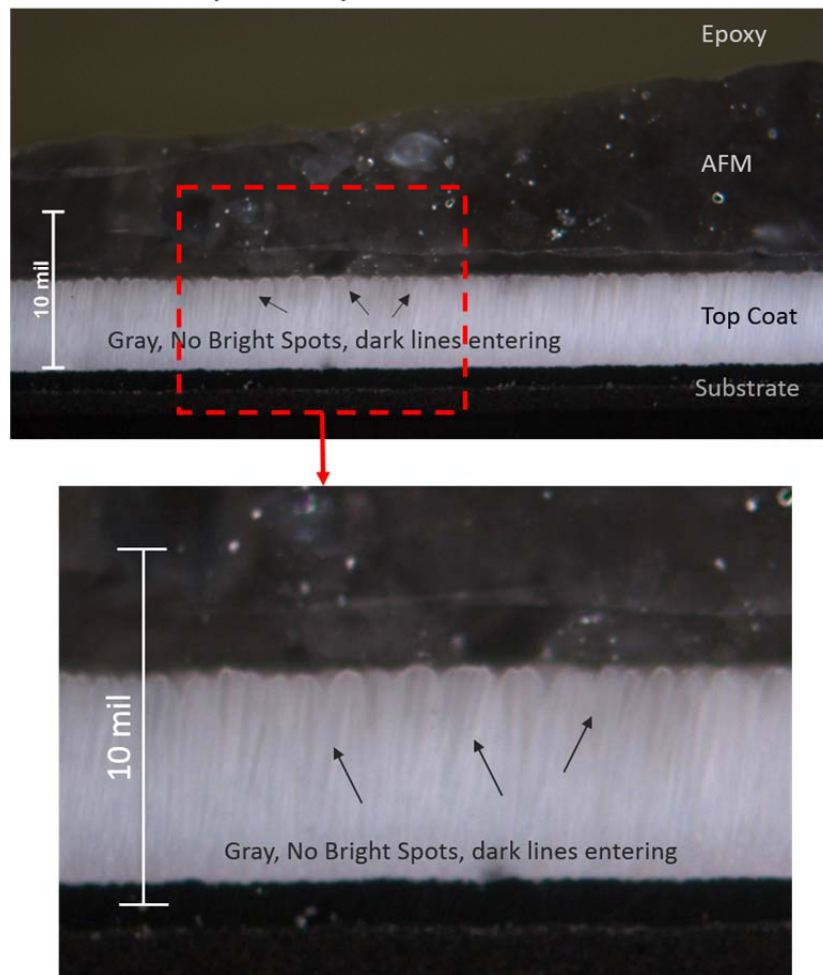
Figure 36: Optical cross-section of A1 and AFM sample heated to 1200 °C by dark field microscopy. A1 sample has a gradual boundary indicating where sample wet the surface. AFM sample presents colors typical of

infiltration with addition of light black lines, indicated by arrows, near the surface of the top coat.
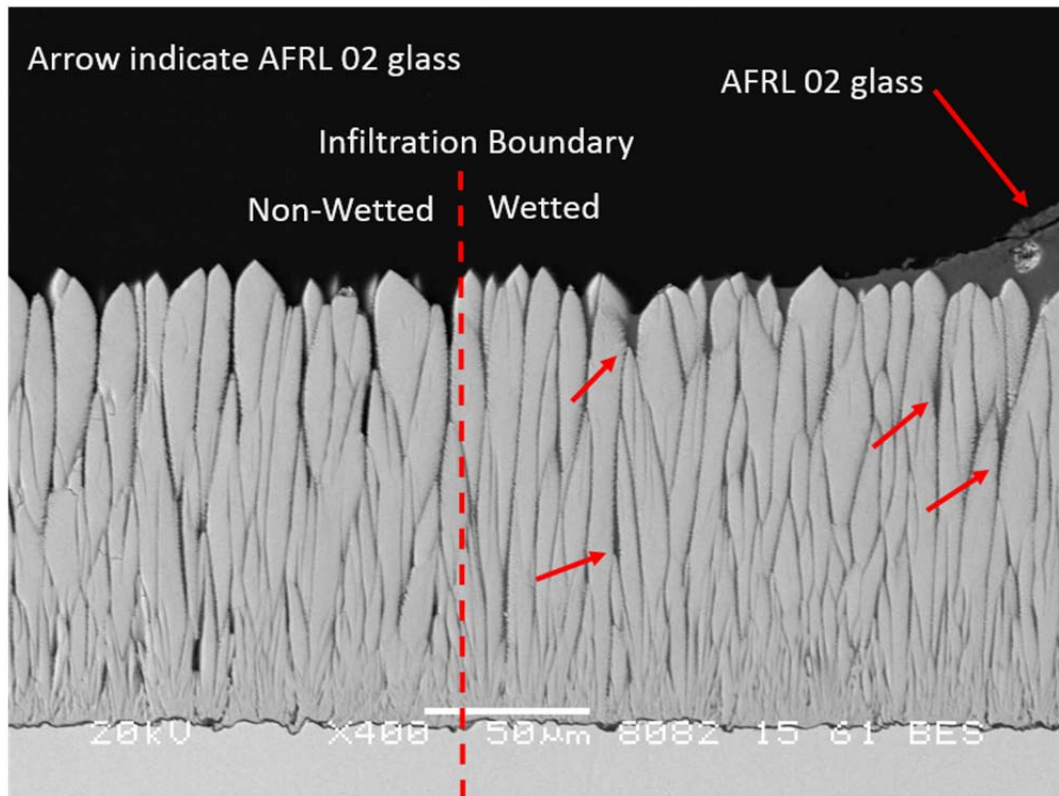
Figure 37: SEM photomicrograph of AFRL 02 heated to 1200 °C on Button A. Arrows indicate AFRL 02 glass between top coat columns.
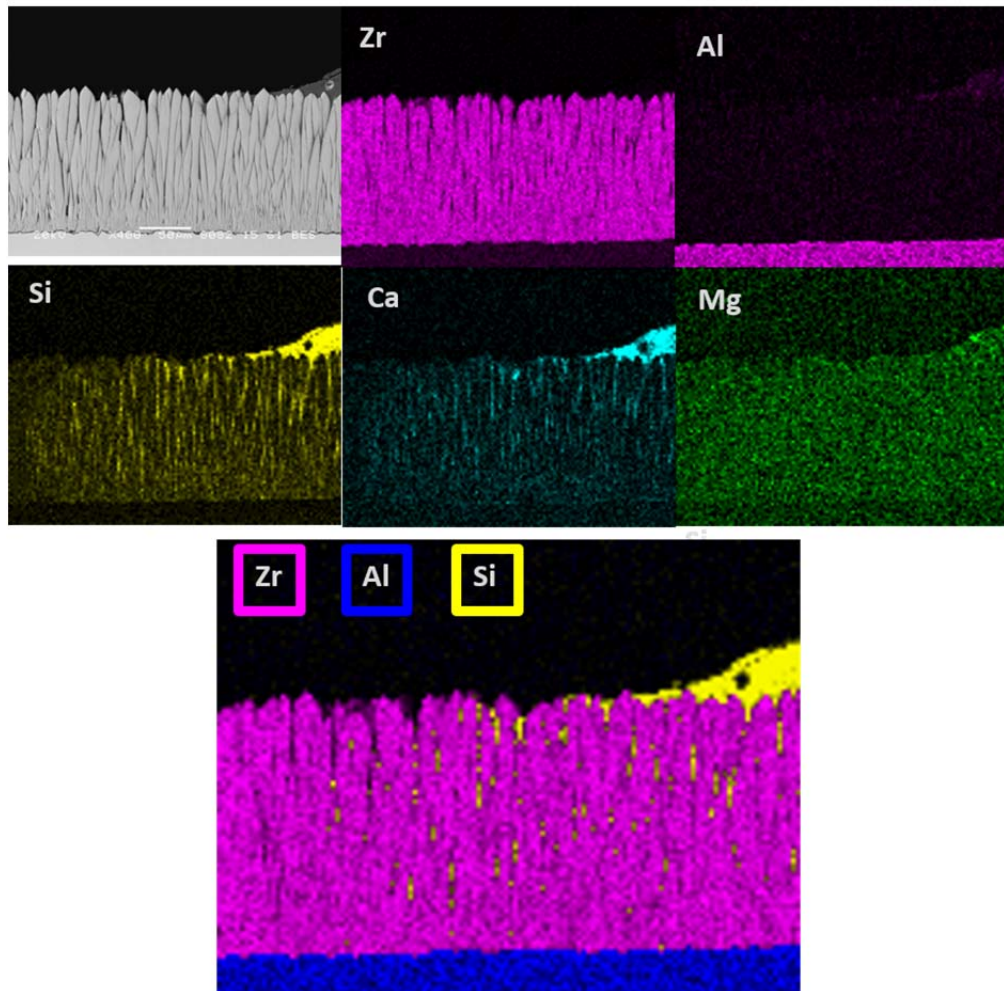
Figure 38: Element map of AFRL 02 heated to 1200 °C on Button A, showing infiltration by Si and Ca into the TBC columnar structure.

Some of the same indicators of infiltration at 1200 °C were also found in specimens heated to 1250 °C. In Figure 39, infiltration is shown in the Yuma and AFM samples. A noticeable area of non-infiltrated TBC is outlined in the top photo, while the expanded view of the droplet (middle photo) highlights the region of infiltration. Also, the images indicate that the molten Yuma droplet did not behave like the typical bulk

samples, and did not readily spread out across the surface like the bulk material. This behavior confirmed the wetting results (discussed previously) in which Yuma sand did not wet the TBC surface as did Afghanistan samples. In the AFM sample (Figure 39, bottom photo), there is also a noticeable difference in the infiltrated and non-infiltrated region.

Processing at 1250 °C caused some samples to spread across a much larger TBC surface area than at lower temperatures. Cross-sections of the wetting edge of Bal Bl on Button A, and AFRL 02 on Button B, and AFM on Button A, are shown in Figure 40. The Bal Bl image indicates the infiltration boundary of the liquid glass and the region of unaffected TBC. The image also indicates a gradual change in slope of the molten sand sample as it readily flows across and wets the TBC surface, seen in the top view images of Figure 33. Thus, even though in this region there was a seemingly non-existent amount of Bal Bl sand on top of the TBC, at high temperatures liquid infiltration appears to have taken place.

The AFRL 02 sample heated to 1250 ºC in Figure 40 also shows a gradual increase in wetting angle, similar to that of the Bal Bl sand. However, this increase is less than the increase of the angle seen in AFRL 02 sample heated at 1200 ºC (Figure 35). Figure 40 also shows an AFM sample that appears to flow less readily across the TBC surface, possibly due to the amount of AFM used in testing when compared to the other sands. The top view image in Figure 33 clearly indicates a larger amount of AFM sand sample than the other samples. The wetting angle compared to AFRL 02 and Bal Bl is greater than both.

Another feature present in the top coat was "spotting". Black spots – sometimes black streaks like those presented in Figure 41 – were only found directly below a sand sample, not in the region adjacent to the wetting boundary. These spots were found both within Button A and Button B TBC layers, and were of various dimensions. However, they were consistently vertically parallel to the top coat columns. In Nat-sand samples AFM, Afg Bl, and Helm, dark field optical microscopy showed the presence of dark, black spots, whereas in Mfg-Sands, AFRL 02 and A1, the spots were lighter gray as shown in Figure 42. In Nat-sands more spots were present than in the Mfg-sands. The composition of these spots was not analyzed in the present study, as such an investigation was beyond scope; such an analysis should be added to future work. It was noted that the spots did not form in a consistent layer or a specific position within the top coat. Figure 42 shows some dark spots are located at the surface of the top coat as shown in the Helm sample; some spots formed at the bottom as shown in AFRL 02. In Afg Bl, spots formed at the top and the bottom of the TBC top coat, while in AFM the spots spanned the entire thickness of the TBC layer. Though the exact composition of theses spots is not known, their location clearly indicates that they originated as a result of molten sand atop the TBC.
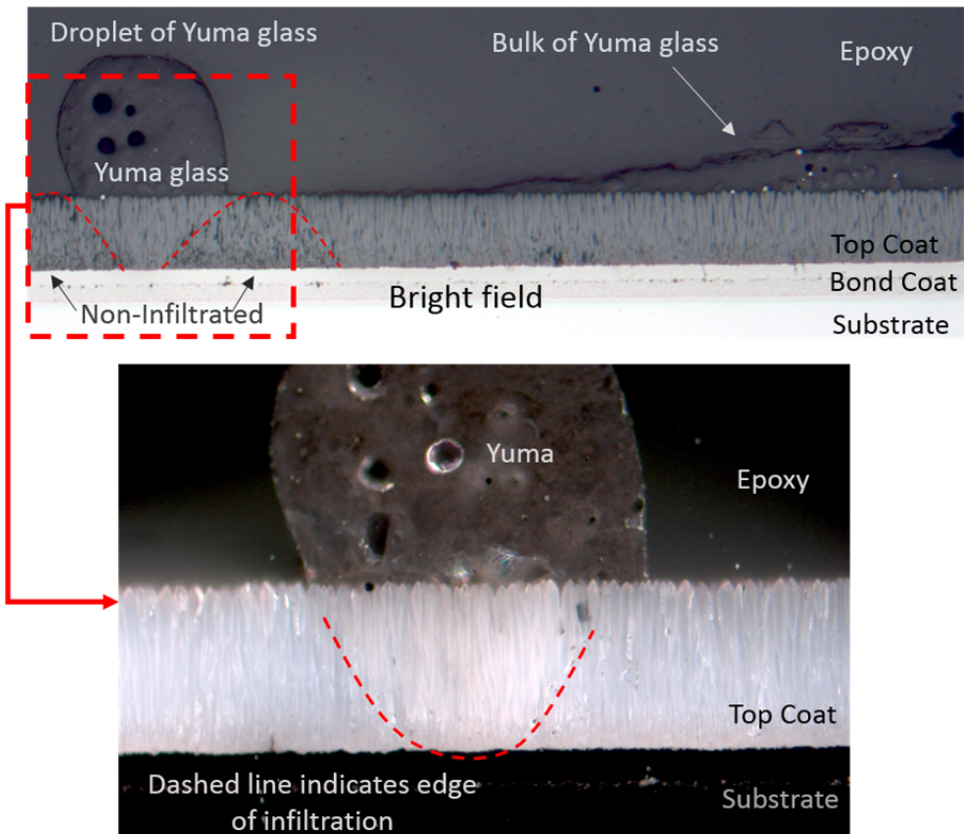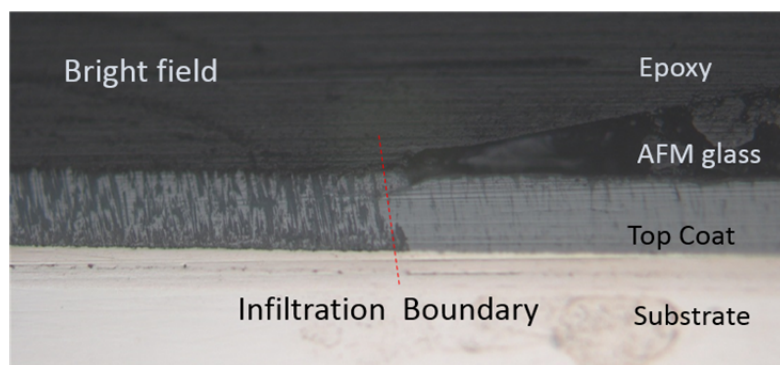
Figure 39: Optical cross-section image of Yuma and AFM heated to 1250 °C. Dashed curve indicates the edge of Yuma sample infiltrated into the top coat. Top Yuma image is presented in bright field microscopy while inset Yuma image is presented in dark field microscopy. AFM sample, imaged in bright field, indicates infiltration boundary by separating with a dashed line.
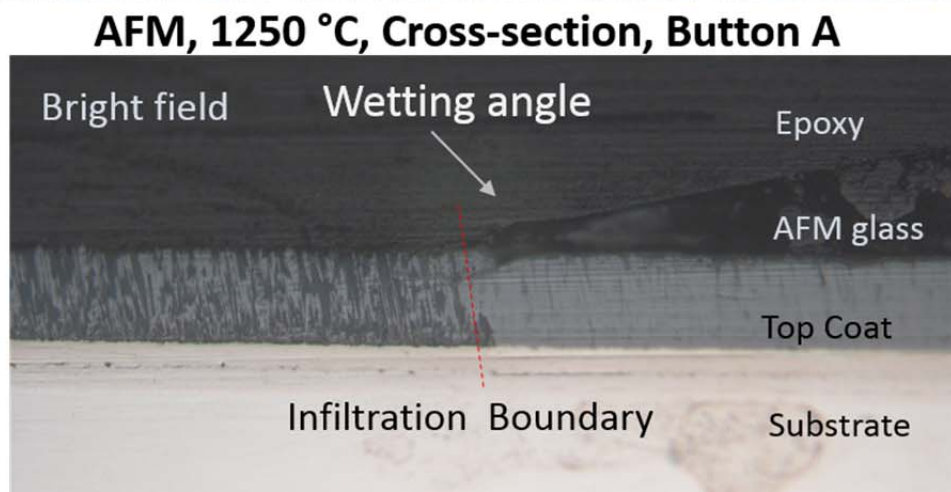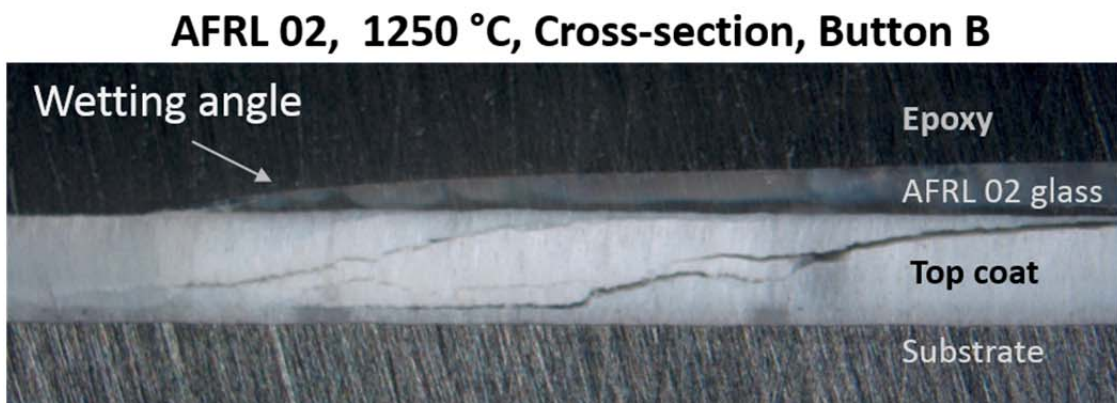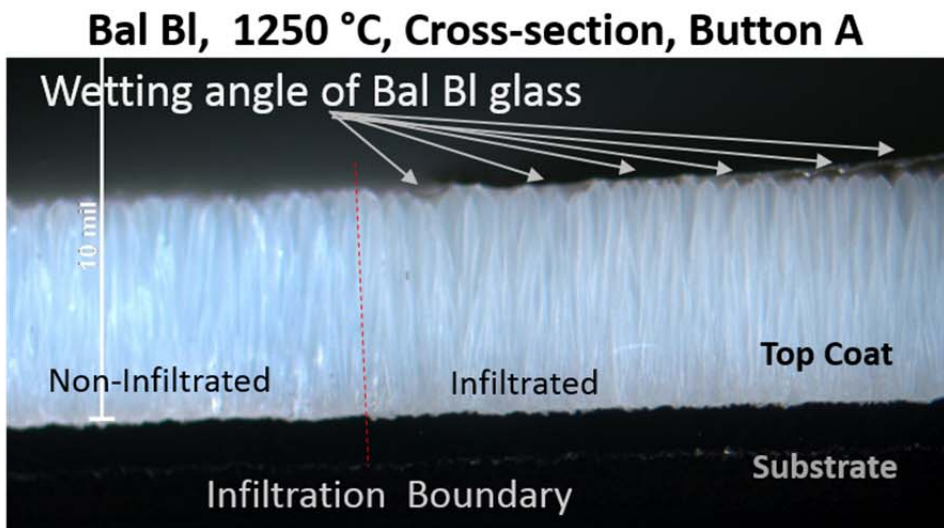
Figure 40: Optical cross-section images of Bal Bl and AFRL 02 heated to 1250 ºC. Arrows indicate wetting angle of sample on top coat. Bal Bl

and AFRL 02 imaged in dark field microscopy. AFM imaged in bright field microscopy.
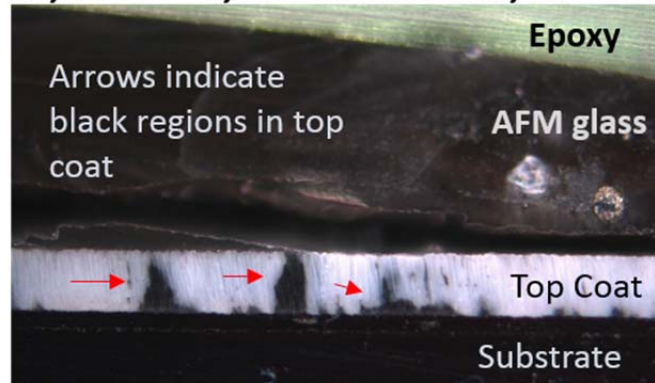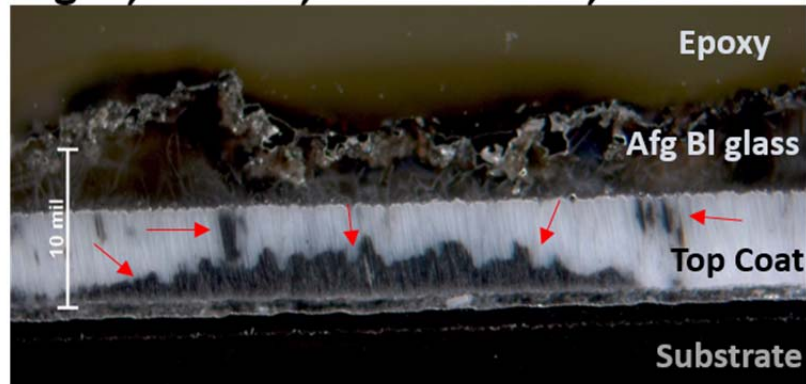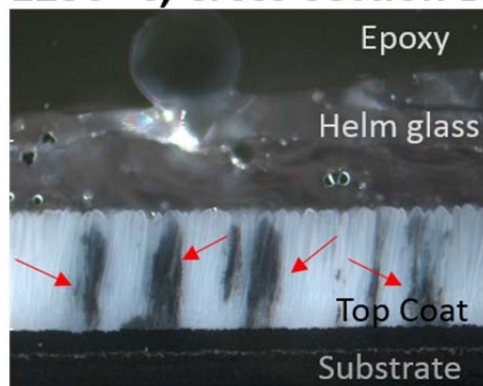

Figure 41: Optical cross-sections of AFM, Bal Bl, and Helm heated to 1250 °C on Button A. Arrows in each sample indicate black regions within

the top coat. Black material is only found underneath glass deposits. All images are captured in dark field microscopy.

Helm, 1250 °C, Cross-section, Button B

AFRL 02, 1250 °C, Cross-section Button B
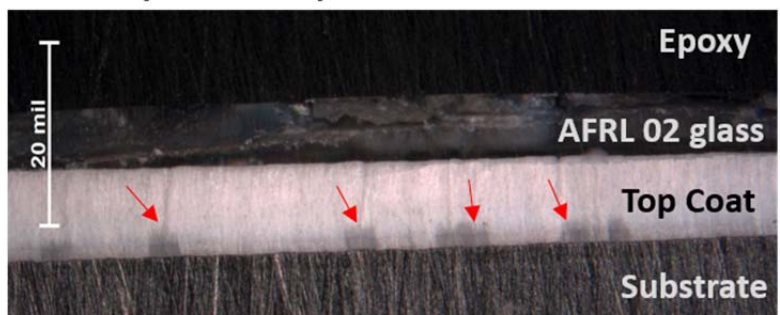
## A1, 1250 °C, Cross-section, Button B

Figure 42: Optical cross-section images of Helm, AFRL 02, and A1 heated to 1250 °C on Button B. Arrows in each sample indicate black regions within the top coat. Black material is only found underneath glass deposits. All images are captured in dark field microscopy.

Samples heated to 1300 °C had many of the same features as those heated to 1250 °C. Examples of infiltration and spotting can be seen in Figure 43. The Nat-sands and Mfg-sands both showed clear signs of liquid infiltration, with no distinguishable difference between the two. As mentioned earlier in this chapter, samples tested atop TBC Button A remained intact upon cooling from 1300 °C, while spallation occurred in samples atop TBC Button B. Despite this spallation, the remaining TBC top coat was cross-sectioned and analyzed. In some Button B specimens, brown discoloration lines were found – a feature not seen previously and not occurring in Button A samples. A few examples of these brown lines are presented in Figure 44. These lines may be a form of additional infiltration and/or reaction with compounds within the TBC. Compositional analysis of these lines should be conducted in future work.

In summary, sand samples heated from 1150 °C to 1300 °C experienced liquid infiltration of the TBC top coat. The degree of infiltration increased as processing temperature increased and facilitated flow across the TBC surface. The Nat-sands at 1250 °C produced more black spots than the Mfg-sands, and these spots were also darker in color. Without further elemental analysis of the infiltrated areas, more detailed comparisons between the Nat-sands and Mfg-sands cannot be made.
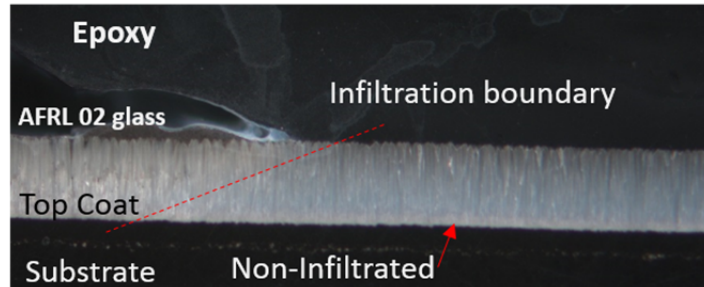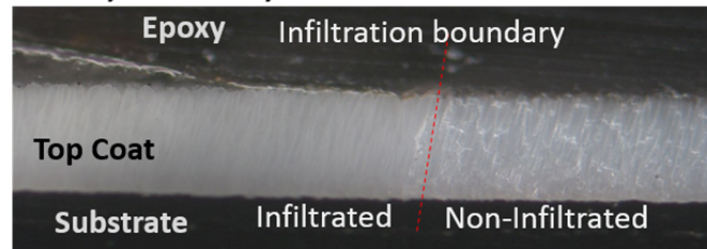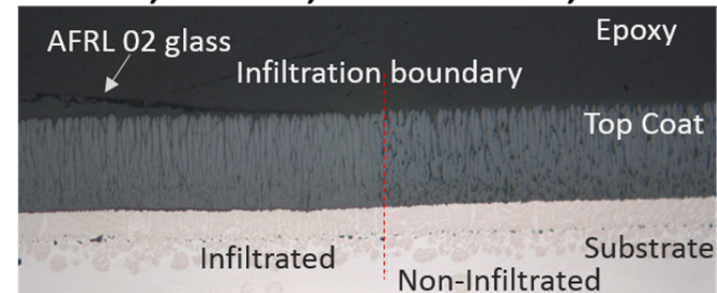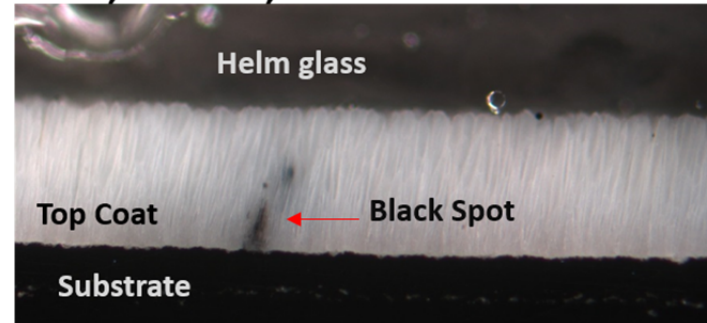
Figure 43: Optical cross-sections images of A1, Helm, and AFRL 02 heated to 1300 °C. Photos highlighting infiltration boundaries and black spots. A1 and Helm images are captured in dark field microscopy. AFRL 02 image is captured in bright field microscopy.
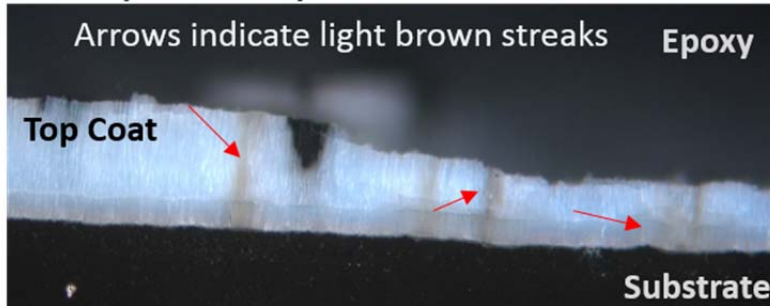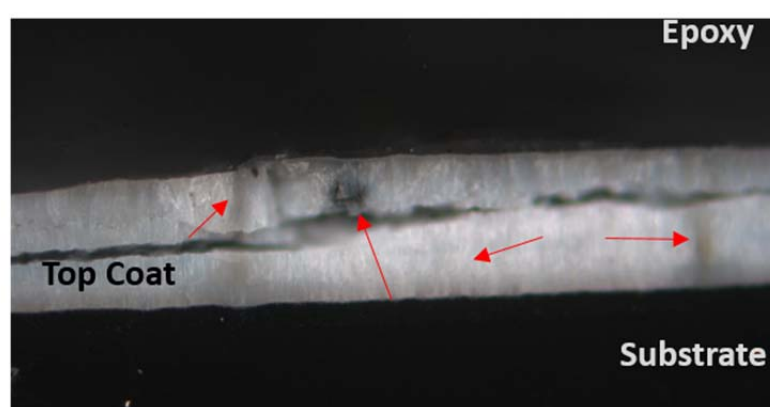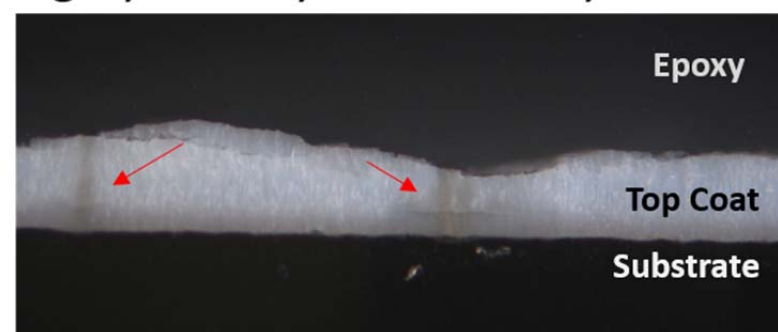
Figure 44: Optical cross-section images of Bal Bl, Helm, and Afg Bl heated to 1300 °C on Button B. Arrows in each sample indicate brown streaks within the top coat. Brown streaks only found in Button B. Images presented in dark field microscopy.

4.7 Delamination Cracking Results

Infiltration of a turbine blade TBC top coat by molten sand can result in severe damage upon cooling. Thermal expansion mismatch between infiltrated and pristine YSZ, combined with a cooling ΔT of 1000 °C, induces a thermal misfit strain which can cause cracking of the top coat. In the present study, such behavior was observed in several specimens. During cross-sectional analysis, cracks were observed within the top coat of some of the heated samples. Figure 45 illustrates cracks initiated or formed as a result of liquid infiltration into the top coat – cracking appeared to coincide with the demarcation between infiltrated and pristine TBC. Photos were taken in bright field microscopy and dark field microscopy to enhance crack visibility. The AFM sample shows a crack forming at the edge of the wetting boundary, and a crack laterally extending through multiple YSZ columns underneath the sample. The Helm sample also illustrates a crack propagating from the edge of the wetting boundary. In the A1 specimen, a crack has formed underneath the sample and has propagated in a lateral direction through half of the thickness of the top coat.

The AFRL 02 sample, seen in Figure 46, shows a network of cracks that have propagated through the top coat toward the top coat/TBC interface. Figure 47 from Mercer et al. [29] on cracking and delamination mechanisms of TBC on turbine blades suggests the cracks have originated from the surface of the top coat, and are formed from "cold shock". These cracks are consistent with those shown in AFRL 02 (Figure 46) and those cracks shown in Figure 45.

Additionally, sand specimens tested atop Button B TBC substrates showed clear evidence of excessive thermal misfit strain from "cold shock" upon cooling, resulting in complete spallation of solidified molten sand. Since both Button A and Button B tests were conducted under the same conditions, the spallation on Button B specimens likely results from composition or morphology differences between the two TBC substrate manufactures. The spallation/delamination was most prevalent on samples heated to 1300 °C, but also occurred on samples heated to 1250 °C and 1200 °C. Examples highlighting this phenomenon can be viewed in Figure 48. The buttons heated to 1200 °C saw complete spallation of Bal Bl, Afg Bl, and AFRL 02 upon cooling. Residual strain eventually led to spallation of AFM and Helm as well, although spallation occurred shortly after images were taken.

Close visual inspection of the damaged area showed clear evidence that failure occurred within the EB-PVD top coat of Button B. On specimens heated to 1300 °C, the majority of the top coat was removed from the substrate during spallation, leaving behind depressed regions, and in some places, exposing the TGO/BC underneath. On the rightmost button (Figure 1Figure 48), spallation was observed at approximately the midpoint of the top coat.

In summary, upon cooling, cracks developed within the top coat of several test specimens due to infiltration of the TBC by liquid from molten sand. This type of cracking is consistent with research performed on turbine air foils affected by CMAS. TBC delamination and spallation are also commonly-reported failure modes of in-service

TBC coatings in turbine engines operating in sandy environments. Such behavior was seen in several specimens in the present study.
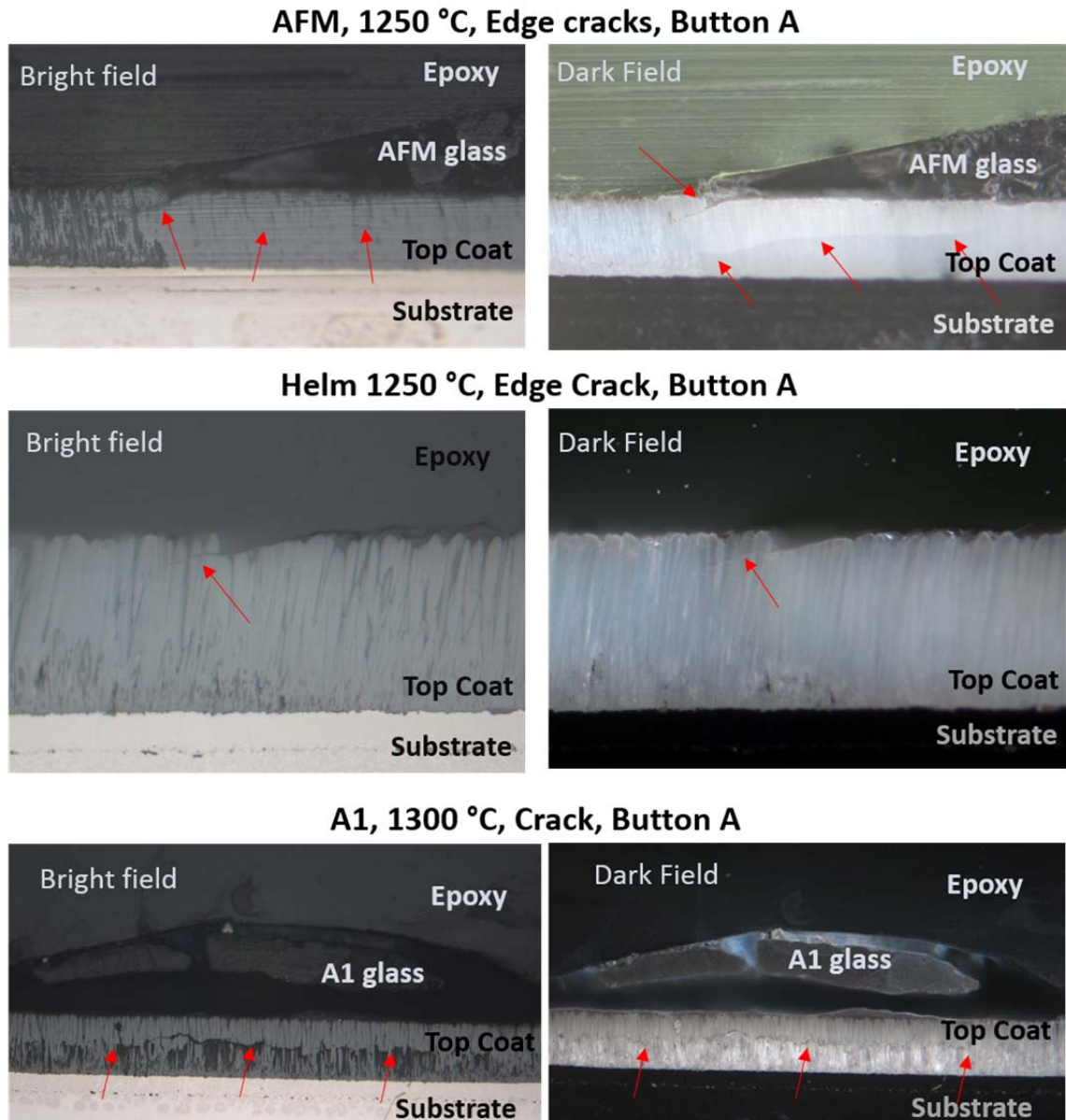
Figure 45: Examples of cracking within the TBC due to infiltration. The arrows indicate the location of cracks.
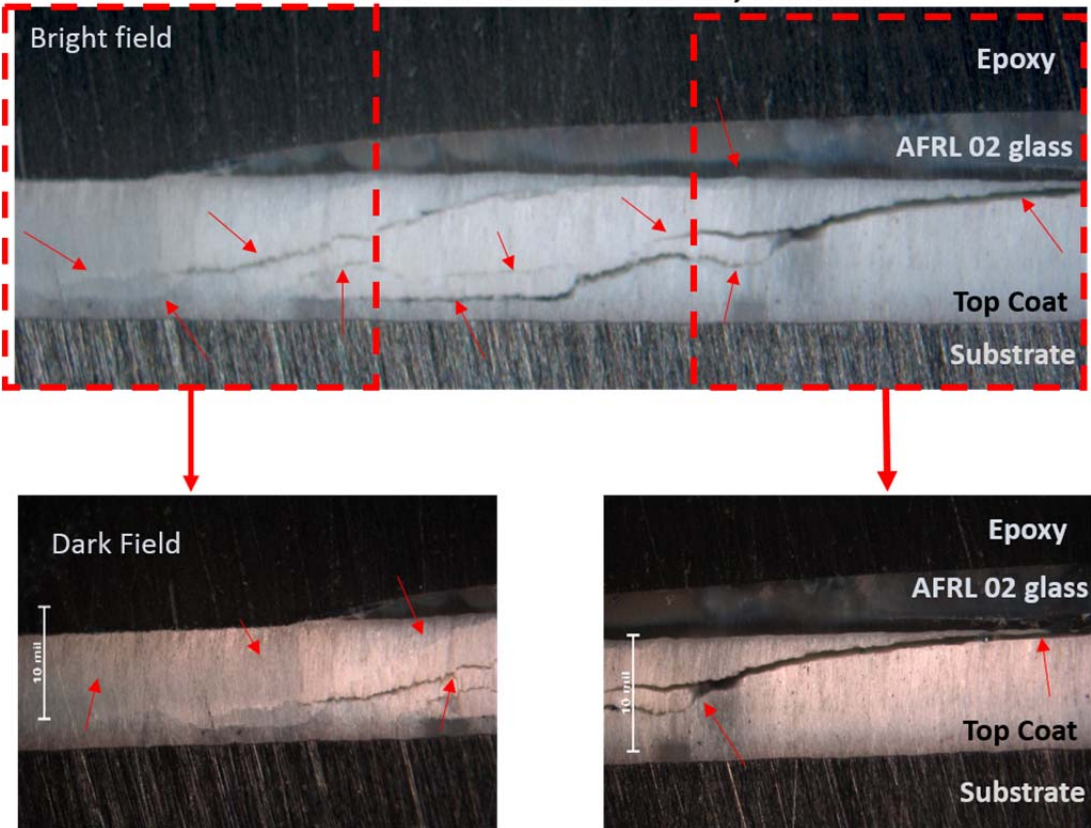
Figure 46: Optical microscopy of a network of cracks propagating through the top coat from AFRL 02 heated to 1250 °C.
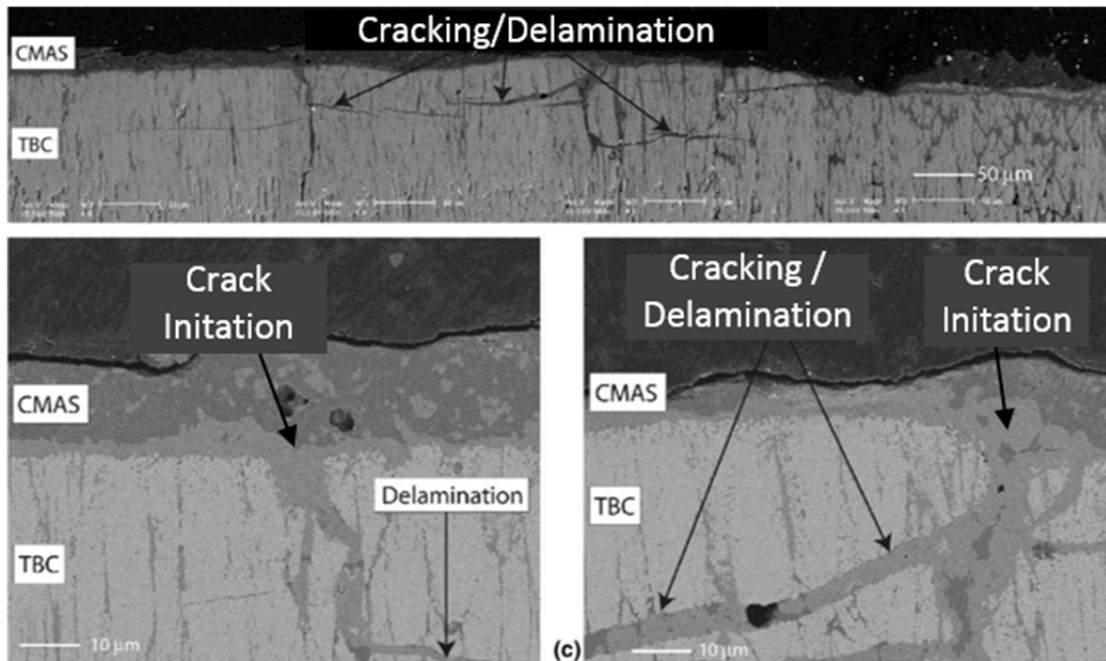
Figure 47: SEM Micrograph of cracking and delamination in Mercer et al. [29], similar to AFRL 02 cracking when heated to 1250 °C and cooled to room temperature.

Figure 48: Button B illustrates missing TBC, indicated by the red circles, and in "All" regions.

4.8 Summary of Results

Both Nat-sands and Mfg-sand specimens were studied in Phase 1, Phase 2, and Phase 3 test protocols in the present study. All sand samples tested showed clear evidence of liquid formation, even when tested at relatively low temperatures (1000 °C).

In Phase 1 studies, all sands showed evidence of liquid phase or solid state sintering at 1000 °C, culminating in the formation of droplets at 1300 °C. Similar behavior was seen in Phase 2 studies, with all sand compositions forming partial-wetting droplets atop Ni substrates, with one exception, the relatively large-grained QGCS. Due to surface energy differences between Ni and EB-PVD substrates, during Phase 3 testing, specimens appeared to have better wet the YSZ topcoat, flowing across the surface and infiltrating the TBC. Yuma and A1 were the exceptions to this behavior, as they wetted the surface with lower viscosity, therefore decreasing surface area.

In petrographic analysis, the Mfg-sands retained a higher content of crystallized minerals than did Nat-sands when processed at 1200 °C, likely due to a larger and more diverse population of natural minerals as compared to sands prepared in a laboratory. After processing at 1300 °C, however, both Mfg-sands and Nat-sands were largely amorphous as the higher temperature compensated for compositional differences.

Rate and temperature of liquid formation in the various sand compositions tested in the present study varied; however, the behavior of the Nat-sands Yuma and AFM was comparable to Mfg-sands A1 and AFRL 02, respectively. The Phase 3 tests verified that when at the lowest temperatures, liquid infiltrated the TBC.

Observations of specimen cross-sections clearly showed the infiltration of liquid into the intercolumnar spaces of the TBC top coat. Additionally, in Nat-sand samples, the presence of light black lines, spots, and large discolored regions was observed throughout the thickness of the TBC directly beneath the sand sample. SEM imaging and EDS analysis also confirmed that the liquid from the sand sample infiltrated the TBC top coat. Top coat cracking was seen in several samples, including AFM, Helm, A1, and AFRL 02.

V. Conclusions and Recommendations

5.1 Conclusions of Research

The overall goal of this research was to determine if the Mfg-sands used in current turbine engine testing melt, wet, and infiltrate TBCs in the same manner as Nat-sands. Of the Nat-sands tested, AFM and Yuma were the sands used through all three phases of testing. Thus, the analysis of these two sands gathered an accurate profile of their behavior in regards to melting, petrography, mass loss, wetting, and infiltration.

Results largely confirmed that the Mfg-sand AFRL 02 most closely resembled the AFM sand. Their similarities are as follows:

1. They transitioned into similar spherical pellets at 1350 ºC.

2. They produced similar amounts of glass at 1300 ºC with similar particle configurations.

3. They had the two greatest mass losses of all the samples.

4. They wet the surface of the TBC in similar ways.

5. They infiltrated and cracked the TBC in similar ways.

The wetting, infiltration, and cracking behavior of AFRL 02 was also similar to the respective activities of the Nat-sands Helm and Afg Bl.

The Mfg-sand that most closely resembled the Nat-sand, Yuma, was A1. The two sands behaved similarly to each other in the areas of melting, petrography, mass loss, wetting, and infiltration. The melting behavior of Mfg-sand QGCS was not at all similar to any of the other sands, either natural or manufactured.

5.2 Significance of Research

Turbine engines continue to fail due to the ingestion of sand in desert environments. The current use of manufactured sands QGCS and PTI A1 in engine testing has proven unsatisfactory, demonstrated by the persistence of engine complications. A sand that better represents the way natural sand attacks TBCs in Middle Eastern desert regions is needed. The results of the present study suggest that the Mfg-sand AFRL 02 be used in qualification testing in order to ensure findings are comparable with real world sand ingestion in Middle Eastern desert regions.

AFRL 02 sand could be used in initial engine acceptance testing, in place of the currently used QGCS and PTI A1 sands. Because its behavior better matches that of Nat-sand, the use of AFRL 02 in place of Sim-CMAS would also be helpful for research into TBC failure mechanisms and in thermal cycling tests. AFRL 02 could be used for the testing of CMAS-resistant TBCs, such as those developed by Aygun, et al. [33]. Such testing could help determine if the novel coatings will also be resistant to Nat-sand. AFRL 02 would serve to help in the development of future TBCs.

5.3 Recommendations for Future Research

While this research compared Nat-sands side-by-side with Mfg-sands, further research still needs to be conducted even within the samples and test conditions presented. Immediate further research should be conducted on:

- The exact composition and particle distribution size of the Nat-sands used in this study.

- Petrography results of melted Helm.

- Petrography results of multiple samples of AFRL 02, ARAMCO, AFM, PTI A2, PTI A1, and Yuma.

- Additional cross-sectional investigation of samples by SEM imaging and EDS analysis to determine if actual CMAS is infiltrating the TBC, or if the liquid present lacks one of more of the CMAS elements (Si, Ca, Al, and/or Mg).

- Composition of the black spots, seen in Figure 41 and Figure 42, from both Nat-sands and Mfg-sands within the columnar microstructure of the TBC.

- Analysis of light brown lines found in Button B (Figure 44) to determine if their composition or other factors contribute to the devastating spallation that occurred.

- Evaluating Sim-CMAS used in other TBC/CMAS interaction studies to compare the sintering and melting behavior with that of the Mfg-sands used in the present study.

These additional studies would be expected to provide further information on the suitability of AFRL 02 as an analogue of Nat-sands from Afghanistan. In addition, by analyzing Sim-CMAS as it compares to Nat-sands, suggestions for improvement can be made on prior CMAS/TBC interaction testing.

References

[1] J. L. Smialek, F. A. Archer and R. G. Garlick, "Turbine Airfoil Degradation in the Persian Gulf War," *JOM,* pp. 39-41, 1994.

[2] D. J. de Wet, R. Taylor and F. H. Stott, "Corrosion Mechanisms of ZrO2-Y2O3 Thermal Barrier Coatings in the Presence of Molten Middle-East Sand," *Journal of Physics IV,* pp. 655-663, 1993.

[3] S. Kramer, J. Yang and C. G. Levi, "Thermochemical Interaction of Thermal Barrier Coatings with Molten CaO-MgO-Al2O3-siO2 (CMAS) Deposits," *Journal of the American Ceramic Society ,* pp. 3167-3175, 2006.

[4] Department of Defense, *Department of Defense Joint Service Specification Guide Engines, Aircraft, Turbine,* Department of Defense, 2007.

[5] M. Zucrow, Aircraft and Missile propulsion, vol. volume 1, New York: John Wiley & Sons, Inc, 1958, p. 51.

[6] W. W. Bathie, Fundamentals of Gas Turbines, New York: John Wiley & Sons, Inc., 1996.

[7] M. P. Boyce, Gas Turbine Engineering Handbook, Burlington, Ma: Elsevier Inc., 2006.

[8] N. Cumpsty, Jet propolusion: A simple guide to the aerodynamic and thermodynamic design and performance of jet engines (2nd ed.), Cambridge, United Kingdom: Cambridge University Press, 2003.

[9] H. Cohen, G. F. Rogers and H. I. H. Saravanamuttoo, Gas Turbine Theory, England: Longman Group Limited, 1996.

[10] J. R. Kelley, L. D. Wakeley, J. R. McKenna and S. S. Jackson, "Physical Characteristics of Soil Collected in Iraq and Afghanistan Related to Remote Sensing," Geotechnical and structures Laboratory (U.S), Vicksburg, MS, 2010.

[11] D. Education, "The Dirt on Soil - Learning Adventrures," Educational Web Adventures, 2014. [Online]. Available: http://school.discoveryeducation.com /schooladventures /soil /name_soil.html. [Accessed 26 May 2014].

[12] C. A. Rigsby, "GEOL 4010/11: Introduction to Depostional Systems and Grains," Department of Geological Sciences East Carolina University, 22 August 2010. [Online]. Available: http://core.ecu.edu/ geology/ rigsbyc/ rigsby/ Sedimentology/ SizSortingShape.jpg. [Accessed 16 June 2014].

[13] T. J. Mack, M. A. Akbari, M. H. Ashoor, M. P. Chornack, T. B. Coplen, D. G. Emerson, B. E. Hubbard, D. W. Litke, R. L. Michel, L. N. Plummer, M. T. Rezai, G. B. Senay, J. P. Verdin and I. M. Verstraeten, "Conceptual Model of Water Resources in the Kabul Basin, Afghanistan," U.S. Geological Survey, Reston, Virginia, 2010.

[14] J. P. Englebrecht, E. V. McDonald, J. A. Gillies and A. W. Gertler, "Department of Defense Enhanced Particulate Matter Surveillance Program," Desert Research Institute, Reno, Nevada, 2008.

[15] L. C. De Jonghe and M. N. Rahaman, "Sintering of Ceramics," in *Handbook of Advanced Ceramics*, Elsevier Inc, 2003, pp. 187- 264.

[16] W. D. Kingery, H. K. Bowen and D. R. Uhlmann, Introduction to Ceramics, New York: John Wiley & Sons, 1976.

[17] E. Suvaci, "Sintering of Ceramics Theory and Practice," Anadolu University, 13 February 2008. [Online]. Available: http://home.anadolu.edu.tr/ ~esuvaci/ egitim/ Sintering%20of%20Ceramics-Overview.pdf. [Accessed 17 June 2014].

[18] M. J. Cima, "3.091 Introduction to Solid State Chemistry, Lecture Notes No.7, Glasses," [Online]. Available: http://web.mit.edu/3.091/ www/ WittNotes/ Notes_7.pdf. [Accessed 4 June 2014].

[19] S. Bose, High Temperature Coatings, Burlington, MA: Elsevier, 2007.

[20] A. G. Evans, D. R. Mumm, J. W. Hutchinson, G. H. Meier and F. S. Pettit, "Mechanisms controling the durability of thermal barrier coatings," *Progress in Materials Science,* pp. 505-553, 2000.

[21] N. P. Padture, M. Gell and E. H. Jordan, "Thermal Barrier Coating for Gas-Turbine Engine Applications," *Science,* pp. 280-284, 2002.

[22] H. G. Scott , "Phase relationships in the zirconia-yttria system," *Journal of Material Science,* pp. 1527-1535, 1975.

[23] R. Doralia, "Thermal Barrier Coatings Technology: Critical Review, Progress Update, Remaining Challenges and Prospects," Maney for the Institute and ASM International, 2013.

[24] J. E. Mahan, Physical Vapor Deposition of Thin Films, New York: John Wiley and Sons, Inc., 2000.

[25] F. H. Stott, D. J. de Wet and R. Taylor, "Degradation of Thermal-Barrier Coatings at Very High Temperatures," MRS Bulletin, 1994.

[26] H. Peng, L. Wang, L. Guo, W. Miao, H. Guo and S. Gong, "Degradation of EB-PVD thermal barrier coatings caused by CMAS deposits," *Progress in Natural Science: Materials International,* pp. 461-467, 2012.

[27] R. Wellman, G. Whitman and J. R. Nicholls, "CMAS corrosionof EB PVD TBCs: Identifying the minimum level to initiate damage," *International Journal of REfractory Metals and Hard Materials,* pp. 124-132, 2010.

[28] J. Wu, H.-b. Guo, Y.-z. Gao and S.-k. Gong, "Microstructure and thermo-physical properties of yttria stabilized zirconia coatings with CMAS deposits," *Journal of European Ceramic Society,* pp. 1881-1888, 2011.

[29] C. Mercer, S. Faulhaber, A. G. Evans and R. Darolia, "A delamination mechanism for thermal barrier coatings subject to calcium-magnesium-alumino-silicate (CMAS) infiltration," *Acta Materialia,* pp. 1029-1039, 2004.

[30] X. Chen, "Calcium-Magnesium-Alumina-silicate (CMAS) delamination mechanisms in EB-PVD thermal barrier coatings," *Surface and Coatings Technology,* pp. 3418-3427, 2006.

[31] S. Kramer, S. Faulhaber, M. Chambers, D. R. Clarke, C. R. Levi, J. W. Hutchinson and A. G. Evans, "Mechanisms of cracking and delamination with thick thermal barrier system sin aero-engines subject to calcium-magnesium-alumina-silicate

(CMAS) penetration," *Materials Science and Engineering,* pp. 26-35, 2008.

[32] A. K. Rai, R. S. Bhattacharya, D. E. Wolfe and T. J. Eden, "CMAS-Resistant Thermal Barrier Coatings (TBC)," *International Journal of Applied Ceramic Technology,* pp. 662-674, 2010.

[33] A. Aygun, A. L. Vasiliev, N. P. Padture and X. Ma, "Novel thermal barrier coating that are resistant to high-temperature attack by glassy deposits," *Acta Materialia,* pp. 6734-6745, 2007.

[34] Joint Turbine Engine Sand Ingestion Working Group, "Manufactured Source for CMAS Creation & Ingestion in Gas Turbine Engines," Coatings Technology Integration Office AFRL/RXSSO, Wright-Patterson AFB, OH, 2013.

[35] R. Findlay, Great American Deserts, Washington D.C: National Geographic Society, 1972.

[36] T. Allan and A. Warren, Deserts The Encroaching Wilderness, New York: Oxford University Press, Inc, 1993, p. 14.

[37] J. W. Whitney, "Geology, Water, and Wind in the Lower Helmand Basin, Sothern Afghanistan," U.S. Geological Survey, Reston, Virginia, 2006.

[38] C. Klein and C. S. Hurlbut Jr., Manual of Mineralogy, New York: John Wiley & Sons, 1985.

REPORT DOCUMENTATION PAGE		Form Approved OMB No. 074-0188

The public reporting burden for this collection of information is estimated to average 1 hour per response, including the time for reviewing instructions, searching existing data sources, gathering and maintaining the data needed, and completing and reviewing the collection of information. Send comments regarding this burden estimate or any other aspect of the collection of information, including suggestions for reducing this burden to Department of Defense, Washington Headquarters Services, Directorate for Information Operations and Reports (0704-0188), 1215 Jefferson Davis Highway, Suite 1204, Arlington, VA 22202-4302. Respondents should be aware that notwithstanding any other provision of law, no person shall be subject to an penalty for failing to comply with a collection of information if it does not display a currently valid OMB control number.
PLEASE DO NOT RETURN YOUR FORM TO THE ABOVE ADDRESS.

1. REPORT DATE (DD-MM-YYYY) 18-Sep-2014	2. REPORT TYPE Master's Thesis	3. DATES COVERED (From – To) Sep 2012 – Sep 2014
TITLE AND SUBTITLE A Comparison of Afghanistan, Yuma, Az, and Manufactured Sands Melted on EB-PVD Thermal Barrier Coatings		5a. CONTRACT NUMBER
		5b. GRANT NUMBER
6. AUTHOR(S) Opie, Nathaniel P, Captain, USAF		5c. PROGRAM ELEMENT NUMBER
		5d. PROJECT NUMBER
7. PERFORMING ORGANIZATION NAMES(S) AND ADDRESS(S) Air Force Institute of Technology Graduate School of Engineering and Management (AFIT/EN) 2950 Hobson Way WPAFB OH 45433-7765		5e. TASK NUMBER
		5f. WORK UNIT NUMBER
		8. PERFORMING ORGANIZATION REPORT NUMBER AFIT-ENY-T-14-S-18
9. SPONSORING/MONITORING AGENCY NAME(S) AND ADDRESS(ES) Materials and Manufacturing Directorate AFRL/RX Materials Engineer, Lynne Pfledderer Lynne.Pfledderer@us.af.mil 2179 12th St, Bldg 652 Wright Patterson AFB, Ohio, 45433		10. SPONSOR/MONITOR'S ACRONYM(S) AFRL/RX
		11. SPONSOR/MONITOR'S REPORT NUMBER(S)

12. DISTRIBUTION/AVAILABILITY STATEMENT DISTRUBTION STATEMENT A. APPROVED FOR PUBLIC RELEASE; DISTRIBUTION UNLIMITED.

13. SUPPLEMENTARY NOTES This material is declared a work of the U.S. Government and is not subject to copyright protection in the United States.

14. ABSTRACT

Sand ingestion into military aircraft turbine engines from desert environments have tested the performance and life of the engine. In particular, turbine section blades and nozzles are coated with a molten glass when the sand is heated to melting temperatures. This molten glass attacks protective coatings on the surface of these parts. Further research is needed to understand the sands behavior on thermal barrier coatings (TBC) when heated to melting temperatures. Also, further research is needed with manufactured sand used in current engine testing to understand the sand ingestion discrepancies between test engines and operational engines. In this study natural sands from Yuma, Arizona, and Afghanistan will be heated to melting temperatures side-by-side with the manufactured sands specifically created for engine testing. All sands will be heated on EB-PVD TBC buttons provided by two companies who produce TBC coated turbine blades for current military engines. The results of manufactured sand should theoretically behave like natural sand and CMAS melted on a thermal barrier coating in order to substantiate past, current, and future testing. Additionally, the two EB-PVD TBCs behavior with the molten and cooled sand will be compared in this study.

15. SUBJECT TERMS Thermal Barrier Coatings Sand, Ingestion, Yuma, Afghanistan, QGCS, Melting, EB-PVD, CMAS

16. SECURITY CLASSIFICATION OF:			17. LIMITATION OF ABSTRACT	18. NUMBER OF PAGES	19a. NAME OF RESPONSIBLE PERSON Lt Col Timothy Radsick, AFIT/ENY
a. REPORT	b. ABSTRACT	c. THIS PAGE	UU	144	19b. TELEPHONE NUMBER (Include area code) (937) 255-36365, ext 4204 Timothy.Radsick@afit.edu
U	U	U			

Standard Form 298 (Rev. 8-98)
Prescribed by ANSI Std. Z39-18